UNIVERSITÉ DE STRASBOURG

ECOLE DOCTORALE pcp

ÉCOLE DOCTORALE DE PHYSIQUE ET CHIMIE PHYIQUE (ED 182)

ICS UPR-22 CNRS

THÈSE

présentée par :

Pierre AYOUB

soutenue le : **16 décembre 2015**

pour obtenir le grade de : **Docteur de l'université de Strasbourg**

Discipline/ Spécialité : **Physique**

Étude par dynamique moléculaire de formation d' excimères et de mélanges de lipides oxidés dans les membranes lipides modèles

THÈSE dirigée par :	
M.THALMANN Fabrice	Maitre de conférences, Université de Strasbourg
RAPPORTEURS :	
M.MONTICELLI Luca	Chargé de recherche , INSERM Lyon
M.SANDRE Olivier	Directeur de recherche, CNRS Bordeaux
AUTRES MEMBRES DU JURY :	
M.WITTMER Joachim	Directeur de recherche, Université de Strasbourg

UNIVERSITÉ DE STRASBOURG

Molecular dynamics study of pyrene excimer formation and oxidation in lipid bilayer models

Dissertation by

Pierre Ayoub

A thesis presented for the degree of
Doctor of Philosophy

December 16, 2015

PHD committee:

M. Joachim Wittmer	
M. Luca Monticelli	*Referee*
M. Olivier Sandre	*Referee*
M. Fabrice Thalmann	*Supervisor*

Contents

Preface **9**

Résumé de thèse en Français **11**
1 Introduction 1
2 Dynamique de formation des excimères du pyrène 1
  2.1 Taux de formation d'excimère 2
  2.2 Théorie et approximations 2
  2.3 Résultats numériques 4
3 Structure des bicouches lipides mélangées 5
  3.1 Analyse de la structure des bicouches 6
  3.2 Potentiel d'interaction 9
  3.3 Détermination du paramètre de mélange χ 9
  3.4 Aire moyenne par lipide 10

1 Introduction **12**
1 Membranes 12
  1.1 History of lipid membranes 13
  1.2 Amphiphilic molecules 15
  1.3 Self-assembly 18
2 Model systems 21
3 Experimental methods 26
  3.1 Scattering 26
  3.2 Nuclear Magnetic Resonance (NMR) 29
  3.3 Fluorescence microscopy 32
4 Time scale of lipid dynamics 36

2 Molecular Dynamics of bilayers **40**
1 Introduction to MD simulations 40
2 The Martini coarse-grained force field 46
  2.1 Model 46
  2.2 Applications of the Martini model 50

2.3 Limitations of the Martini model 51
2.4 Advantages of the Martini model 52

3 Excimer formation 54
1 Excimer formation mechanism 54
2 Two dimensional reaction rates and applications to membranes 60
3 Principle of the calculation 63
4 Algorithm 66

4 Submitted manuscript 69

4 Peroxidised Lipid Mixtures 87
1 Introduction 87
1.1 Peroxidised lipids 87
1.2 Solutions and mixtures 89
1.3 Radial Distribution Function 90
1.4 Theoretical determination of $g(r)$ and the Orstein-Zernike equation 92
1.5 Liquid state approach of lipid mixtures 93
1.6 Mixtures of coarse-grained peroxidised lipids 94
2 Bilayer setup and simulation details 94
2.1 Results 95
3 Summary 103

Conclusion 105

Appendices 107

A1 Equations of motion for atomic systems 109
1 Equations of motion 109
2 Stress 110

A2 On mixtures 111
1 Thermodynamic relations involving rdfs for pure fluids 111
2 A virial expansion for mixtures 112
3 The direct correlation functions 114
4 Numerical determination of the rdf 117

A3 Simulation-details 119
1 Dynamical quantities 119
2 Numerical integration of the monomer emission intensity 120
3 Simulation details for the excimer problem 120

4 Simulation details for the lipid mixtures problem 121

List of figures **123**

List of tables **127**

Bibliography **129**

Abstract **139**

Preface

Lipid molecules are fundamental components of biological cell membranes. Their amphiphilic structure consisting of one or two fatty acid chains attached to a hydrophilic headgroup, make them self-assemble in aqueous solution to form complex structures such as vesicles and bilayers. Because lipids interact together through weak forces, membranes are *soft* and *fluid* systems that undergo dynamics needed for specific cellular functions. While models for membrane structure have been constantly progressing, the dynamics of lipids are far from being well understood. Such is the case of the lateral diffusion which describes the motion of lipids in the bilayer plane. Measurements of lipid lateral diffusion coefficients for a given membrane may differ a lot depending on the experimental technique being used. The reason behind this disagreement could be the time scale of the measured diffusion; short range techniques probe the rapid motion of a lipid, while long range techniques measure the displacements over much larger scales.

In the past years, computer simulations has become an increasingly important technique for investigating biomolecular systems. Molecular dynamics (MD) simulations is a powerful tool that allows to test theoretical models and to interpret experimental results. MD allows the study of the structure of lipid bilayers as well as lipid dynamics on different time scales. Furthermore, it allows the calculation of many dynamical properties like diffusion and autocorrelation functions from atomic coordinates and velocities stored in trajectory files. Although atomistic simulations offer the most precise description, they are restricted to small length and time scales. Going beyond those limitations is achieved by simplifying the system through the use of coarse-grained CG models such as the *Martini force field*.

The aim of this work is first, to numerically investigate some dynamical properties of model lipid bilayers and compare them with available experimental results on pyrene excimer fluorescence, and second to investigate lipid mixtures using a recently proposed model for peroxidized lipids.

The structure of the thesis manuscript is as follows. In the first two chapters, I give a brief introduction on membrane bilayers and phospholipids, as well as on the dynamical properties of these molecules, the experimental and numerical techniques used to measure them.

In a third chapter, I introduce the pyrene excimer formation dynamics which is used experimentally for determining the membrane fluidity properties. I then outline the analyze that we perform on this problem using MD trajectories. These results are summarized in a manuscript which is currently under review. The manuscript is provided as chapter four.

In the fifth chapter, I discuss lipid mixtures. I simulate bilayers consisting of either a binary mixture of DOPC/DHP-DOPC (hydroperoxidized DOPC) or POPC/HP-POPC (hydroperoxidized POPC), at different molar fractions. Then, I attempt to extract system information through the means of the radial distribution functions, which can be related to thermodynamic mixing coefficients.

Résumé de thèse en Français

Étude par dynamique moléculaire de formation d'excimères et de mélanges de lipides oxydés dans les membranes lipides modèles

Pierre Ayoub

February 9, 2016

1 Introduction

Les lipides sont depuis longtemps étudiés par les biochimistes pour leur rôle important dans le vivant. Bien qu'étant des acteurs fondamentaux de la matière vivante, leur rôle a été parfois mésestimé. Il y a aujourd'hui un intérêt nouveau porté aux lipides, y compris de la part des physiciens, car la communauté scientifique reconnaît l'importance de ces molécules dans de nombreuses fonctions de la cellule[1].

Le but de ce travail est dans un premier temps d'explorer certaines propriétés dynamiques des membranes modèle, et d'effectuer la comparaison avec des résultats expérimentaux, et dans un second temps d'étudier les mélanges lipides à l'aide d'un modèle récemment proposé pour les lipides oxydés [2].

La structure du manuscrit de thèse est la suivante. Dans les deux premiers chapitres, je donne une brève présentation des phospholipides et des bicouches, ainsi que de leurs propriétés dynamiques et des techniques utilisées pour les déterminer.

Dans un troisième chapitre, je présente une approche statistique nouvelle basée sur un modèle à gros grains (Coarse-Grained) de membrane lipide qui nous permet d'analyser la dynamique de diffusion du DOPC (*1,2-Dioleoyl-sn-glycero-3-phosphocholine*) et du POPC (*1-palmitoyl-2-oleoyl-sn-glycero-3-phosph-ocholine*) à différentes températures. D'abord, je présente le modèle qui se fonde sur la dynamique de formation d'excimères, puis discute les approximations nécessaires pour calculer les probabilités de survie de tels systèmes à partir des trajectoires Martini (gros grains) obtenues. Ces probabilités de survies sont utilisées ensuite pour comparer les résultats théoriques avec les données expérimentales. Cela nous permet d'estimer le facteur d'accélération de la dynamique de lipides et, en suivant, le coefficient de diffusion.

Un manuscrit résumant les résultats de ce chapitre est en cours d'évaluation, et occupe le chapitre 4.

Au cinquième chapitre, je présente les mélanges de lipides. Je simule des bicouches consistant soit en un mélange DOPC/DHP-DOPC (DOPC péroxydé) ou POPC/HP-POPC (POPC péroxydé) à différentes fractions molaires. Ensuite, j'essaie d'extraire les informations du système à l'aide de fonctions de distribution radiales, qui peuvent être reliées au coefficients thermodynamiques de mélange.

2 Dynamique de formation des excimères du pyrène

La formation d'excimères est utilisée pour sonder les propriétés dynamiques des membranes. L'avantage que cette méthode a sur d'autres techniques basées sur la fluorescence est sa distance caractéristique courte de diffusion. Les molécules excimères sondent la mobilité sur l'échelle de quelques lipides puisque liée au temps de vie caractéristique du monomère excité $\sqrt{D\tau_M}$.

2.1 Taux de formation d'excimère

Les excimères sont des complexes formés par deux molécules identiques, une étant dans un état excité A* l'autre dans son état fondamental A. Le spectre d'émission de fluorescence des molécules isolées, communément qualifiée de monomère, diffère notablement du spectre d'émission de l'excimère, ou dimère (AA)*. Cela permet de mesurer optiquement la fraction de sondes fluorescentes formant un état de dimère excité (excimère). La cinétique d'un tel processus est habituellement donné par les équations

$$A + A^* \underset{k_d}{\overset{K(x)}{\rightleftharpoons}} (AA)^* \tag{1}$$

$$A^* \xrightarrow{k_M, k'_M} A + h\nu_M \tag{2}$$

$$(AA)^* \xrightarrow[k_E, k'_E]{} 2A + h\nu_E \tag{3}$$

où k et k' se rapportent aux taux de désexcitation radiatifs et non radiatif des monomères (M) et des excimères (E). $K(x)$ est le taux de formation d'excimère dépendant de la concentration, k_d le taux de dissociation supposé négligeable, et x la concentration en sondes fluorescentes:

$$x = \frac{[\text{probe}]}{[\text{probe}] + [\text{lipid}]} \tag{4}$$

Cette approche est limitée, et nous en proposons une meilleure.

2.2 Théorie et approximations

Le taux de réaction d'un processus limité par la diffusion dépend exclusivement de la dynamique de diffusion des deux espèces et de la forme géométrique de la région de réaction [3].

Une hypothèse commune à toutes les approches basées sur la fluorescence et que les molécules marquées, qui sont souvent aussi semblables que possible aux phospholipides, modifient seulement à la marge les structures et la dynamique de la membrane hôte [4].

Nous considérons une membrane simulée contenant un total de N_t lipides, parmi lesquels N_p seront considérés *a posteriori* comme contenant des groupes pyrènes fluorescents. Nous notons L le coté d'une boite de simulation carrée dans les directions x,y avec conditions aux limites périodiques (pbc) Nous introduisons la probabilité de survie

$P_s(\rho_c, N_p, N_t, L; t)$, probabilité qu'une paire de molécules choisies au hasard parmi les N_p possibles dans le même feuillet ne se soit pas approchée à moins d'une distance critique ρ_c pendant un intervalle de temps t. Nous définissons de manière similaire $P_o(\rho_c, N_p, N_t, L; t)$ pour deux feuillets opposés.

Sous condition d'illumination normale, on peut considérer qu'un fluorophore au maximum est excité à la fois, et et que $N_p - 1$ monomères sont disponibles pour se combiner sous forme d'excimère. Si le mouvement des monomères pyrène est décorrélé des autres, la probabilité de survie $P_s(\rho_c, N_p, N_t; t)$ se ramène à $P_s(\rho_c, 2, N_t; t)^{N_p-1}$. Nous appelons "approximation des paires indépendantes" la possibilité de factoriser la probabilité de survie lorsque la concentration x est suffisamment faible.

Il est assez naturel de supposer que la probabilité de survie dépend de la taille L ou du nombre de lipides N_t à travers le rapport intensif $x = N_p/N_t$.

La probabilité de survie obéit à la propriété d'échelle suivante:

$$\begin{aligned} P_s(\rho_c, N_p, N_t; t) &= P_s(\rho_c, 1 + \lambda^2(N_p - 1), \lambda^2 N_t; t) \\ &= P_s(\rho_c, 1 + \lambda^2(xN_t - 1), \lambda^2 N_t; t). \end{aligned} \tag{5}$$

Combinant approximation des paires indépendantes et propriété d'échelle, nous pouvons réduire la probabilité de survie d'un groupe pyrène excité à la probabilité de survie d'une paire unique située dans une bicouche de taille arbitraire λL:

$$P_c(t) = P_s(\rho_c, 2, \lambda^2 N_t; t)^{\lambda^2 x N_t - 1} P_o(\rho_c, 1, \lambda^2 N_t; t)^{\lambda^2 x N_t}. \tag{6}$$

La fonction de survie résultante $P_c(t)$ est la probabilité de collision globale. Ce qui reste à faire est d'utiliser un facteur λ correspondant aux conditions de simulations.

Intensité de fluorescence des excimères

La probabilité de former un excimère peut être déduite de $P_c(t)$. Un monomère excité à $t = 0$ se forme durant l'intervalle de temps $[t, t + \mathrm{d}t]$ avec probabilité

$$-\frac{\mathrm{d}P_c}{\mathrm{d}t} \exp\left(-\frac{t}{\tau_M}\right) \tag{7}$$

produit de la probabilité de collision avec un monomère dans l'état fondamental, tout en étant encore dans l'état excité, tandis que τ_M désigne le temps de vie de fluorescence du monomère dans le cas ultra-dilué ($x \to 0$). La probabilité de formation d'excimère J_E est donc:

$$\begin{aligned} J_E &= \int_0^\infty -\frac{\mathrm{d}P_c}{\mathrm{d}t} \exp\left(-\frac{t}{\tau_M}\right) \mathrm{d}t \\ &= 1 - \frac{1}{\tau_M} \int_0^\infty P_c(t) \exp\left(-\frac{t}{\tau_M}\right) \mathrm{d}t \end{aligned} \tag{8}$$

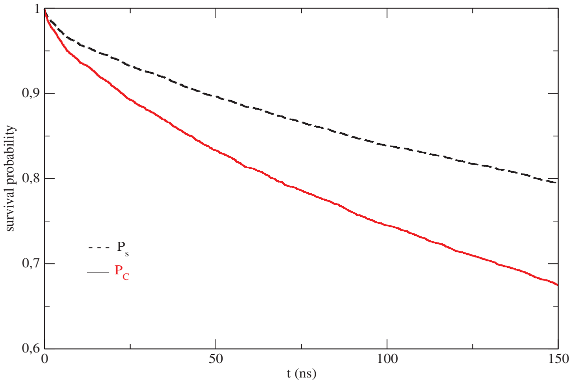

Figure 1: La probabilité de survie du dérivé pyrène dans une bicouche de DOPC à 10°.

Les simulations Martini sont accélérées d'un factor α communément choisi égal à 4 [5]. Comme corollaire, la dynamique à gros grains ne peut pas, seule, fournir d'estimation quantitative des coefficients de transport des lipides. Nous supposons dans notre approche que le facteur d'accélération α s'applique de façon uniforme. En d'autres termes, si l'on peut déterminer α en se fondant sur le régime de temps intermédiaires associé au temps de vie de fluorescence et à la formation d'excimères induite par collision, nous devrions être capable de prédire la constante de diffusion du lipide D comme $D = D_{MD}/\alpha$, où D_{MD} représente le coefficient de diffusion de la dynamique moléculaire obtenu à l'aide du déplacement carré moyen. Cela s'assimile à une procédure de *matching*.

2.3 Résultats numériques

Les simulations ont été faites pour des bicouches de DOPC et de POPC contenant 256 lipides par feuillet à 10°C et 20°C respectivement. La figure 1 montre la probabilité de survie collisionnelle $P_c(\rho_c, 2, 256; t)$ des sous-groupes de chaîne constitués des trois dernières billes, pour un rayon de capture de $\rho_c = 0.5$ nm. La probabilité a été calculée pour des collisions restreintes au même feuillet $P_s(2, 256; t)$, aux feuillets opposés $P_o(1, 256; t)$, et enfin au produit $P_c = P_s P_i$ lorsque les collisions entre feuillets sont autorisées. Ce dernier cas est le plus réaliste et sera utilisé pour ajuster les données expérimentales. Il faut noter que nous supposons que la formation d'excimère se produit à la première rencontre entre monomères (temps de premier passage).

Pour obtenir le meilleur accord avec la courbe expérimentale [6, 7], la probabilité de survie collisionnelle est insérée dans l'équation 8 et le temps de fluorescence de la sonde τ_M doit être déterminé. L'accord entre la courbe de titration expérimentale et la titration prédite à l'aide de la courbe de survie de la figure 1 est montré sur la figure 2. Le meilleur accord est obtenu avec un temps de fluorescence numérique égal

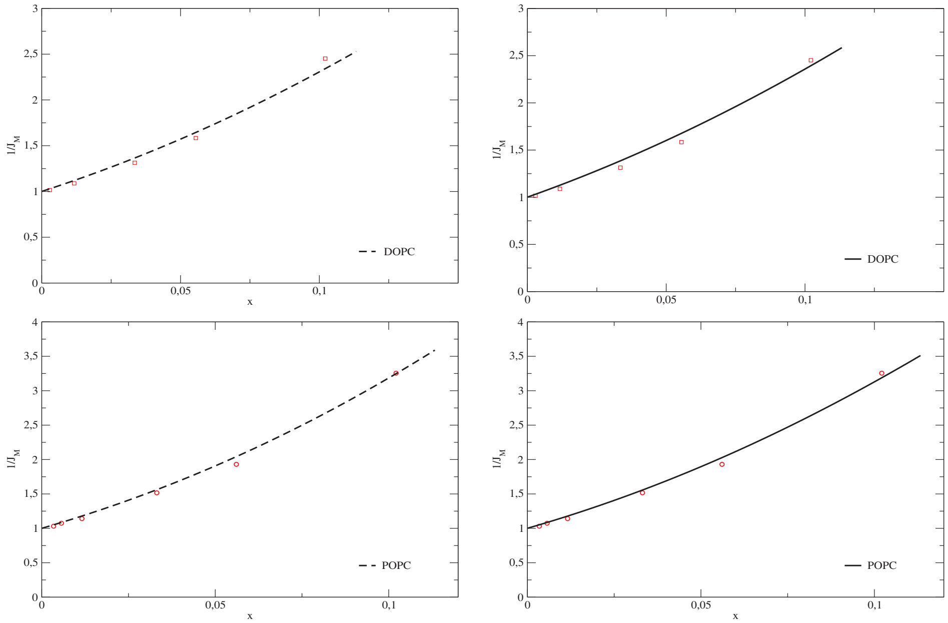

Figure 2: Axe horizontal: concentration x, axe vertical $1/J_M$. Émission normalisée des groupes pyrènes dans les bicouches DOPC et POPC, mesurées à 10°C et 20°C respectivement. Le paramètre τ_M est choisi pour donner le meilleur fit des courbes de titration expérimentales représentées par les carrés □.

à 6 ns. Le rapport entre les temps de vie numériques et expérimentaux détermine le facteur d'accélération $\alpha = \tau_M/\tau_{M,CG}$= 26, étant donné que τ_M à 10° est égal à 60 ns. La constante de diffusion du modèle à gros-grains D_{CG} est supposée de la forme αD, avec D la constante de diffusion vraie. Cette approche prédit D= 1 $\mu m^2.s^{-1}$ pour les molécules de DOPC pour les molécules de DOPC à 10°.

Ce schéma d'analyse, ainsi que la Table 1 sont les contributions originales principales de ce chapitre.

3 Structure des bicouches lipides mélangées

La péroxydation des lipides se produit quand l'oxygène singulet réagit avec des lipides, altérant les membranes, et créant des dommages aux cellules. L'oxydation concerne principalement les lipides insaturés [8] causant des changements de leur conformation et modifiant la composition des bicouches. L'oxydation provoque des changements structuraux, tel qu'une augmentation de l'aire par lipide [9].

Nous supposons un système consistant en un mélange binaire de DOPC et de lipide peroxydé, basé sur un modèle original à gros-grains. Ce dernier est une version légèrement modifiée du DOPC où un groupe péroxyde OOH [2] a été ajouté à la chaîne hydrophobe juste à l'endroit du lien C=C saturé. La même chose est proposée

Host	T (°)	α	$D(\mu m^2 s^{-1})$
DOPC*	10	15	1.6
POPC*	20	9	4
DOPC	10	26	1
POPC	20	20	1.8

Table 1: Coefficient de diffusion et facteur d'accélération du pyrène dans les bicouches de DOPC et POPC à 10° et 20° respectivement, pour un seul feuillet (*) et quand l'association entre feuillets est autorisée.

pour le POPC. Nous appellerons ces modèles à gros-grains de lipide péroxydés DHP-DOPC et HP-POPC.

En utilisant le champ de force Martini, nous avons réalisé des simulations pour différentes concentrations de mélanges DOPC/DHP-DOPC et POPC/HP-POPC.

Comme au chapitre précédent, nous utilisons la dynamique moléculaire pour étudier le mélange de lipides. En particulier, nous essayons de caractériser la relation entre composition et structure de la membrane. Les systèmes étudiés contiennent un total de 512 lipides et 3072 billes de solvant. Nous avons étudié des membranes contenant 16, 128 et 256 lipides peroxydés, formant des bicouches de concentration 3.1%, 25% et 50%. Les lipides modifiés sont également et aléatoirement distribués dans la membrane sur les deux feuillets.

3.1 Analyse de la structure des bicouches

Durant l'hydroperoxydation, un groupe $-OOH$ est ajouté aux chaînes hydrocarbonées, occasionnant une augmentation de l'hydrophilicité de celles-ci. L'effet structural sur la membrane se traduit par une augmentation de l'aire par lipide, comme le montre la table 2.

Une autre propriété importante est la fonction de distribution radiale (de paire) $g(r)$ qui a été calculée pour les mélanges ci-dessus. Par définition, le nombre moyen de particules situées à une distance comprise entre r et $r + \mathrm{d}r$ d'une particule de référence est $n(r)\mathrm{d}r = 4\pi r^2 \rho g(r)\mathrm{d}r$.

	Concentration de lipides oxydés (%)	Aire par lipide moyen(nm^2)	Épaisseur de boite moyenne (nm)	Volume moyen (nm^3)
DHP-DOPC:DOPC	0	0.67	6.57	1127.67
	3	0.674	6.54	1129.6
	25	0.716	6.25	1145.63
	50	0.75	6.07	1165.19
	100	0.8	5.87	1203.55
HP-POPC:POPC	0	0.64	6.551	1072.04
	3	0.642	6.52	1073.01
	25	0.672	6.28	1080.76
	50	0.704	6.05	1090.61
	100	0.745	5.82	1110.63

Table 2: Propriétés moyennes de la boite de simulation et aire par lipide pour différents mélanges à différentes concentrations.

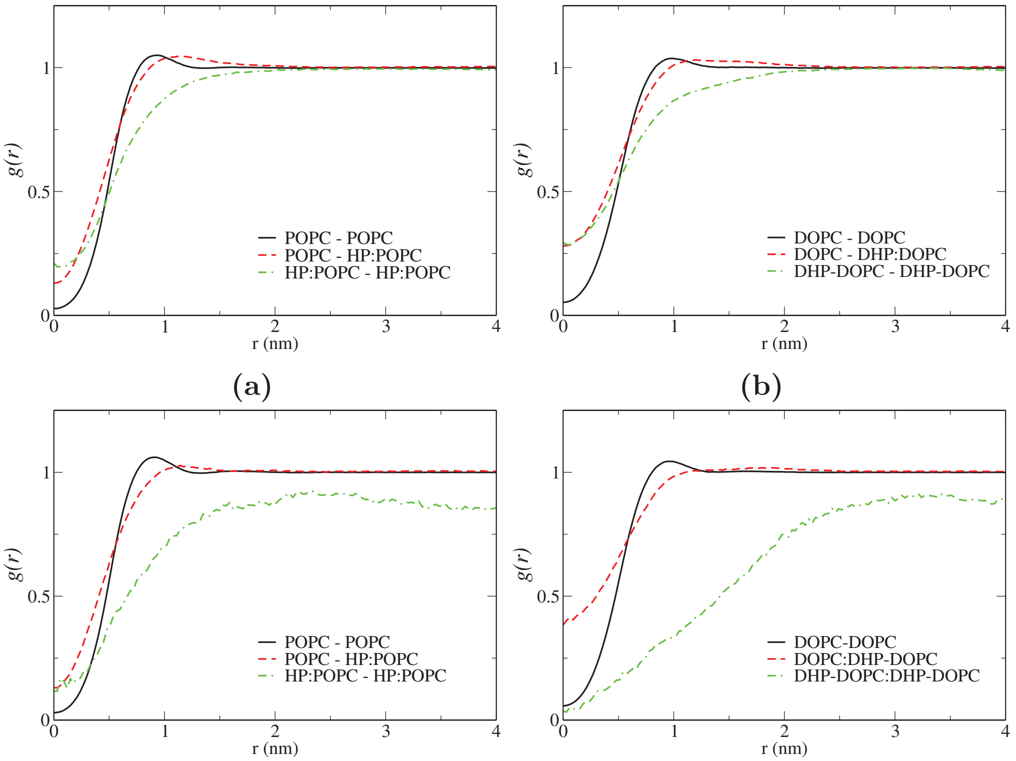

(a) **(b)**

(c) **(d)**

Figure 3: Fonction de corrélation de paires de DOPC:DHP-DOPC (b,d) et POPC:HP-POPC (a,c) pour une concentration de 25% (a,b) and 3.1% (c,d).

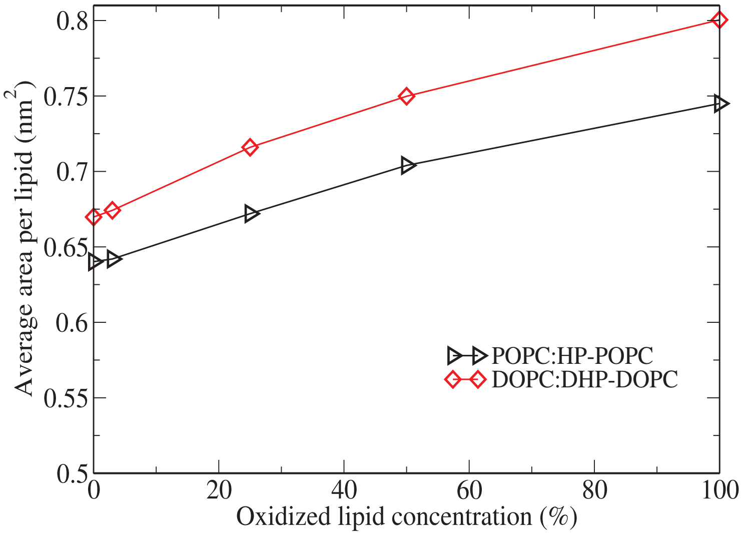

Figure 4: Aire moyen par lipide pour un mélange DOPC:DHP-DOPC et POPC:HP-POPC pour différentes concentrations d' oxydation.

De ces fonctions de distribution de paires binaires, on peut déterminer si les lipides ont tendance à se mélanger ou non. Nos résultats montrent que lipides péroxydés et normaux se mélangent bien, ce qui est nouveau et inattendu.

	Concentration des lipides oxydés (%)	paramètre d' interaction χ	χ_{11}	χ_{22}	χ_{12}
DOPC:DHP-DOPC	3.1	-4.058	0.978	8.538	0.67
	25	$-1{,}074$	1.027	2.371	0.625
	50	0,391	0.573	0.934	1.145
POPC:HP-POPC	3.1	-1.002	0.882	2.789	0.971
	25	-1.062	1.039	2.346	0.629
	50	-0.253	0.924	1.242	0.829

Table 3: Paramètres de mélange pour des bicouches DOPC:DHP-DOPC and POPC:HP-POPC. $\chi \leq 0$ indique un système ayant tendance à ce mélanger. Alors qu' une valeur de χ positive suggère la séparation des composants.

3.2 Potentiel d'interaction

Le potentiel d'interaction se dérive à partir des fonctions de distribution de paires. Dans le cas des fluides simples, celui-ci s'écrit

$$g(r) = e^{-\beta u(r)} \tag{9}$$

L'équation (4.14) est valable aussi pour les mélanges. Dans le cas d' un système composé de deux espèces A et B, le potentiel dans l' approximation du champ moyen est le suivant:

$$g_{AB}(r) = e^{-\beta u_{AB}(r)} \tag{10}$$

En conséquence, le calcul du logarithme de la fonction de corrélation de paires suffit pour déterminer le potentiel d'interaction de paires:

$$u^{(pmf)}(r) = -\frac{1}{\beta} \ln\left(g(r)\right) \tag{11}$$

La figure 4.8 représente le potentiel d'interaction effectif entre toutes les paires possibles dans des bicouches de DOPC : DHP-DOPC and POPC : HP-POPC.

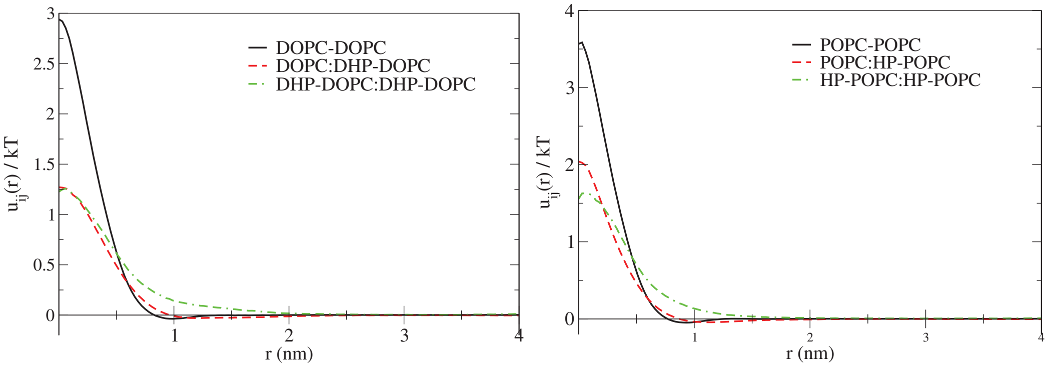

(a) DOPC:DHP-DOPC **(b)** POPC:HP-POPC

Figure 5: Le potentiel d'interaction de paires de DOPC:DHP-DOPC et POPC:HP-POPC pour une concentration d'oxydation de 25%.

3.3 Détermination du paramètre de mélange χ

Nous avons utilisé l'approximation du viriel pour déterminer le paramètre χ. Par exemple, pour un mélange 75:25 de POPC-HP-POPC, nous trouvons $\chi_{11} = 1.039$, $\chi_{12} = 0.629$, $\chi_{22} = 2.346$, et par conséquent une valeur négative pour $\chi = -1.062$, ce qui indique que les lipides et les lipides péroxydés ont une tendance à se mélanger. Nous avons aussi calculer le paramètre χ des autres mélanges, les résultats sont présentés dans le Table 4.1. Tous les systèmes simulés montrent une affinité au mélange, la seule exception étant le mélange DOPC/DHP-DOPC 50:50. Nous avons trouvé un paramètre de mélange χ positif ($0 \leq \chi \leq 2$), suggérant une faible séparation des deux composants du système.

3.4 Aire moyenne par lipide

Nous avons mesuré l'aire moyenne par lipide pour les différentes concentrations de lipides péroxydés (Table 2). Nous montrons aussi l'épaisseur de la boite de simulation. Les résultats sont présentés dans la fig.4.10. Pour les deux mélanges, l'aire par lipides augmente avec la concentration en lipide oxydés, alors que l' épaisseur décroît. Ce résultat attendue est conforme avec les expériences [10, 11] dans lesquelles le radical peroxydé est en contact avec l' eau. L' augmentation de l'aire par lipide est non linéaire avec la concentration. Le changement de l'aire par lipide lors de la péroxydation est due à l'exposition progressive du groupe péroxydé à l'interface air-eau.

Chapter 1

Introduction

1 Membranes

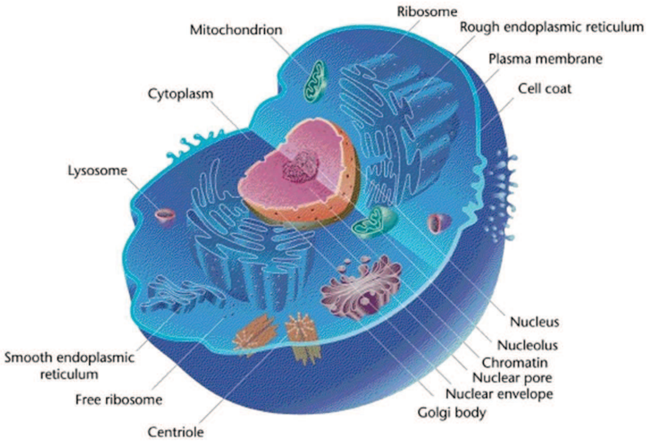
Ribosome
Rough endoplasmic reticulum
Mitochondrion
Plasma membrane
Cell coat
Cytoplasm
Lysosome
Nucleus
Nucleolus
Chromatin
Nuclear pore
Nuclear envelope
Golgi body
Smooth endoplasmic reticulum
Free ribosome
Centriole

Figure 1.1: Highly schematic, internal view of an eukaryote cell, characterized by a membrane-bound nucleus.

Cells are the building blocks of all life on Earth, whether it is unicellular organisms like bacteria, or multicellular complex organisms like plants and animals.

Membranes are essential components of living systems [12]. They act as a selective barrier, separating the interior of the cell from the exterior environment. In addition to the plasma membrane, eukaryote cells possess internal membranes surrounding organelles inside the cell, such as the mitochondria and the Golgi apparatus, all of them responsible of performing various tasks. These functional roles range from regulating the intake of structural molecules, providing metabolic energy and excreting the toxins resulting from that operation (Fig. 1.1).

The lipid bilayer is the basic structure of cell membranes, which works as a barrier between two aqueous compartments and is composed mainly of lipids (phospholipids, glycolipids, cholesterol) and proteins. The basic function of a membrane as a barrier is due to the structure of the phospholipids. The presence of dense hydrophobic fatty acid chains in the interior of the phospholipid membrane makes it impermeable to water-soluble molecules, including ions and most biological molecules. Another property that is essential to membrane functions is the ability of proteins and lipids to diffuse laterally. The fluidity and flexibility of the membrane are insured by the presence of one or more double bonds in the hydrocarbon chain of the phospholipids, that introduces kinks into the chains and prevents them from forming a too packed and rigid gel phase.

The high flexibility of the membrane insures their ability to deform under external perturbations such as elastic or viscous stresses (below a certain threshold). Red blood cells, for example, can strongly deform when travelling through capillary vessels without sustaining any structural damage [13].

Phospholipids, cholesterol, and glycolipids constitute the major part of lipids composing the membrane. The compositions of the inner and outer monolayers are different, reflecting the different roles of the two faces of a cell membrane. Different mixtures of lipids are found in the membranes of cells of different types, as well as in the various membranes of a single eukaryote cell. All this makes the membrane a molecular assembly of extreme complexity whose structure and function is difficult to predict, and which represents a challenge to scientists.

1.1 History of lipid membranes

Lipids are, alongside proteins, nucleic acids and sugars, major components of living matter. Initially reduced to energy storage molecules (triglycerides) or structural components of the cell membranes, they are now recognized for their signalling or membrane cell function regulating roles. The high complexity of lipid biochemistry, and their many roles in living cells is referred as the field of “lipidomics” [14].

Lipid structures are highly fluid and fluctuating. The usual tools of structural biology, though useful, are not sufficient to understand their behaviour and organization. Lipids in membranes display collective properties (phase behaviour for instance) that can only be properly understood using the concepts of thermodynamics and statistical physics. This maybe is the reason why lipidomics emerged relatively recently, as compared with studies on protein structures or the genetic code.

In **1917**, Irvin Langmuir discovered the structure of oil-water films and proposed that fatty acids form a monolayer by orienting themselves vertically, with the carbon chains pointing away from water and the carboxyl group in contact with water [15].

In **1925**, Gorter and Grendel demonstrated that red blood cells are covered by a layer of lipids that is two molecules thick [16]. They obtained their results by extracting lipids from blood cells and showed that these lipids can form bilayers, in addition to monolayers. Also, they showed that surface of area a monolayers extracted from blood cells are twice the area of the cells.

The word *Lipid* first appeared in a paper by W.M. Sperry in **1926** [17]. The term lipid was used to describe fats and all substances associated with them.

In **1935**, J.F. Danielli et Davson described a basic model for the structure of plasma membrane known as the ”sandwich” model. It states that a lipid bilayer was covered on both sides with proteins [18].

The techniques of structural biology (X-ray scattering) were applied soon to lipid-water solutions, by V. Luzzati, who was able to determine numerically the thickness of typical lipid bilayers forming multilamellar phases.

Bretscher proposed in **1972** that both leaflets of the lipid bilayer of biological membranes have different lipid compositions, thus defining an asymmetric structure granting the membrane functional properties [19].

A model of cell membrane architecture describing the organization of proteins and phospholipids, known as the fluid mosaic model, was proposed by S.J. Singer and G. L. Nicolson [20]. Proteins are partially embedded in a matrix of phospholipids, and both are able to move freely giving the membrane its fluid structure (Fig 1.2).

To add to the complexity of the membrane structure, Simons advocated for the existence of microdomains within the cell in **1997**. These *rafts* are presented as a new aspect of cell membrane based on the dynamic clustering of sphingolipids and cholesterol. They were mainly proposed as platform for the attachment of proteins [21].

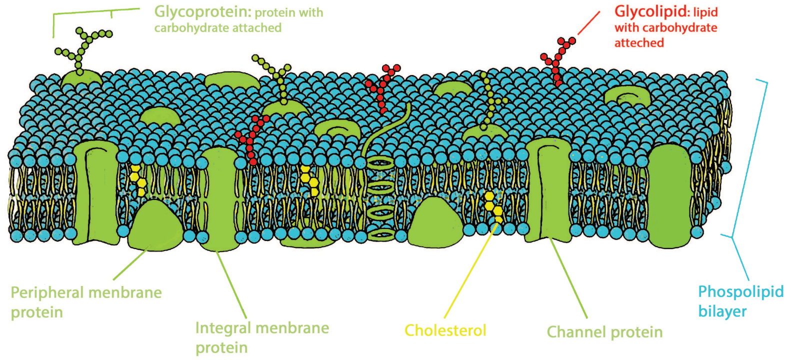
Glycoprotein: protein with carbohydrate attached
Glycolipid: lipid with carbohydrate attached
Peripheral menbrane protein
Integral menbrane protein
Cholesterol
Channel protein
Phospolipid bilayer

Figure 1.2: Fluid mosaic model in which integral proteins are inserted into a fluid structure pf phospholipids. Peripheral proteins do not react with the hydrophobic part of lipids, instead they are bound to the membrane by protein-protein interaction.

1.2 Amphiphilic molecules

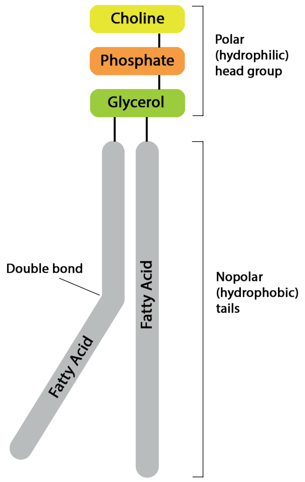
Choline
Phosphate
Glycerol
Polar (hydrophilic) head group
Double bond
Fatty Acid
Fatty Acid
Nopolar (hydrophobic) tails

Figure 1.3: Schematic representation of phosphatidylcholine representing the hydrophilic and hydrophobic part. The kink results from a double bond in the carbon chain.

We call hydrophilic molecules that are soluble in water (water loving) [22]. They can be charged or neutral polar molecules, capable of forming electrostatic interactions or hydrogen bonds with water molecules. In contrast, hydrophobic molecules prefer neutral or non-polar solvents and presents no attraction to water. Most hydrophobic molecules tend to be lipophilic (fat-loving), they are able to dissolve in oils and non-polar solvents. Amphiphilic molecules are compounds that present both hydrophilic and hydrophobic properties.

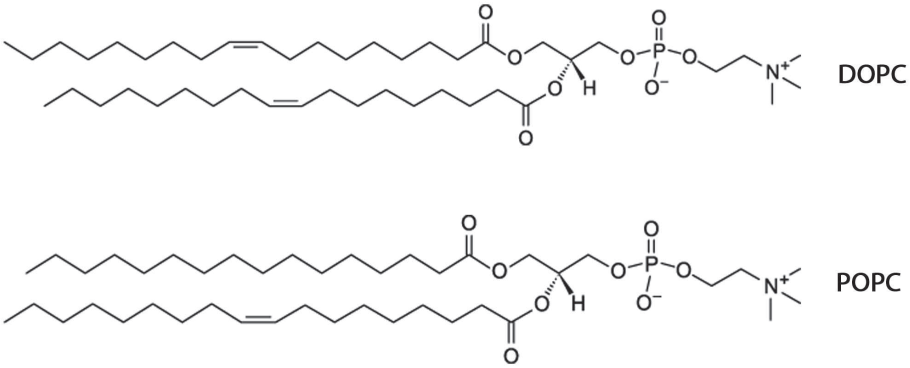

Figure 1.4: Chemical structure of two phospholipids $1,2-dioleoyl-sn-glycero-3-phosphocholine$, DOPC and $1-palmitoyl-2-oleoyl-sn-glycero-3-phosphocholine$, POPC. One presents a mono saturation (POPC) while the other have both tails unsaturated (DOPC).

Phospholipids The first phospholipid identified as such in biological tissues was lecithin (from the greek lekithos which means egg yolk), or phosphatidylcholine, in the egg yolk by Theodore Nicolas Gobley in **1847** [23, 24].

Glycerophospholipids fall in the category of amphiphilic molecules. They are one of the main components of biological membranes. Phospholipids are composed generally of two hydrophobic fatty acid tails/chains, connected by a glycerol molecule to a hydrophilic head consisting of a polar phosphate group. Lipids form bilayers by arranging themselves in a specific way. The polar group of these molecules points towards the surrounding aqueous medium while the hydrophobic tail remains inside the bilayer surrounded by other lipophilic chains, delimiting a non-polar region between two polar ones.

The average length of a phospholipid is about a few nm, and the average area per lipid lies between 0.6 and 0.75 nm^2 [25]. The hydrocarbon tails differ in length, which can range between 12 and 24 carbon atoms. The hydrocarbon chain can be unsaturated or saturated, whether it contains one or more double carbon-carbon bonds or not. The bonds in the chain have a structural consequences since they introduce kinks in the chain, in the case of *cis*-unsaturations. Unsaturated lipids chains tend to be liquid at room temperature due to the presence of these kinks that prevent them from packing, and act against solidification of the membrane. Double bonds in the chains are also the target of oxidation reactions, that occurs naturally in biological membranes.

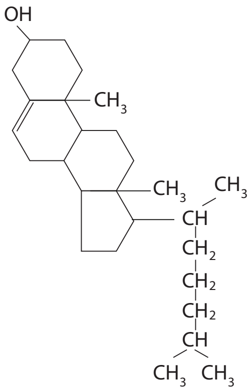

Figure 1.5: Chemical structure of cholesterol.

Cholesterol In addition to glycerophospholipids, eukaryote cell membranes contain other lipids such as cholesterol and glycolipids. François Poulletier de la Salle was the first to study a compound, that turned out to be cholesterol, in its solid form by isolating it from gallstone in 1758. However, it was chemist Michel Eugène Chevreul that named the compound *cholesterine* in **1815** [26, 27].

Characterized by its rigid ring structure illustrated in Fig. 1.5 (rings forbid rotation around C-C bonds), cholesterol is a major component of the membrane and plays an essential role its structure. It places itself in a way that its hydroxyl group (chemical group consisting of a hydrogen atom linked to an oxygen, as in an alcohol) is close to the polar phospholipid head so that their steroid (hydrophobic lipid molecule with a characteristic four-ringed structure) rings interact with regions of the hydrocarbon chains closest to the polar head (Fig. 1.6). Depending on the temperature, the effect on membrane fluidity due to cholesterol presence varies. At high temperature, cholesterol's interaction with the fatty acid chain reduce the mobility of phospholipids, making the lipid bilayer less deformable in this region and thereby decreases the permeability of the bilayer [28]. At low temperature however, it has the opposite effect on the membrane by preventing the hydrocarbon chain from ordering and crystallizing and thus obstructs possible phase transitions.

It is worth mentioning that cholesterol is exclusive to animal cells. It is not present in prokaryotes and plant cells, although the latter contain other compounds capable of performing similar tasks.

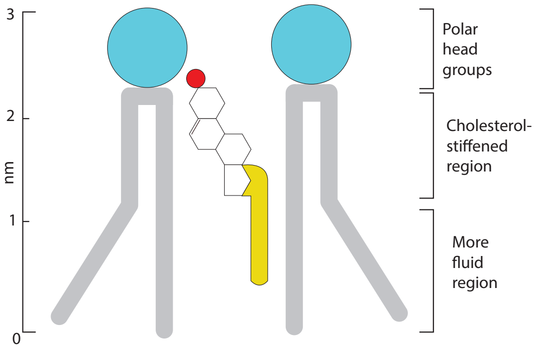

Figure 1.6: Interaction between cholesterol and phospholipids in a monolayer.

Recent studies suggest the existence of cholesterol enriched discrete membrane domains. These so called *rafts* are thought to move laterally within the membrane. Although their functions remain unclear, specific proteins associate with these clusters and may be important in roles related to cell signaling and endocytosis (the uptake of extracellular material in vesicles) [14].

1.3 Self-assembly

When put in aqueous solution, lipid molecules are known to spontaneously form bilayers as a result of their amphiphilic nature and shape. The hydrophilic part dissolve easily in water, while the hydrophobic part can not. As a result, lipids tend to cluster together in special structures to reduce the fatty acid-water interface and minimize the interactions. Although the ordering of water molecules causes an increase in free energy, the cost is minimized when the hydrophobic part of lipids is shielded from water molecules. So for instance, if we consider phospholipids on a water/air surface, the hydrophilic group will be submerged in water, while the hydrophobic chain will be in the air. If we keep increasing the concentration of lipids, the water/air surface is saturated and lipids are forced into the bulk of the solution, they spontaneously aggregate to hide the hydrophobic chain in the interior and leave the hydrophilic group to water, resulting in the formation of supra-molecular structures. This threshold is known as the critical micellar concentration (CMC $\sim 10^{-10}\,\mathrm{mol.L^{-1}}$ for typical phosphatidylcholine [29]).

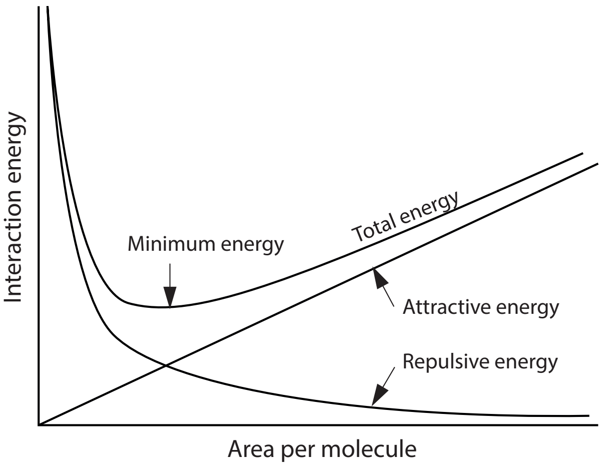

Figure 1.7: Interactive energy (attractive, repulsive and total) as a function of mean area per molecule a. Optimal headgroup area a_0 is obtained when the total interaction energy is minimized ($a = a_0$).

Lipids can self-assemble into different structures depending on their shape and on the surrounding environment. The forces that hold amphiphilic molecules together are weak. They result from non covalent interactions (van der Waals, hydrophobic, hydrogen-bonding). As a consequence, amphiphilic molecules aggregates are fluid like. Thus, any change in the aqueous environment, such as the pH or the number of ions, will modify the interactions and therefore the intermolecular forces holding the aggregate together, and by that changing the size and shape of the lipid aggregate.

Consequently, on the one hand hydrophobic interaction at the hydrocarbons-water interface gives rise to a positive interfacial free energy. On the other hand, the repulsion between the headgroups (whether it is hydrophilic, ionic or steric), promotes hydration (the molecule is surrounded with as much water as possible). Thus, we have a competition between two opposite forces. One is aiming to reduce, the other to increase the area of contact with water per lipid a [30]. The optimal area per headgroup at the surface is the one for which the total interaction energy per lipid molecule is a minimum (Fig. 1.7), and should not depend strongly on the chain length (number of carbon in the chains) [31].

It has been shown by Israelachvili that we can define a dimensionless *shape factor* v/a_0l_c, where l_c represent the length at which the hydrocarbon chain is considered fluid, and v the hydrocarbon volume. The value of this parameter indicates the type of the self-assembled structure that is formed [32]. The shape factor correlates well with the following sequence of amphiphilic structures: spherical micelles for $v/a_0l_c < 1/3$, non-spherical micelles for $1/3 < v/a_0l_c < 1/2$, vesicles or bilayers $1/2 < v/a_0l_c < 1$, or inverted structures $v/a_0l_c > 1$.

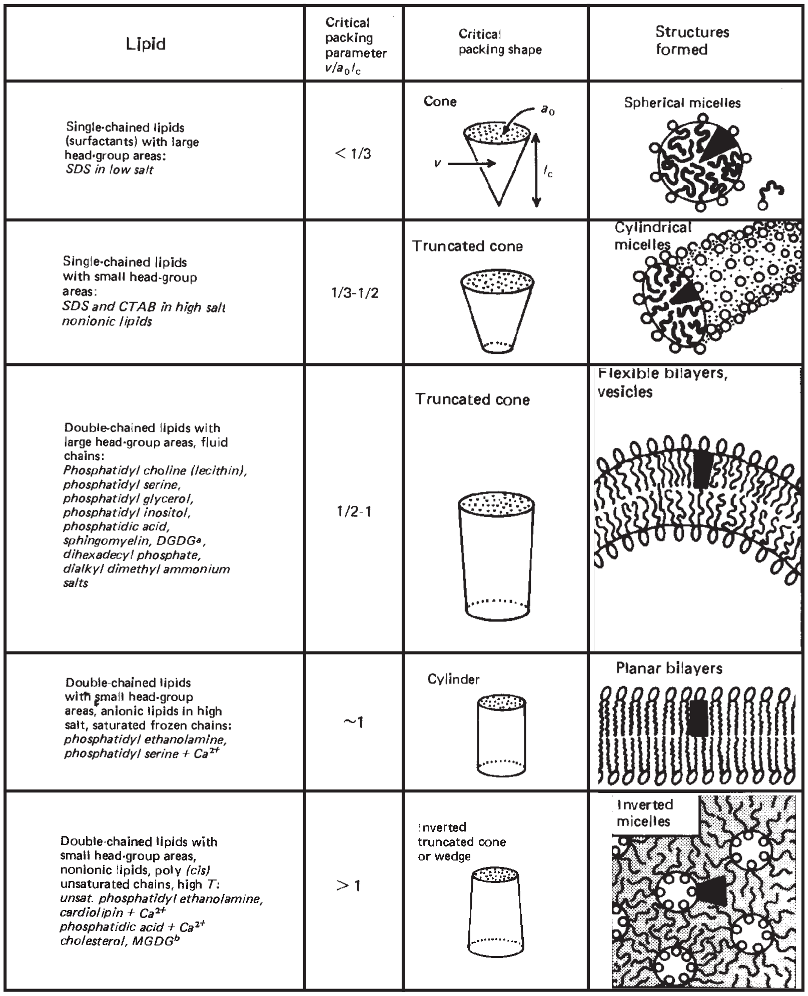

Lipid	Critical packing parameter $v/a_0 l_c$	Critical packing shape	Structures formed
Single-chained lipids (surfactants) with large head-group areas: *SDS in low salt*	$< 1/3$	Cone	Spherical micelles
Single-chained lipids with small head-group areas: *SDS and CTAB in high salt* *nonionic lipids*	1/3-1/2	Truncated cone	Cylindrical micelles
Double-chained lipids with large head-group areas, fluid chains: *Phosphatidyl choline (lecithin), phosphatidyl serine, phosphatidyl glycerol, phosphatidyl inositol, phosphatidic acid, sphingomyelin, DGDG*[a], *dihexadecyl phosphate, dialkyl dimethyl ammonium salts*	1/2-1	Truncated cone	Flexible bilayers, vesicles
Double-chained lipids with small head-group areas, anionic lipids in high salt, saturated frozen chains: *phosphatidyl ethanolamine, phosphatidyl serine + Ca^{2+}*	~1	Cylinder	Planar bilayers
Double-chained lipids with small head-group areas, nonionic lipids, poly *(cis)* unsaturated chains, high *T*: *unsat. phosphatidyl ethanolamine, cardiolipin + Ca^{2+}* *phosphatidic acid + Ca^{2+}* *cholesterol, MGDG*[b]	> 1	Inverted truncated cone or wedge	Inverted micelles

[a] DGDG, digalactosyl diglyceride, diglucosyl diglyceride.
[b] MGDG, monogalactosyl diglyceride, monoglucosyl diglyceride.

Figure 1.8: Packing arrangements of lipid molecules in an aqueous environment. Lipid molecules spontaneously form one or other of these structures in water, depending on their shape (from [29]).

Phases Lipids are capable of different conformations [33] based on many factors such as tail length, headgroup charge, number of lipid species, but most importantly size and temperature. This phenomenon is known as lipid polymorphism.

The effect of temperature comes from the entropic contribution ($-TS$ term in the free-energy definition) and depending on temperature, one observes different phases affecting the ordering and mobility of lipids (Fig. 1.9). At low temperatures, lipids chains are extended and ordered. The membrane is in its crystal phase L_c, while lipid motion (translation or rotation) is almost absent. When temperature increases, the membrane goes through a phase transition to adopt a less ordered configuration while keeping an orientational tail ordering. In the gel phase L_β lipids start to diffuse across the membrane ($D \approx 10^{-2}\,\mu m^2/s$). At high temperatures, the bilayer is in the fluid phase L_α and both tails and head groups are disordered. The lipids lateral mobility increase and their diffusion coefficient is about a few $\mu m^{-2}/s$. The complexity of the membrane composition leads to complex phase diagrams. Phase transitions occur at temperatures specific of the lipids forming the membrane. This temperature is affected by the presence of cholesterol and the presence of unsaturations in the lipid tails. Such effects are usually detected by calorimetric techniques, and the gel/fluid transition is called the melting transition T_m.

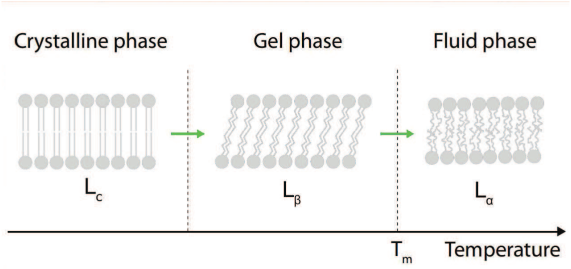

Figure 1.9: Scheme illustrating different phases of a lipid bilayer in an aqueous medium as a function of temperature.

2 Model systems

Biophysicists and biochemists have built artificial membrane systems using the self-assembly character of amphiphilic molecules, in order to reproduce the properties and to understand the phenomena taking place in a cell membrane. These artificial membranes or artificial bilayers have a simpler composition than the original biological membranes which contain a wide variety of lipids and proteins.

Examples of such artificial systems are: the supported bilayers, the small unilamellar vesicles (SUV, or liposomes), the large or giant unilamellar vesicles (LUV, GUV).

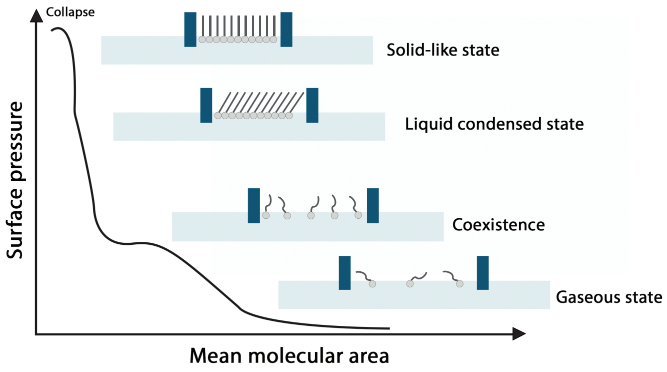

Figure 1.10: Surface pressure vs area isotherms of a Langmuir monolayer. The monolayer exhibits states transition from gaseous state, to liquid expanded (LE), liquid condensed (LC) and finally solid state upon compression.

Langmuir-Blodgett (LB) technique The most appropriate method for forming a supported lipid bilayer involve the Langmuir–Blodgett (LB) technique. When insoluble amphiphilic molecules are deposited on water, they interact with the air through an air-water interface and thus form a mono-molecular layer, called Langmuir monolayer. As a result, the surface tension of water is lowered. The new surface tension γ can be measured using Whilhelmy plate [34] at the air-water interface. The surface pressure becomes $\pi = \gamma_0 - \gamma$, where γ_0 is the surface tension of pure water. For small concentration (much smaller than critical micellar concentration CMC), i.e small surface pressure, amphiphiles show random motions very similar to an ideal gas phase.

When compressed, the thin film formed by the molecules on the interface exhibits modifications associated to phase transitions. When reducing the surface area of the monolayer, the surface pressure increases, The film compresses from a gas to a liquid-expanded (LE) then liquid-condensed (LC) and ultimately to a solid like state if the tails are ordered (not tilted). For high concentration, the monolayer may eventually break (collapse). The area of the interface (A) can be controlled and compressed using an LB trough Fig.1.11.

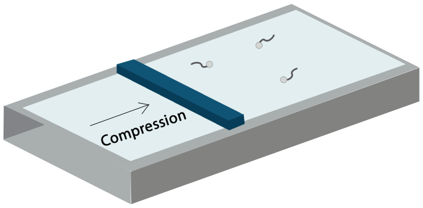

Figure 1.11: Langmuir trough used to compress molecules on the surface of a subphase.

Plotting the surface pressure as a function of the interfacial area yields compression/decompression isotherms [35](Fig. 1.10) which provides useful information about the physical state of the system and the organization of the lipid molecules([36, 37]).

Langmuir-Blodgett technique has many applications in biological systems. However, the large contact area at the interface between the hydrocarbon chains and air causes the self-assembled monolayers to display a surface tension much larger than that of a biological membrane for which the surface tension is almost zero [38].

Supported lipid bilayers The LB technique allows the adsorption of the Langmuir film onto a substrate (solid support), at a constant surface pressure and a constant speed to form a supported bilayer [39]. The first step is to pull the support from the surface of the monolayer. If the substrate is hydrophilic, like mica, the polar head groups interact with it, thus leaving the hydrophobic tails exposed in the air. Next step is to dip the substrate allowing the deposition of a second monolayer and therefore the formation of a supported bilayer as shown in figure 1.12. In contrast, if the solid surface is hydrophobic, like silicon, the steps are performed in the reverse order and an inverted bilayer is created. By repeating the process, we obtain a complete bilayer. The transferred lipid monolayers can be of different compositions, thus forming asymmetric supported lipid bilayers.

Supported lipid bilayers can also be obtained from small unilamellar vesicles (SUV). When put in contact with a hydrophilic substrate, SUVs adsorb and eventually burst on the surface of the support, leading to the formation of supported bilayers [40, 41, 42, 43]. Unlike LB deposition, the fusion of vesicles on hydrophobic support cannot lead to the formation of asymmetric bilayers. The vesicle fusion technique is simple, and the formed supported bilayers are pertinent [44].

Supported membranes on solids are very stable which makes them practical for surface-sensitive techniques like Atomic Force Microscope (AFM) or Surface Force Apparatus (SFA) [45] and other spectroscopy techniques [46] to study their dynamical and structural properties. Another reason that makes supported bilayers interesting is the fact they form versatile models of two dimensional complex fluids, which can be used to study interfacial forces and membrane interactions [47].

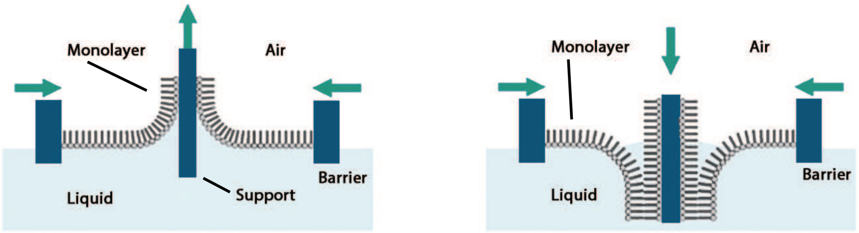

Figure 1.12: Langmuir-Blodgett deposition.

Vesicles It is energetically unfavourable to form two dimensional membranes with edges, exposing the hydrocarbon chains to water molecules. Thus, the membrane closes on itself, forming a spherical vesicle (Fig. 1.13). These structure can be either unilamellar formed by a single bilayer, in this case they are called liposomes or multilamellar formed by stacking multiple bilayers. These structures can be grouped into three main categories based on their size. Small vesicles are known as ***S**mall **U**nilamellar **V**esicles*, SUV's have a size ranging between 20 and 100 nm. While larger vesicles ranging from 100 nm to 500 nm are known as ***L**arge **U**nilamellar **V**esicles. And **G**iant **U**nilamellar **V**esicles* are the ones with diameter ranging from 500 nm to 100 μm on average. GUV can be observed, and even manipulated under an optical microscope.

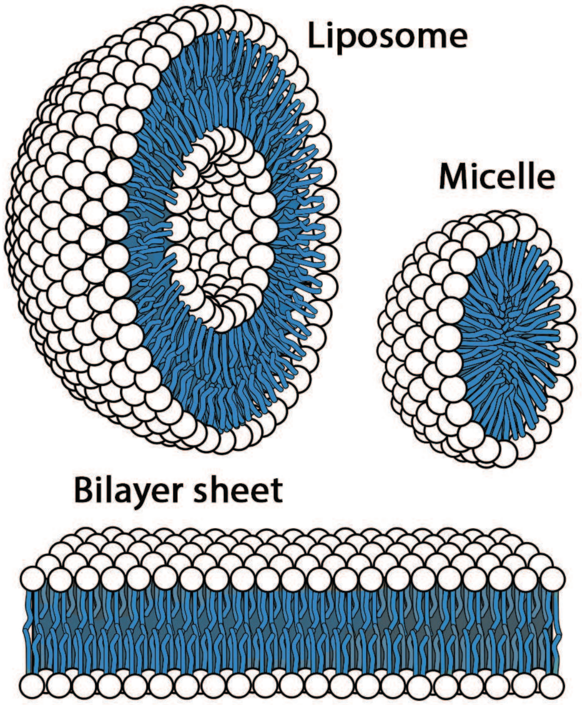

Figure 1.13: Schematic view of a spherical vesicle two lipid thick (liposomes), a micelle and lipid bilayer.

The size of the artificial vesicles is hard to control and depends mainly on the preparation technique. The first reported method of vesicle formation goes back to 1969. A controlled hydration of dry thin film of egg yolk lipids led to the formation of giant unilamellar vesicles [48]. In the last decades, many improvements and breakthroughs have been achieved in controlling the size of the desired vesicles. Small unilamellar vesicles can be prepared by sonication [49], while large unilamellar vesicles were obtained by extrusion of multilamellar vesicles through specific membranes [50], and GUVs can be achieved by electroformation [51].

Small vesicles, or liposomes have a wide range of pharmaceutical applications, in particular as drug delivery systems [52]. Also, they can be used for targeting particular diseases in the cell, as they have a low toxicity and higher efficiency than traditional techniques. Anticancer therapy using liposomes is available (example CAELYX$^{\mathrm{TM}}$).

Large vesicles enables a direct visualization of various phenomena (phase separation, decoration by fluorescent proteins). It is also possible to measure the membrane mechanical properties (elasticity or bending modulus for instance) [53].

3 Experimental methods

The experimental study of the diversity of lipids and their complex arrangement in membranes at molecular level represents a challenge. Ideally, one would like to observe the structure of different lipid phases and molecular conformations. The dynamics of lipid motion and transient features in membranes are also of interest, all this being part of the membrane fluid mosaic model.

This experimental knowledge requires a combination of complementary techniques, and many detailed features still remain today out of reach. Each technique has a validity range and characterizes a different property of the membrane. In the following section we discuss a few of the widely used methods.

3.1 Scattering

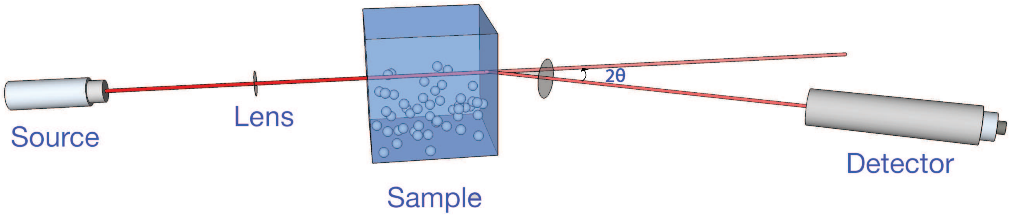

Figure 1.14: A scattering experiment setup. In the *Fraunhofer approximation*, the incident beam and the beam reaching the detector are considered a plane wave due to the fact that the distances between the source-sample and sample-detector are significantly larger than the size of the sample.

Scattering techniques are useful in studying the structural as well as the dynamical properties. These methods are based on the interaction between an incident wave (light or particles) and the sample.

The key element in all scattering experiments is the modification of the incident wave vector **k** caused by the heterogeneities of the sample in question. We define the momentum transfer (scattering vector) **Q** as the difference between the incident wave vector and the scattered wave vector **k'** as

$$\mathbf{Q} = \mathbf{k} - \mathbf{k}' \tag{1.1}$$

We distinguish two types of scattering: elastic and inelastic. Elastic scattering is when the energy change of the radiation is negligible. Inelastic processes are caused by internal fluctuation in the sample, leading to some energy change of the radiation. Scattering experiments consist on measuring the emitted radiation intensity distribution as function of the scattering vector.

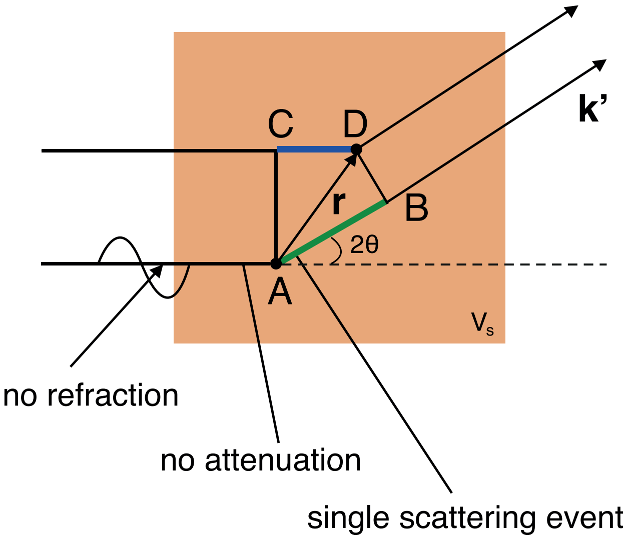

Figure 1.15: Phase difference between a beam scattered at the origin A and a beam at a position **r**.

In order to probe a length scale l, the phase difference must satisfy the following condition

$$\delta\phi = \mathrm{Q.l} = 2\pi. \tag{1.2}$$

It is clear form (1.2) that the wavelength of the radiation λ should be in the same order of magnitude of real space lengths of interest. Hence, in order to probe the structural properties of a system, if l_0 denotes the inter-particle distances, then the requirement needed is $\lambda \sim l_0$. A comparison of the length scale of each technique is given in Fig.1.16 that demonstrates for which $E-\lambda$ (energy-wavelength) combination a certain probe is particularly useful.

The probes in scattering experiments can be electromagnetic waves (light and X-ray diffraction) or particle waves (neutron or electron scattering).

X-ray diffraction Small angle X-ray (SAXR) scattering detects small variation in the structure of the membrane of the order of the nm, and can be used to measure the thickness of a bilayer. This is also how area per lipids are obtained. Wide angle scattering (WAXS) provides more resolution (sub-nanometre), useful for studying the more ordered phases of the bilayer (crystalline or gel phase) and tail packing [54]. The interaction of X-rays with electrons depends on the electron density profile. This means that the scattering cross section depends on the number of electrons, i.e the atomic number of the element. Therefore, it is difficult to detect small atoms such as hydrogen using this technique in the presence of heavier ones, as well as elements with similar atomic numbers.

Particle scattering

Particles such as neutrons and electrons can be used as well. These particles are governed by the Schrödinger (thermal neutrons) and Dirac equation (fast electrons). While easy to use in practice and capable of producing resolution up to fraction of an atom (for an energy of 100 KeV, $\lambda \sim 10^{-2}$ Å), the drawback of electrons is their charge. Electrons interact with the sample via coulomb interaction, making it impossible to neglect multiple scattering effects. However, electron microscopy remains a very powerful imaging technique, if the samples are thin enough. CryoTEM relies on freezing thin aqueous samples containing small objects, such as SUVs. It is then possible to visualize directly the bilayers and various morphological changes occurring when they interact with other components.

Neutron scattering In contrast, thermal neutron ($E = 25$ meV at T = 300 K) have a wavelength $\lambda \sim 0.1$ nm. Neutrons have no charge. The absence of the coulomb interaction, allows neutrons to penetrate deeper in the bulk of the sample. Small angle neutron scattering (SANS) probes the size scales of most soft matter structures, ranging from nanopores to polymer aggregates. Additionally, the energy of thermal neutrons matches the energy of elementary excitations such as lattice vibrations (phonons).

Thermal neutrons interacts with the nuclei within the sample. The neutron-nuclei interaction is different for each isotope. This means that the scattering length density, specific to each isotope, plays the role of the atomic number like in the case of X-ray scattering. This is exploited in practice by substituting deuterium (isotope of hydrogen) into certain molecules in order to vary the contrast and makes structures easier to detect. Scattering by subcomponents of a lipid molecules can be specifically enhanced or reduced.

Light scattering

Electromagnetic waves dynamics are governed by the Maxwell equations. The light beam interacts with the electrons of the sample, and is scattered by optical index heterogeneities. A special technique using the intensity time dependence of an elastic light scattering signal (DLS, dynamic light scattering) makes it possible to measure the Brownian diffusion coefficient of subwavelenth objects moving in a solution. The size of SUVs can be obtained in such a way.

Inelastic scattering So far, we considered only elastic scattering, by assuming static samples. In reality, density fluctuations and Brownian motion are present. The dynamics of the samples in question are investigated by the mean of inelastic or quasielastic scattering. As a result, we measure not only pair correlation function

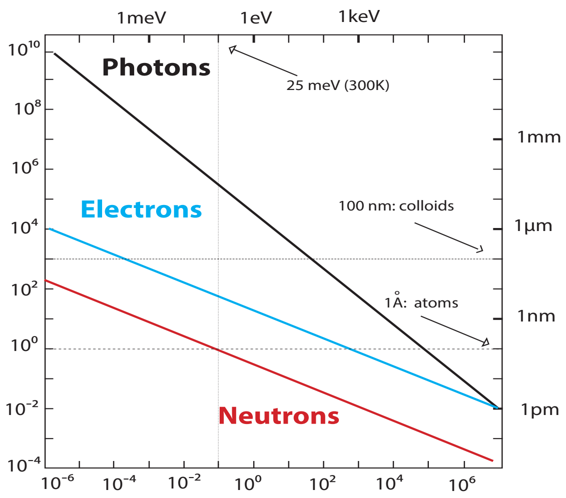

Figure 1.16: Plot of the dispersion relation on a double logarithmic scale. The energy-wavelength plot for neutron, electron and photon helps determining the most appropriate investigative method for the system in hand.

as in the case of elastic scattering but also the auto-correlation of the particles with time. For example, quasielastic neutron scattering (QENS) probes the dynamics of the system such as local vibration and diffusion [55].

3.2 Nuclear Magnetic Resonance (NMR)

Nuclear magnetic resonances (NMR) stands out as one of the most powerful spectroscopic techniques to determine structural properties and dynamics of systems. NMR is based on the interaction of the magnetic momentum of a nucleus with an

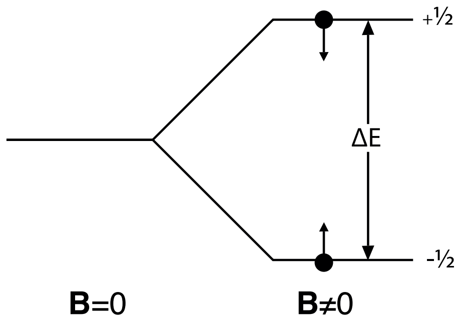

Figure 1.17: The nuclear spin energy levels of a spin 1/2 nucleus in the presence of a magnetic field.

external magnetic field. A nucleus with a spin angular momentum **I** presents $2\mathbf{I}+1$ orientation of its “magnetic number”m_I. A nuclei with non zero spin has a magnetic moment $\boldsymbol{\mu}$. The z component of $\boldsymbol{\mu}$ depends on the orientation of the spin :

$$\mu_z = \gamma m_I \hbar \tag{1.3}$$

where $\hbar$ is the reduced plank constant and γ is the gyromagnetic ratio of the respective nucleus. When put in a magnetic field (usually along the z axis), the nucleus energy levels splits into m_I values:

$$E_{m_I} = -\mu_z B = \mu_I \, \hbar \, w_0 \tag{1.4}$$

where $w_0 = \gamma B$ is the Larmor frequency. If the nucleus for example has a spin moment of 1/2 (like hydrogen ^{1}H and phosphate ^{31}P), the energy splits into two levels, one with orientation +1/2 and the other -1/2, and the energy separation $\Delta E = \gamma \, \hbar \, B$ (Fig. 1.17).

The nuclei can resonate between the two states by absorbing an energy equal to the energy difference between the states. to achieve nuclear magnetic resonance, a rotating magnetic field in the orthogonal plane $\mathbf{B}' \perp \mathbf{B}$ is applied. The circular frequency of $\mathbf{B}'$ is equal to the Larmor frequency w_0 in order to flip between states.

Although the energy difference depends on γ and the constant external field $\mathbf{B}$, that does not result in the same resonance energy spectrum for nuclei with the same gyromagnetic ratio. The cause of this so called *chemical shift* is the electron shell surrounding the nucleus. The spin-orbit interaction result in a magnetic field that affects the nucleus by reducing the energy gap between the states.

NMR can be used to detect the dynamics of the system, in particular the diffusion coefficient. Pulsed field gradient NMR (PFG-NMR) applied on oriented bilayers helps to investigate the effect of the structure, and obstacles on the dynamics by measuring the lateral diffusion coefficient [56, 57]. The principle of PFG-NMR is to apply two opposite strong magnetic field pulses (short time) two different time. Applying a gradient causes the changes the Larmor frequency making it depend on the position. This creates a phase difference between spins at different position. After some time, during which the atoms would have diffused, another gradient is applied. This gradient is opposite to the first one, and have the purpose of reversing the phase differences caused by the first gradient. However, the movement of the spins would have caused them to adopt an new frequency, hence a new phase, and the reverse does not restore the initial configuration (Fig. 1.18).

The diffusion coefficient D is determined using the Stejskal-Tanner relation [58]

$$\ln\left(\frac{S}{S_0}\right) = -\gamma^2 \, G^2 \, \delta^2 D \left(\tau - \frac{\delta}{3}\right) \tag{1.5}$$

where S and S_0 represent the amplitude of the signal with and without the gradients, G is the gradient pulse, δ is the pulse duration and τ is the delay between them. δ is usually very small compared to τ ($\delta \ll \tau$) which simplifies the relation $\left(\tau - \frac{\delta}{3}\right) \longrightarrow \tau$.

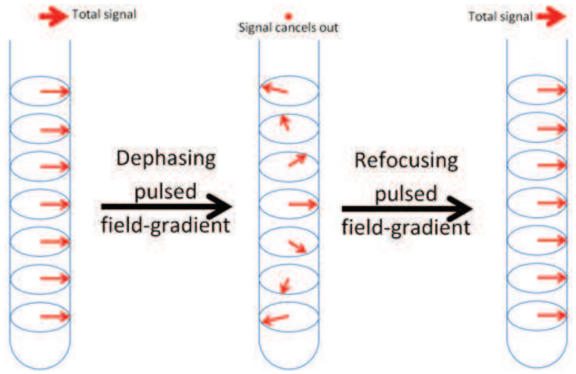
Total signal
Signal cancels out
Total signal
Dephasing pulsed field-gradient
Refocusing pulsed field-gradient

Figure 1.18: Illustration of the pulse-field gradient method. Nuclei diffusing in the presence of a balanced gradient pair. The two gradients are separated by a diffusion time interval δ and are very short ($\delta \ll \tau$). A diffusion gradient changes the phase of a spin depending on its position. The result is two signals; the signal obtained without any diffusion gradients, and the signal attenuated due to phase dispersion caused by the diffusion gradient pair.

The deuterium element has a spin 1 and its resonance depends on the angle between the bond bearing the hydrogen (usually CD) and the applied constant magnetic field. One can recognize in this way the lipid phases (fluid, gel for instance) and the average orientation angle between the lipid chains and the external field. NMR therefore contributes significantly to the determination of structural membrane properties.

3.3 Fluorescence microscopy

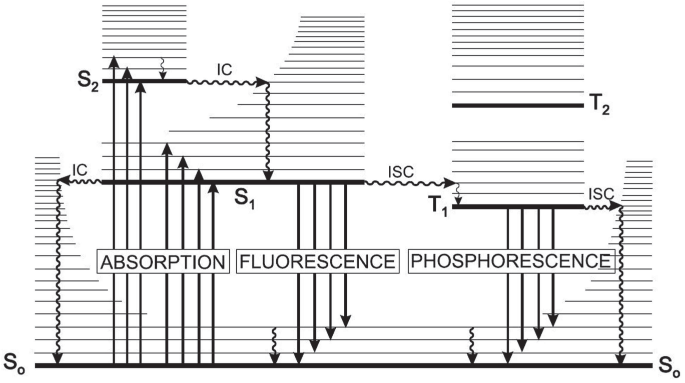

Figure 1.19: Perrin-Jablonski diagram illustrating the possible de-excitation processes of a molecule with no surrounding. Figure from [59].

Since the first reported observation of fluorescence in 1565 by Nicolas Monardes to the introduction of the term fluorescence by George Gabriel Stokes in 1853, this physical effect of light-matter interaction has become a powerful tool for probing the structure and dynamics of organic systems at a molecular level. Once a molecule absorbs a photon, it can return to its fundamental state through many de-excitation pathways that compete with each other. These pathways are visualized in the Perrin-Jablonsky diagram (Fig. 1.19) and they can be grouped into two categories:

- Radiative de-excitation such as fluorescence, phosphorescence and delayed fluorescence.
- Non radiative de-excitation, such as internal conversion and intersystem crossing.

The relaxation from $S_1 \rightarrow S_0$ through the emission of a photon is called *fluorescence*. Fluorescence wavelength is higher than that of the absorption; at room temperature the majority of the molecules are at the lowest vibrational level of the ground state according to the Boltzmann distribution. Once a photon is absorbed, the molecule is excited to any of the vibrational levels of the first singlet states, then it relaxes to the zero vibrational level of S_1 through internal conversion. Due to this excess energy loss, the absorption and the emission spectra are different. The gap between the maximum of both spectrum is called *Stokes shift*. However, in most cases these two spectrum overlap since even at room temperature a small number of molecules are in a vibrational level higher than 0 as stated by Einstein.

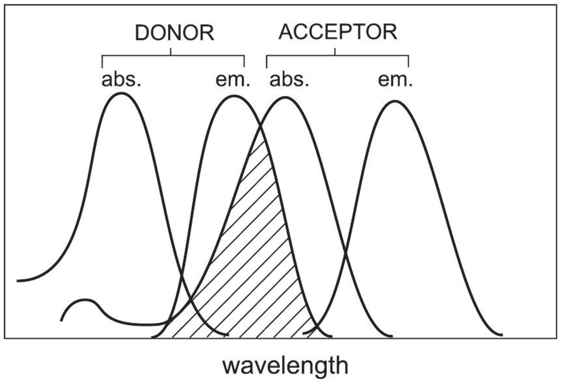

Figure 1.20: Illustration of the integral overlap between the emission spectrum of the donor and the absorption of the acceptor. Figure from [59].

Fluorescence emission occur according to :

$$D + h\nu \longrightarrow D^*$$

$$D^* \xrightarrow{k_r^S} D + h\nu' \qquad \text{Fluorescence lifetime : } \tau_r = 10^{-7} - 10^{-10} s.$$

Where, k_r^S is the rate constant for radiative de-excitation $\mathrm{S}_1 \rightarrow \mathrm{S}_0$ with emission of fluorescence and $\tau_r = \dfrac{1}{k_r^S}$.

Single molecule detection (SMD), Förster resonance energy transfer (FRET), fluorescence recovery after photobleaching (FRAP), fluorescence correlation spectroscopy are all fluorescent techniques used to measure the lateral mobility of lipids as well as investigating domain formation.

Förster resonance energy transfer FRET

When a fluorescent molecule is in solution, possible interactions with the surrounding molecules can give birth to other de-excitation pathways. They are called intermolecular photophysical processes such as electron transfer, proton transfer, excimer formation, radiative and non-radiative energy transfer. *Resonance energy transfer* is a non-radiative transfer induced by long ranged electric dipole-dipole interactions between a donor molecule and an acceptor molecule, and it can occur if the emission spectrum of the donor overlaps the absorption spectrum of the acceptor (Fig. 1.20). The energy transfer from an excited *donor molecule* (D*) to another *acceptor molecule* (A) happens according to :

$$D^* + A \longrightarrow D + A^* \tag{1.6}$$

The transfer rate is defined as :

$$k_T = k_D \left[\frac{R_F}{r} \right]^6 \tag{1.7}$$

Where k_D is the emission rate constant in the absence of transfer, r is the distance between the donor and the acceptor and R_F is the Förster radius defined as the distance at which the probability of transfer and total de-excitation probability of an excited molecule are equal. The transfer rate varies with r^{-6}, making FRET a distance sensitive technique. The transfer rate is defined as :

$$\phi_T = \frac{k_T}{k_D + k_T} \tag{1.8}$$

Using (1.7) the transfer efficiency can be expressed in terms of the ratio $\frac{r}{R_F}$:

$$\phi_T = \frac{1}{1 + \left(\frac{r}{R_F}\right)^6} \tag{1.9}$$

Note when the donor-acceptor distance is equal to R_F the transfer efficiency is equal to 50%. This can be used to experimentally determine Förster radius, which is usually in the range of 1-10 nm. R_F depends on the dielectric constant of their medium, the relative orientation of the molecules and most importantly the overlap between the **emission** spectrum of the donor and the **absorption** spectrum of the acceptor.

FRET has become a very popular technique in biology as it makes monitoring the relative positioning of two fluorescently labelled molecules with optical methods possible, hence the nickname *the spectroscopic ruler*. This means it is able to detect phase separation and domain formation that some times can be smaller than the optical microscopy resolution limit [60].

Fluorescence recovery after photobleaching FRAP

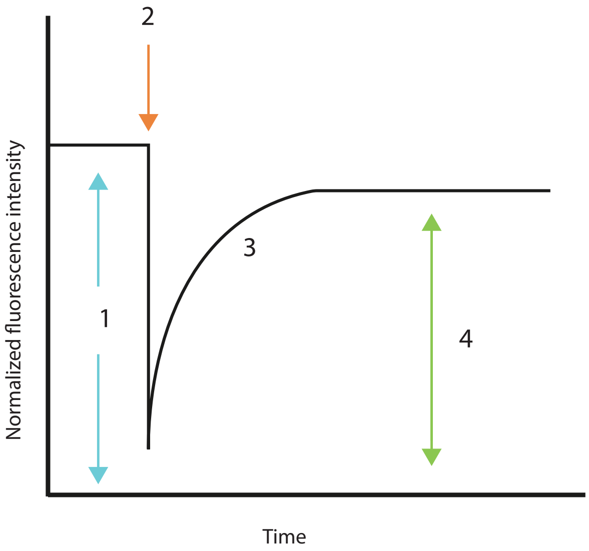

Figure 1.21: Data collecting during a FRAP experiment. The fluorescence intensity is uniformly distributed (1). Then photobleaching occurs (2), diminishing the fluorescent signal. Over time, the amount of fluorescence in the photobleached area increases as unbleached molecules diffuse into this area (3).Eventually uniform intensity is restored (4). The diffusion coefficient is determined by the slope of the curve (3). The steeper the curve, the faster the recovery and therefore, the more mobile the molecules.

Fluorescence recovery after photobleaching (FRAP) is simple an direct method for measuring long range lateral diffusion of lipids in membranes. FRAP measurements of lipid diffusion give an overview of the fluidity of the membrane. Thus, FRAP helps detecting phase transition and lipid composition. The principle of this technique is to attach a lipophilic fluorescent probe to the system in question (such as membranes). Under normal illumination intensity, an image of the system is determined by detecting fluorescence emissions using confocal microscopy. Applying a light pulse (short period) with high intensity on a specific region will result in the bleaching of the probes and therefore extinction of the fluorescence in the respective area (dark spot). The diffusion of the molecules in out and out of the bleached spot causes the restoration of the fluorescence signal (Fig. 1.21) [61, 62]. To determine the diffusion coefficient, one must solve the diffusion equation in 2D for the following initial conditions:

- The bleaching is uniform (square-well) inside the area of radius w assuming it is circular.

- The bleaching beam is Gaussian. That means, the intensity is a 2D gaussian distribution with a width w.

The lateral diffusion coefficient D can be related to the bleached area radius w and the recovery half time $\tau_{1/2}$

$$D \propto \frac{w^2}{\tau_{1/2}} \tag{1.10}$$

Fluorescence recovery after photobleaching provides a direct measure of the diffusion coefficient. However, it requires the averaging over large number of molecules. Imaging is done using confocal microscopy. Because of that, the spatial resolution of the method is limited to the diffraction limit of light ($\sim$ 250 nm), and fails to detect microdomains [26, 63]. The best use of FRAP is on large ordered systems where it can be considered that the size of bleached spot much smaller than the system, making the calculations much simpler.

Single-Molecule Fluorescence Miscroscopy

Single-molecule detection (SMD) of individual fluorescent probes allows the observation of molecules in their environment without having to average over an ensemble of molecules. Depending on the experimental condition, resolution up to 10 nm can be achieved [64]. This level of accuracy makes this technique useful for detecting heterogeneities in he membrane.

The objective of SMD is the tracking of the trajectories of individual fluorescent probes. Analysing these trajectories yields the lateral diffusion coefficient and as a result, the dynamical state of the system [65]. To extract the appropriate diffusion constant, two different cases must be considered whether the tracer diffuses in an homogeneous membrane or heterogeneous structure (obstacles, domains) [66]. For a homogeneous membrane, the molecules perform random walks (Brownian motion), described by a linear relation between the mean squared displacement (MSD) and time (see below).

4 Time scale of lipid dynamics

As already mentioned, phospholipids self-assemble with non-bonded interactions (of the order of $\sim k_BT$) to form many structures, including bilayers. The weak forces binding lipids together are the reason of the fluid nature of the bilayers. The dynamical behaviour of bilayer lipids, driven by thermal fluctuations, span on a large time scale ranging from picoseconds to seconds and even hours for some out of plane motion.

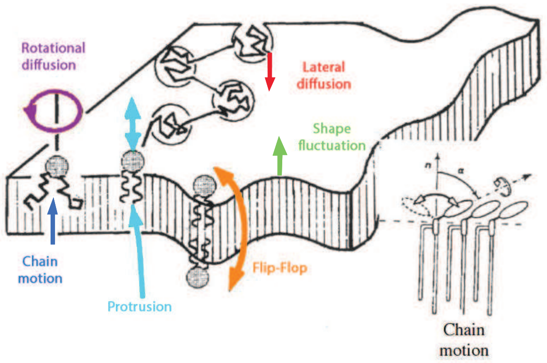

Figure 1.22: Individual lipid movement in a bilayer, chain conformational move, rotation along the lipid axis, protrusion, lateral diffusion and flip-flop [67].

The rotational diffusion of carbon-hydrogen bonds in the $\mathbf{CH_2}$ groups in the hydrocarbon chains is one the fastest dynamical processes (Fig. 1.23). The correlation times between conformations measured by NMR and spectroscopy techniques [68], reveal times in the order of few picoseconds ($\sim 2.10^{-11}$s) [69]. Although it can be slower in the case of saturated lipids ($\sim 3-8.10^{-11}$s) [69] as well as for lipids in membranes in the gel phase. The rotational relaxation (wobbling and principal axis rotation) of lipids in bilayers is much slower $\sim 10^{-8}-10^{-7}$ s [70]. The dynamical processes that we consider in more detail will be the lateral diffusion of lipids. The measured value of the lateral diffusion coefficient D depends on the length scale considered. For a fluid membrane, the diffusion coefficient $D \sim 1-10\mu\text{m}^2/\text{s}$ [71]. Thus, it takes lipids less than a minute to explore a typical cell membrane with a diameter of 10 μm. However, this time increases significantly in the more ordered membrane phases, as for instance the gel phase, with $D \sim 10^{-2}\mu\text{m}^2/\text{s}$ [72]. Heterogeneities, domains and other obstacles affect the lateral mobility of lipids and the time needed to visit the membrane. In addition, lipids need about 10 ns to diffuse over its own size (fraction of a nm). Slower dynamics consists of lipids switching leaflets, called *flip-flop* with a time scale that range from hours to days [73]. The translocation of lipids in biological membranes is essential to its function and can be accelerated by the presence of special proteins called flippase [74, 75]. In model bilayers or numerical simulations, this slow process is accelerated by the formation of pores making the time scale accessible through experiments and powerful computers [76, 77]. Collective motions such as undulations of the bilayer and domain diffusion ($D \sim 10^{-3}\mu\text{m}^2/\text{s}$) take place in the membrane [78].

Lipid self-diffusion corresponds to the random displacements of a single "tagged" lipid molecule in a fixed reference frame. On time and length scales large enough, this

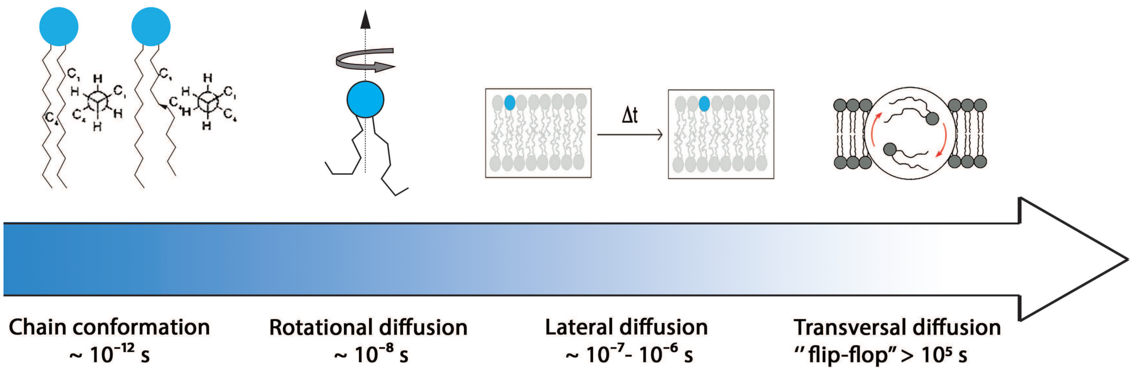

Figure 1.23: Hierarchy of the lipid motions in a bilayer, from the fastest (chain conformational transition) to the slowest (transverse diffusion).

motion belongs to the general class of Brownian motion, or random walk. On very short times, however, this motion is affected by intramolecular degrees of freedom and interaction with the neighbours.

The simplest characterization of a lipid self-diffusion is the mean-squared displacement (MSD). Denoting $x(t), y(t)$ the lateral (in plane) coordinates of the lipid center of mass, the MSD is a time correlation function defined as

$$g_{MSD}(t) = \left\langle (x(t) - x(0))^2 + (y(t) - y(0))^2 \right\rangle \tag{1.11}$$

The asymptotic behavior of g_{MSD} is expected to be $4Dt$, linear in time, with D the diffusion constant.

An ideal Brownian motion would correspond to a pure linear behaviour $g_{MSD}(t) = 4Dt$. At short and intermediate times, deviations from such a linear law reveal non trivial features of the lipid diffusive motion (heterogeneities, corral confinement, hydrodynamic and collective effects). The case $g_{MSD} \sim t^{\alpha}$ with $\alpha < 1$ is referred as anomalous diffusion or subdiffusion.

Chapter 2

Molecular Dynamics of bilayers

In addition to experiments and techniques which for some have been mentioned earlier, computer simulations have long been used to analyse the molecular structure and dynamics of membranes. Since the first numerical simulation of a liquid in 1953 [79], the field of computer simulations has enjoyed rapid advances, resulting in a continued growth in the field of membrane physics. These developments allow simulations to access time and length scales in which the comparison with experimental measurements can be made. Because of the dual role of simulations, connecting models and theoretical predictions on the one hand, and experimental results on the other, they are sometimes called *computer experiments*.

Monte Carlo sampling techniques are extensively used to simulate various systems, and are very helpful for simulating for instance fluids on lattices [80] and phase transitions. They are restricted in principle to thermal equilibrium properties of membranes.

In the following we will limit ourselves to describing the Molecular Dynamics approach, with particular attention to the aspects essential when simulating membranes.

1 Introduction to MD simulations

The molecular dynamics simulation method is based on integrating Newton's second law or the classical equations of motion.

$$\ddot{\boldsymbol{r}}_{\boldsymbol{i}} = \boldsymbol{f}_i/m_i; \qquad \boldsymbol{f}_i = -\frac{\partial U}{\partial \boldsymbol{r}_i}. \tag{2.1}$$

where $\boldsymbol{f}_i$ is the force exerted on particle i of mass m_i and acceleration $\ddot{\boldsymbol{r}}_{\boldsymbol{i}}$. The force derives from the potential energy of the system $U(r^N)$, where $r^N = (r_1, r_2, ...r_N)$ represents the complete set of $3N$ atomic coordinates. Once the force on each atom is known, it is possible to determine the acceleration of each atom in the system. Computing trajectories, involves solving a system of $3N$ second-order differential equations (2.1), or $6N$ first order differential equation (A1.12).

Discrete integration schemes A typical method for solving ordinary differential equations such as eq.(2.1) is the finite difference method (FDM). The scheme is as follows: knowing the molecular positions, velocities at time t, we attempt to determine the positions, velocities and other dynamic information at a later time $t+\delta t$, to a sufficient degree of accuracy. A Taylor' s series expansion abound t yields

$$\boldsymbol{r}(t+\delta t) = 2\boldsymbol{r}(t) - \boldsymbol{r}(t-\delta t) + \ddot{\boldsymbol{r}}(t)\delta t^2 \tag{2.2}$$

Eq.(2.2) is known as the *Verlet algorithm*. This method gives the position of each atom based on the current position and force, along with the previous position. Notice that the velocities are not needed to calculate the trajectory. However, they are used for the calculation of the kinetic energy and the pressure. The velocity may be expressed as

$$\dot{\boldsymbol{r}}(t) = \frac{\boldsymbol{r}(t+\delta t) - \boldsymbol{r}(t-\delta t)}{2\delta t} \tag{2.3}$$

Variations of the basic *Verlet* algorithm exist that differ in the velocity definition, such as the *leap-frog* scheme and *velocity Verlet*.

$$\textit{leap-frog}: \qquad \boldsymbol{r}(t+\delta t) = \boldsymbol{r}(t) + \delta t\dot{\boldsymbol{r}}(t+\frac{\delta t}{2}) \tag{2.4}$$

$$\dot{\boldsymbol{r}}(t+\frac{\delta t}{2}) = \dot{\boldsymbol{r}}(t-\frac{\delta t}{2}) + \delta t\,\ddot{\boldsymbol{r}}(t) \tag{2.5}$$

These integration methods result in a dynamics over a discrete set of evenly distributed times t_i, with a so-called time step $\Delta t = t_{i+1} - t_i$. This is therefore a discrete dynamics, which only approximate the real dynamics in the limit of small enough intervals Δt. The Verlet scheme, despite its relative simplicity, performs remarkably well for sampling molecular trajectories. This is usually attributed to its time-reversibility (as in the real dynamics) and its phase-space volume preserving properties (the Liouville theorem is respected). These are important criteria for molecular dynamics, that some more complex numerical schemes might fail to fulfil.

From the trajectories, the average values of any observable can be determined, as a time averages over a large number N of discrete steps:

$$\langle\mathcal{O}\rangle_{\text{microcanonical}} = \lim_{N_t\to\infty}\frac{1}{N_t}\sum_{i=1}^{N_t}\mathcal{O}(t_i) \tag{2.6}$$

This time average should tend to the microcanonical ensemble average of the physical observable $\mathcal{O}$, by a convergence process known as ergodicity. The method is deterministic once the positions and velocities of each atom are given, the state of the system can be predicted at any time, whether in the future or in the past (Fig. 2.1).

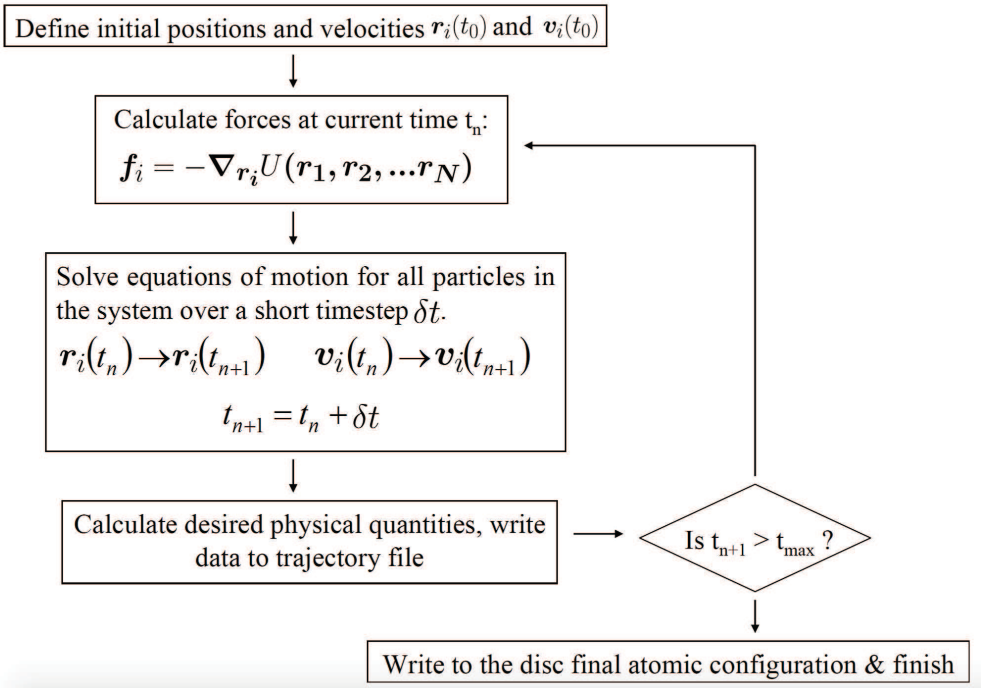
Define initial positions and velocities $\boldsymbol{r}_i(t_0)$ and $\boldsymbol{v}_i(t_0)$
Calculate forces at current time t_n:
$\boldsymbol{f}_i = -\boldsymbol{\nabla}_{\boldsymbol{r}_i} U(\boldsymbol{r}_1, \boldsymbol{r}_2, \ldots \boldsymbol{r}_N)$
Solve equations of motion for all particles in the system over a short timestep δt.
$\boldsymbol{r}_i(t_n) \rightarrow \boldsymbol{r}_i(t_{n+1})$ $\boldsymbol{v}_i(t_n) \rightarrow \boldsymbol{v}_i(t_{n+1})$
$t_{n+1} = t_n + \delta t$
Calculate desired physical quantities, write data to trajectory file
Is $t_{n+1} > t_{max}$?
Write to the disc final atomic configuration & finish

Figure 2.1: The general scheme of a discrete MD simulation. (a) predict the positions, velocities, accelerations etc., at a time t + δt, using the current values of these quantities; (b) evaluate the forces, and hence accelerations, from the new positions; (c) calculate any variables of interest, such as the energy, virial, order parameters, ready for the accumulation of time averages, before returning to (a) for the next step.

Force fields The energy function, or classical Hamiltonian, is essential to molecular dynamics simulations and the above algorithms (2.1) and (2.2). Intra- and intermolecular interactions must be faithfully represented by a function of the coordinates. The energy function can be arbitrary, but is often chosen in order to facilitate the analytical and numerical determination of the forces. The number of parameters in the energy function should be as small as possible for computational efficiency, but at the same time, sufficient to accurately describe the system.

To serve that purpose, many so-called force fields exist nowadays, each one designed for a specific model. Some of the popular programs (force field families) for biomolecular dynamics simulations are CHARMM [81], AMBER, GROMOS [82].

In addition to all-atom force fields, there exists coarse-grained force fields such as VAMM and MARTINI.

The expression for the potential energy function used in these force fields usually assumes the following form

$$U = U_{nb} + U_{bond} + U_{angle} + U_{torque} \tag{2.7}$$

where U_{nb} is the non-bonded energy, U_{bond}, U_{angle} and U_{torque} are the intramolecular energies (atom bonding, bending potential, dihedral terms). These intramolecular terms involve three and four bodies interactions. As an alternative to rigid bonding, it is also possible to enforce constraints on the relative distances between atoms. The advantage over a rigid bond potential, is that the latter causes high frequency vibrations which require small time-steps to be integrated. Such constraints for instance are used to simulate the ring structure of cholesterol molecules, but will not be necessary in our simulations.

Periodic boundary conditions (PBC) Computers can only simulate finite systems. It is therefore necessary to confine the system into a finite size simulation box, which for soft matter systems can usually be chosen as an orthogonal cell with size (L_x, L_y, L_z). If one chooses to introduce hard confining boundaries, the simulated system becomes inhomogeneous, with sizeable boundary effects. To overcome this problem, the best solution is to introduce periodic boundary conditions (PBC). Each atom leaving the cell on one side is immediately reintroduced at the opposite side with its velocity unchanged. Another way of viewing a periodic system consists in replicating by translation multiple copies of the original simulation cell. Each atom, or bead, located at (x, y, z) has an infinite number of “images” occupying all sites $(x + mL_x, y + nL_y, z + pL_z)$, where (m, n, p) can be any triplet of algebraic integers. As a result, the simulated periodic systems remains homogeneous and all points are equivalent. This however does not mean that finite size effects are absent.

Some aspects must be handled with care when using periodic boundary conditions. As there are many replicas associated with each bead, one must make sure that each atom does not interact more than once with any other atom, or with itself. For that, the minimal image convention states that each atom i does not interact directly with atom j, but with the closest image of atom j. The role of i and j can naturally be exchanged. In other words, the distance $r_{|ij|}$ between i and j that matters is

$$r_{|ij|} = \min_{(m,n,p)} ||\vec{\mathbf{r}}_j - \vec{\mathbf{r}}_i - mL_x - nL_y - pL_z|| \tag{2.8}$$

This are the relative distances $r_{|ij|}$ that are fed to the intermolecular potential. For consistency, the range of the pairwise (or intramolecular) interactions must be shorter than the smallest half-size of the simulated system $\min(L_x/2, L_y/2, L_z/2)$. When this condition is fulfilled, two images cannot compete for interacting with a given atom. If at two consecutive times, two different images of an atom j happen to interact with a given atom i, there is in between a time lapse where atoms i and j are out of range and non-interacting.

Periodic boundary conditions also pose a problem for long range electrostatics interactions. These interactions cannot be truncated without deeply altering the physics of the simulated systems. They therefore require a specific treatment in order to add properly the contributions of all periodic images. This is usually handled by the simulation software. In our simulations, such treatment of long-range forces is not necessary.

Neighbour list For computational efficiency, the range of the non-bonding interactions should be as small as reasonably possible. As a result, each bead or atom interact only with partners located within a sphere of radius r_c (cut-off radius). The number of interacting pairs, and consequently the computational effort, grows only linearly with the number of atoms or the size of the simulated system. This is true in practice if one knows which are the atoms pairs that do actually interact. The original idea of Verlet is to maintain a list of neighbours to save time when computing the forces (the most demanding step of a simulation). This list of neighbours contains for each atom the list of all other atoms (or images) occupying a sphere of radius r_v larger than the cut-off size r_c. The list of neighbours must be updated periodically at a frequency that depends on $r_v - r_c$ and on the discrete time step Δt.

Coupling with a thermostat Integrating Newton's equation with a Verlet scheme only samples the microcanonical ensemble, or constant energy ensemble. In addition, the total energy is not exactly conserved in the case of long trajectories due to time discreteness. It is necessary to reset the total, or the kinetic energy from time to time if one wishes to preserve it along the simulation. One elegant way to get around this difficulty is to couple the system to a thermostat.

A thermostat maintains a constant temperature, and inject or pump energy to the system according to the canonical ensemble statistics. If successful, the time averages of the observables of interest (kinetic energy, virial pressure) converge towards their canonical average. The thermostats may also stabilize systems which otherwise would crash due to sharp repulsive forces. This sometimes allow to increase the integration time steps Δt compared with the case of pure Newtonian dynamics.

Coupling to a thermostat is achieved by introducing additional degrees of freedom to the system. These additional degrees of freedom should be only weakly coupled to the system coordinates in order for the trajectory to remain close to the Newton's form, and the energy of the system to vary slowly.

In this work, the thermostat used are Nose-Hoover [83] and V-Rescale [84]. They both ensure that both energy average and energy fluctuations are consistent with the canonical ensemble.

Coupling with a barostat Barostats allow the simulation box size to fluctuate, and enforce a constant average pressure onto the system. For isotropic systems, they allow the volume V to fluctuate while maintaining the pressure approximately constant. Pressure, in molecular dynamics simulations, is related to the a stress tensor observable $\sigma(\mathbf{v}_i, \mathbf{r}_i)$ function of the instantaneous velocities and positions.

The system is subject to homogeneous rescaling of coordinates, with the volume variations subject to negative feedback response, coupled to the difference $\sigma - p$ between the actual isotropic stress σ and the pressure target p. When simulating a bilayer, it is not enough to consider an isotropic barostat, as otherwise the bulk compressibility of the system would dominate the volume fluctuations. It is necessary for the membrane to adjust freely and independently its lateral size L_x and transverse size L_z. An anisotropic barostat lets the system evolve with independently fluctuating lateral and transverse sizes. If the lateral and transverse pressures are set equal, the simulated membrane system should display no lateral stress or surface tension.

Parallel computing and coarse-graining All the modern simulation packages are designed for running on clusters of parallel nodes. This means that one can extend the geometrical size of the simulation box with only marginal losses of performance, provided the computing resources are of sufficient size. It is now possible for instance to simulate the motion of millions of atoms over billions of time steps.

There are however two limits, not to mention the availability of the computing resources. First, large systems may take much longer to thermalize, especially if dominated by hydrodynamic interactions. Long wavelength undulations of membranes, for instance take a very long time to relax. Parallelization cannot make a system thermalizing faster. Second, the recorded trajectory files grow linearly with size and simulation time. The storage and analysis time of huge trajectory files can be a practical limitation to the actual size of the simulations.

Coarse-graining is a procedure where atomic details are removed in favor of a coarser description involving supra-atomic collective coordinates. This has the effect of speeding up simulations by a very significant amount due to several reasons:

- the number of degrees of freedom (number of beads) is reduced, and so is the computation time of the interactions between beads.
- the time step Δt can be increased by a significant factor.

- the intrinsic relaxation dynamics of the system is faster, because mutual interactions are smoothed.

A speeding up factor by a thousand is reported for lipids coarse-graining. Only 15 beads are necessary instead of typically 130 explicit atoms. The time step can be increased from 2 fs to sometimes 40 fs. Intramolecular barriers such as chain isomerization potential are no longer present. Unfortunately, the connection between the coarse-grained numerical time and the physical time is lost in the process.

We discuss in Chapter 3 a situation, the pyrene excimer formation dynamics, where it is possible to establish a connection between the coarse-grained time and the experimental dynamics.

2 The Martini coarse-grained force field

In the following, we give a brief description of the *The Martini coarse-grained force field*, considering that all MD simulations done during this Thesis were based on it.

All atoms (AA) simulations are nowadays capable of reaching biologically relevant timescales (beyond the microseconds and even the milliseconds [85]). However, reaching those time scales requires a massively parallel supercomputer. In addition, the simulation of long timescales constrains the system size. To overcome these limitations, a natural strategy consists in simplifying the AA model, in such a way that the main structural properties and the essence of the interactions are preserved.

2.1 Model

The Martini model is a coarse-grained (CG) force field for biomembranes simulations. Using a chemical building block principle and *top to bottom* approach, the force field has been parameterized in a systematic way to reproduce thermodynamic data, especially the partitioning of the building blocks between aqueous and oil phases [86]. The use of short range potentials as well as reducing the number of degrees of freedom make Martini CGMD very efficient, computationwise, able to reach length scales of the order of micrometer and timescales of the order of milliseconds.

The Martini model was initially designed to simulate lipids [5]. Since then, it has become a valuable tool to probe time scales and length scales beyond the AA model, yet flexible enough to be applicable to a large range of biomolecular systems. In the following, we present a description of the force field.

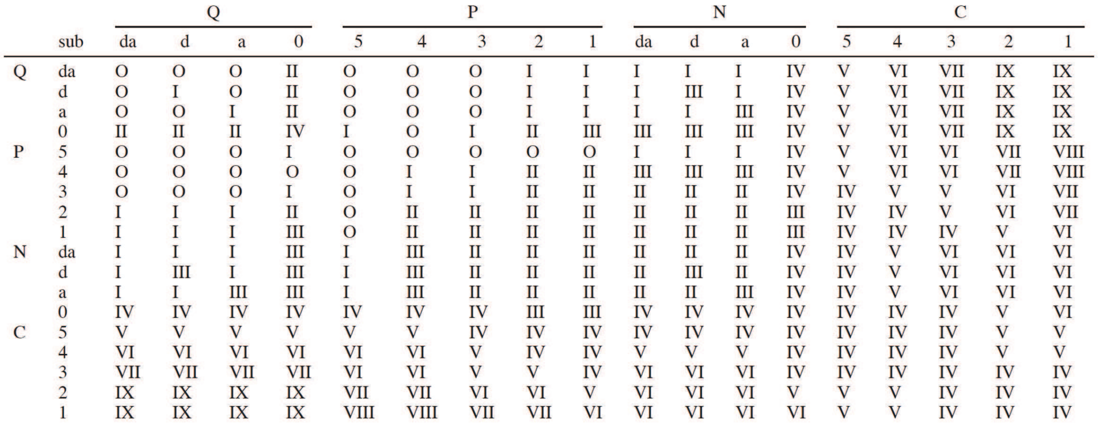

		Q				P					N				C				
	sub	da	d	a	0	5	4	3	2	1	da	d	a	0	5	4	3	2	1
Q	da	O	O	O	II	O	O	O	I	I	I	I	I	IV	V	VI	VII	IX	IX
	d	O	I	O	II	O	O	O	I	I	I	III	I	IV	V	VI	VII	IX	IX
	a	O	O	I	II	O	O	O	I	I	I	I	III	IV	V	VI	VII	IX	IX
	0	II	II	II	IV	I	O	I	II	III	III	III	III	IV	V	VI	VII	IX	IX
P	5	O	O	O	I	O	O	O	O	O	I	I	I	IV	V	VI	VI	VII	VIII
	4	O	O	O	O	O	I	I	II	II	III	III	III	IV	V	VI	VI	VII	VIII
	3	O	O	O	I	O	I	I	II	II	II	II	II	IV	IV	V	V	VI	VII
	2	I	I	I	II	O	II	II	II	II	II	II	II	III	IV	IV	V	VI	VII
	1	I	I	I	III	O	II	II	II	II	II	II	II	III	IV	IV	IV	V	VI
N	da	I	I	I	III	I	III	II	II	II	II	II	II	IV	IV	V	VI	VI	VI
	d	I	III	I	III	I	III	II	II	II	II	III	II	IV	IV	V	VI	VI	VI
	a	I	I	III	III	I	III	II	II	II	II	II	III	IV	IV	V	VI	VI	VI
	0	IV	IV	IV	IV	IV	IV	IV	III	III	IV	IV	IV	IV	IV	IV	IV	V	VI
C	5	V	V	V	V	V	V	IV	IV	IV	IV	IV	IV	IV	IV	IV	IV	V	V
	4	VI	VI	VI	VI	VI	VI	V	IV	IV	V	V	V	IV	IV	IV	IV	V	V
	3	VII	VII	VII	VII	VI	VI	V	V	IV	VI	VI	VI	IV	IV	IV	IV	IV	IV
	2	IX	IX	IX	IX	VII	VII	VI	VI	V	VI	VI	VI	V	V	V	IV	IV	IV
	1	IX	IX	IX	IX	VIII	VIII	VII	VII	VI	VI	VI	VI	VI	V	V	IV	IV	IV

Figure 2.2: Martini interaction matrix. Level of interaction indicates the well depth in the Lennard-Jones potential: : O, ϵ = 5.6 kJ/mol; I,ϵ = 5.0 kJ/mol; II, ϵ =4.5 kJ/mol; III, ϵ = 4 kJ/mol ; IV, ϵ = 3.5 kJ/mol; V; ϵ = 3.1 kJ/mol; VI, ϵ = 2.7 kJ/mol; VII, ϵ = 2.3 kJ/mol; VIII, ϵ = 2.0 kJ/mol; IX, ϵ = 2.0 kJ/mol. The Lennard-Jones parameter, σ = 0.47 nm for all interacion levels except level IX for which σ = 0.62 nm. (adapted form [86]).

Mapping The Martini model is based on a four-to-one mapping (Fig. 2.3). Four heavy atoms are represented by a single bead/interaction site). Hydrogen atoms are not considered because of their small size and mass. Small ring like structures such as cholesterol need a more detailed representation. Therefore they are mapped with higher resolution, usually a three non hydrogen atoms to one interaction center. Solvent is explicitly included. Martini water for example is modelled as a coarse-grained Lennard-Jones particle representing four real water molecules.

The four-to-one mapping was chosen as an optimum between computational efficiency on the one hand and chemical realism on the other hand. Mapping of water is consistent with this choice, as four real water molecules are mapped to a CG water bead. Ions are represented by a single interaction site, which consists of both the ion and its first hydration shell.

There are four main types of interaction sites:

- polar sites (P) represent neutral groups that would easily dissolve in water.
- nonpolar sites (N) represent groups that are partly polar and partly apolar.
- apolar sites (C) represent hydrophobic groups.
- charged sites (Q) represent ions and zwitterionic molecules.

In addition to bead types, subtypes are introduced. They can be either letters to represent hydrogen bonding capabilities (d = donor, a = acceptor, da = both, 0

= none), or numbers denoting the degree of polarity (ranging from 1 = low polarity to 5 = high polarity). In total we distinguish 18 particle types, forming the Martini building blocks (Fig. 2.2). For reasons of computational efficiency, in the MARTINI model all beads share the same mass of 72 amu (the mass of four water molecules) although, realistic masses can be assigned to the particles.

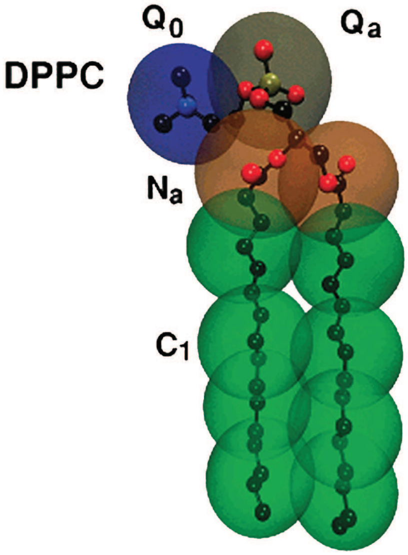

Figure 2.3: Mapping between the chemical structure and the coarse grained model for DPPC. The coarse grained bead types which determine their relative hydrophilicity are indicated (from [86]).

Non-bonded interactions

VDW interactions

The excluded volume between two beads i and j separated by distance r_{ij} is defined by a 6-12 Lennard-Jones potential (LJ) potential

$$U_{LJ}(r_{ij}) = 4\epsilon_{ij}\left[\left(\frac{\sigma_{ij}}{r_{ij}}\right)^{12} - \left(\frac{\sigma_{ij}}{r_{ij}}\right)^{6}\right] \tag{2.9}$$

where ϵ_{ij} is the depth of the potential, σ_{ij} is the distance at which the inter-particle potential is zero. The strength of the interaction ϵ_{ij} depends on the type of the particles i, j. The highest value of ϵ is for interactions between strongly polar groups and its lowest value is for interactions between polar and apolar groups, reflecting the hydrophobic effect. The parameter σ determines the effective bead size considered equal to 0.47nm for all normal particle types. For the special class of particles in ring structures, the LJ parameters are slightly reduced. The full interaction matrix is represented in (Fig 2.2).

Electrostatic interaction

In addition to the LJ interaction, charged groups (type Q), such the zwitterionic lipid head groups, present an elementary charge $\pm e$ and interact via a Coulomb potential. To account for the reduced set of partial charges and resulting dipoles that occur in an atomistic force field the Coulombic interaction are screened explicitly by introducing a relative dielectric constant $epsilon_r = 15$

$$U_el(r_{ij}) = \frac{q_i q_j}{4\pi\epsilon_0\epsilon_r r_{ij}} \tag{2.10}$$

Coulombic interactions are also truncated at a distance of $r_c = 1.2$ nm, which means that they are not strictly speaking long ranged, and do not require a specific treatment for images sums. In addition, the Coulomb potentials are shifted progressively to zero between 0 and 1.2 nm, as if implicit screening ions were present.

Non bonding Lennard-Jones interactions also are cut-off at a distance of $r_c = 1.2$ nm, and shifted progressively starting from 0.9 nm. In this way, discontinuity of the forces are avoided.

Bonded Interactions

Bonded interactions between chemically connected sites are represented by a set of weak harmonic potentials: bonds are described by $V_{bond}(R)$ and angular potentials $V_{angle}(\theta)$ describes the chain stiffness

$$V_{bond}(R) = \frac{1}{2}K_{bond}[R - R_{bond}]^2 \tag{2.11}$$

$$V_{angle}(\theta) = \frac{1}{2}K_{angle}[\cos(\theta) - \cos(\theta_0)]^2 \tag{2.12}$$

The LJ interaction are excluded between bonded particles, but not between second nearest neighbours. On average, bonded particles are closer to each other than non-bonded neighbours.

Overview of the *dioleoyl phosphatidylcholine* CG topology

Id	type	atom	charge
1	Q_0	NC_3	1.0
2	Q_a	PO_4	-1.0
3	N_a	GL_1	0
4	N_a	GL_2	0
5	C_1	C_{1A}	0
6	C_1	C_{2A}	0
7	C_3	D_{3A}	0
8	C_1	C_{4A}	0
9	C_1	C_{5A}	0
10	C_1	C_{1B}	0
11	C_1	C_{2B}	0
12	C_3	D_{3B}	0
13	C_1	C_{4B}	0
14	C_1	C_{5B}	0

i j k	angle	K_{angle}
2 3 4	120.0	25.0
2 3 5	180.0	25.0
3 5 6	180.0	25.0
5 6 7	180.0	25.0
6 7 8	120.0	45.0
7 8 9	180.0	25.0
4 10 11	180.0	25.0
10 11 12	180.0	25.0
11 12 13	120.0	45.0
12 13 14	180.0	25.0

Table 2.1: Details of the DOPC CG molecule. The force constant K_{angle} is equal to 25 kJ mol^{-1} with an equilibrium bond angle $\theta = 180\,\mathrm{deg}$ for aliphatic chains. The force constant for the angles involving the cis double bond is set to $K_{angle} = 45$ kJ mol^{-1}. The equilibrium angle remains at $\theta = 120\,\mathrm{deg}$.Bonded interactions were not presented here but they remain the same between different interaction sites, with an equilibrium distance $R_{bond} = \sigma = 0.47$ nm and a force constant of $K_{bond} = 1250$ kJ mol^{-1} nm^{-2}.

2.2 Applications of the Martini model

Nowadays, the Martini force field parameters extend to a variety of biomolecules, including lipids, proteins, sugars and nucleic acids. Martini molecules are constructed using the building block principle. The molecules are constructed by attaching beads (the building blocks) together. The entire philosophy behind Martini is that the carefully parametrized properties of the individual beads are able to reproduce the properties of the molecule as a whole. Validating this assumption requires comparisons to more detailed atomistic simulations or to experimental data. If a system could not be described by the standard Martini beads, further optimizations could be made due to the simplicity of the model, i.e. limited set of parameters, which makes it relatively easy to adjust or optimize the interactions.

Because of the flexibility and transferability of the Martini coarse-graining protocol, the list of applications has grown greatly. The force field can be used to characterize lipid membrane properties, protein-lipid interplay, self-assembly of soluble peptides and proteins, protein conformational changes, binding and pore-formation in membranes, structure and dynamics of polymers and interaction of nanoparticles with membranes, and the list goes on. However, clearly, lipid membranes are still central in the applications.

2.3 Limitations of the Martini model

The central issue of the Martini coarse-grained model is that it contains less detail than atomistic models. While improving the accuracy of the model can be achieved by adding back details, this also takes away, to a certain extent, its computational advantages.

Martini has a number of limitations. Some of Martini's limitations originates from coarse-graining at a fundamental level, such as the chemical and spatial resolution, which are both limited compared to atomistic models. The reduced number of degrees of freedom results in a shifted balance between entropy and enthalpy; and kinetics that is modified in an unpredictable way. Lipids such as DMPC (14 carbons) and DPPC (16 carbons) can be represented by the same Martini molecule, even though there is in reality a 20°C difference in their main fluid-gel melting temperature. Water beads, by bunching together 4 water molecules, cannot penetrate into the bilayer as individual water molecules would do in an AA model.

- Model resolution and accuracy: Martini can reproduce the thermodynamics of a large number of organic systems. However, the coarse-graining (mapping and range of interaction) limits the chemical resolution, the consequences of that are clear while investigating properties that are dependant on the length of the carbon chain, internal degrees of freedom as well as polarity.

- Effective time scale. Coarse-grained simulations accelerate the kinetics of the system. However, it is not always the same for all degrees of freedom [87]. While usually estimated as 4, some studies have shown accelerated kinetics of a factor varying between 1 and 22 [88].

- Free energies, enthalpies, entropies. Reducing the number of degrees of freedom affects the entropy of the simulation system, which is compensated for by reduced enthalpic terms in the model. This affect the temperature dependence of the model. Martini is designed for use between 20 and 50°C.

- The functional form of the non-bonded potential. The steep repulsion from using a 12-6 LJ potential results in an unwanted ordering. One of the consequences is the freezing of Martini water at room temperature.

2.4 Advantages of the Martini model

The Martini model is very well characterized due to its popularity and its large community of users. Many results are available for reference to compare with, and efficient configuration and analysis tools are available. Martini is based on the Gromacs simulation engine, which is one of the most user-friendly package for simulations, and one of the standard engine for biomolecular simulations in general.

The degree of coarse-graining preserves enough intramolecular details to make it an interesting tool in our work on excimer formation kinetics. It was also shown to describe appropriately the properties of peroxidized lipids.

Chapter 3

Excimer formation

1 Excimer formation mechanism

The word excimer is formed by the contraction of *excited* and *dimer*. A dimer here represents a non-covalent bound complex between two identical molecules. Excitation means that the electronic state of the molecule is an eigenstate with energy higher than the ground state.

An excimer is therefore a dimer made of two identical molecules, one of them being in an excited state, usually as a result of a photoexcitation process. When two different molecules participate to a complex, this one is referred as an exciplex.

The specificity of excimers is that the complex is only stable because one of the component is excited, and would not form with two molecules in their ground states. When the excimer return to its electronic ground state, the complex dissociates as the two original molecules are released. If in addition, both excited molecule and excited dimer display radiative deexcitation (*e.g.* fluorescence) the emission spectrum bears the signature of the conformation at the time of the photon escape. Excited monomer and excited dimer differ in their emission spectra.

Excimers and exciplexes have technical applications, as for instance the excimer/exciplex lasers, known for their tunable excitation wavelengths.

The complexes are formed as a result of the association/collision of a molecule in the excited state and a normal molecule. Isolated molecules will be referred as *monomers*. The diagram (3.1) shows the classical kinetics rates associated to such a dynamical process. Excimer formation is a bimolecular reaction, that can be

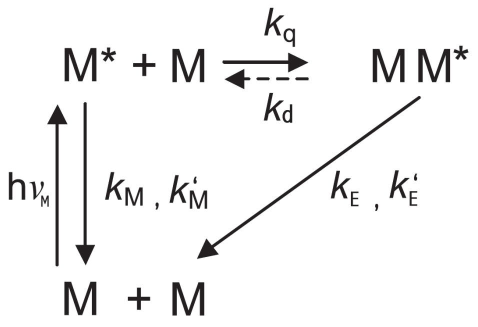

Figure 3.1: Excimer formation reaction.

represented by the following equations:

$$\mathrm{M} + \mathrm{M}^* \underset{k_d}{\overset{k_q}{\rightleftharpoons}} (\mathrm{MM})^* \tag{3.1}$$

$$\mathrm{M}^* \xrightarrow{k_M, k'_M} \mathrm{M} + h\,\nu_M \tag{3.2}$$

$$(\mathrm{MM})^* \xrightarrow{k_E, k'_E} 2\mathrm{M} + h\,\nu_E \tag{3.3}$$

where hv is the emitted photon, the subscripts M and E refer to monomer and excimer emissions. k and k' denotes radiative and nonradiative deexcitation rates respectively. k_q is the excimer formation rate (quenching rate) and k_d is the dissociation rate (usually considered negligible compared to k_q.

Many molecules can form excimers, and in particular the rigid aromatic hydrocarbon compounds. The fluorescence emission spectrum of the monomers (M), markedly differs from the emission spectrum of the excimers, or dimers (MM)*, i.e. the fluorescence band of an excimer is located at higher wavelengths than that of the monomer (Fig. 3.4).

The reason behind this is shown in fig.3.2. A system consisting of two molecules with one being in the excited state lowers its energy (exhibits a minimum) by forming the excimer.

In the excimer state, monomers need to be at a distance of a few Angstroms from one another (3.7 Å for pyrene). In the monomer state, molecules are dispersed in solution, and possibly far apart. Following excitation, an excimer forms if the excited monomer gets in close contact with a ground state monomer. The monomer lifetime must necessarily be larger than the average collision time. Excimer formation is efficient only if the yield of the collision process is high.

It is therefore assumed that excimer formation kinetics is diffusion controlled, or diffusion limited (rates k_q), represented on figure (3.3).

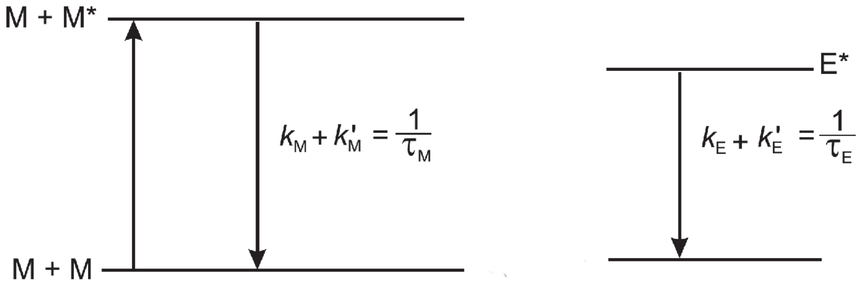
M + M*
M + M
$k_M + k'_M = \frac{1}{\tau_M}$
E*
$k_E + k'_E = \frac{1}{\tau_E}$

Figure 3.2: Energy gap between the first excited state and ground state for an excited monomer (left) and an excited excimer (right). Because $\nu_M \geq \nu_E$ the monomer fluorescence emission band occurs at shorter wavelengths than that of the monomer.

Pyrene excimers Pyrene is a hydrophobic polyaromatic molecule that is prone to forming excimers, and characterized by a long life-time of the order of 100 ns, compared with usual organic fluorescent dyes (usually $\sim$ 5 ns). The planar and rigid shape of the molecule are likely to favour the dimer formation, while the long lifetime is favourable in terms of diffusion limited processes. The spectrum evolution as a function of the concentration is shown in fig. (3.4).

One of the reasons which explains the high formation yield, is that excited molecules exert quite long-range interactions with ground state molecules. In addition, further attractive terms act on very short range [89]. Most treatments of the excimer formation kinetics, however, neglect these effects and assume that monomers diffuse as if they were non interacting.

Stern-Volmer (SV) kinetics assumes a time independent excimer formation rate obeying the following relations

$$\frac{\mathrm{d}[\mathrm{M}^*]}{\mathrm{d}t} = -(k_1 + k_q[\mathrm{M}])[\mathrm{M}^*] + k_d[\mathrm{MM}^*] \tag{3.4}$$

$$\frac{\mathrm{d}[\mathrm{MM}^*]}{\mathrm{d}t} = k_q[\mathrm{M}][\mathrm{M}^*] - (k_d + k_2)[\mathrm{MM}^*] \tag{3.5}$$

where k_1 and k_2 are the sum of the radiative and non-radiative processes for the monomer and excimer, respectively. For stable excimers, dissociation cannot occur during the lifetime of the excited state ($k_d \ll k_q$). Therefore, neglecting the reverse process and integrating first order differential equation with $[\mathrm{M}^*] = [\mathrm{M}^*]_0$ and $[\mathrm{MM}^*]_0 = 0$ at $t = 0$ as initial condition gives

$$[\mathrm{M}^*] = [\mathrm{M}^*]_0 \exp\{-(1/\tau_M + k_q[\mathrm{M}])t\} \tag{3.6}$$

The monomer fluorescence intensity is obtained by integrating

$$i_M(t) = k_M[\mathrm{M}^*] = k_M[\mathrm{M}^*]_0 \exp\{-(1/\tau_M + k_q[\mathrm{M}])t\} \tag{3.7}$$

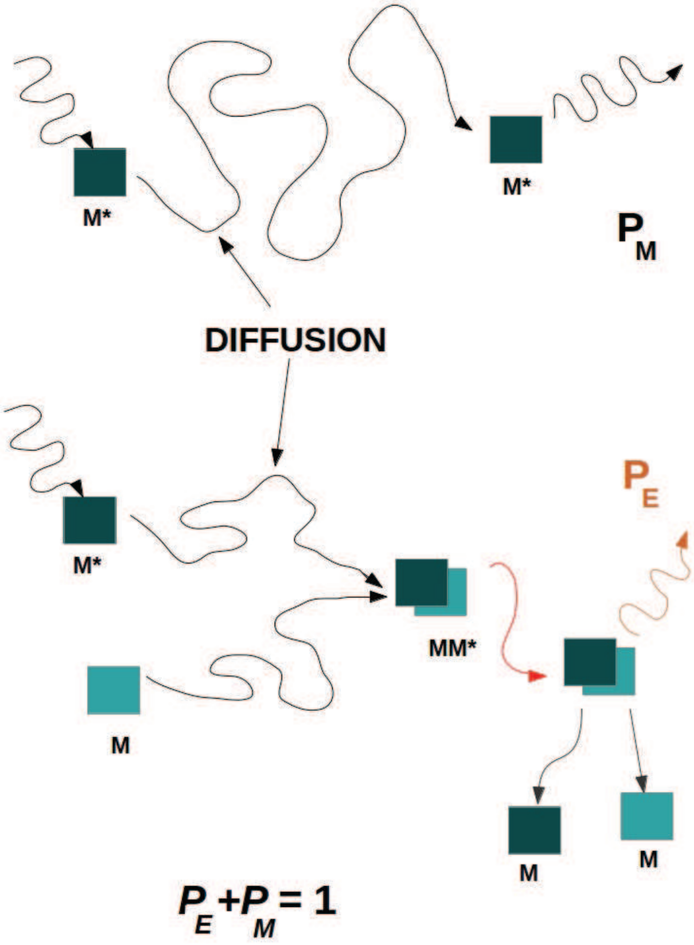

Figure 3.3: Competition between monomer and excimer deexcitation in a diffusion controlled reaction.

where k_M is the radiative rate constant of M* and $1/\tau_M = k_M + k'_M = k_1$. The fluorescence decay is thus exponential with a decay time $\tau = \tau_M[1 + k_q\tau_M[\mathrm{M}]]^{-1}$.

At the time of the excitation, fluorophores that are close to each other react at shorter times than those than need to diffuse before encountering another fluorophore. This will consequently affect the beginning of the fluorescence decay curve (short times). The so-called transient effect becomes more important with the concentration of the present quenchers (fluorophores) or the fluidity of the system, affecting the diffusion of the monomers. The consequence of these transient effects is a departure from the Stern–Volmer plot in which the fluorescence intensity is proportional to the concentration of M*. The decay intensity of the excited monomer

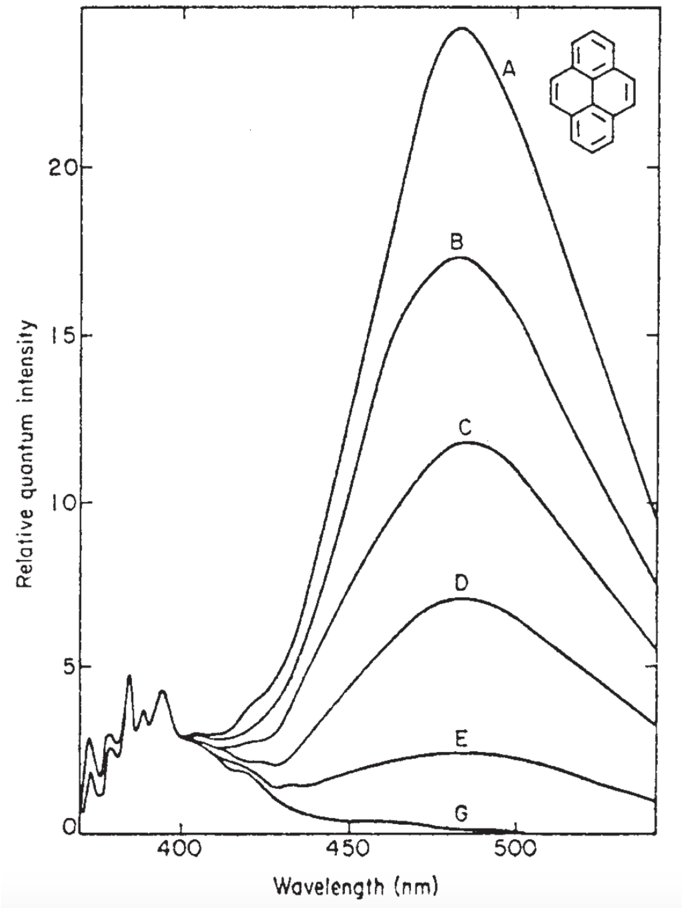

Figure 3.4: Fluorescence spectra of pyrene derivatives for different concentrations varying from G = 10^{-4} mol.L^{-1} to A= 10^{-2} mol.L^{-1}(adapted form [90]).

is no longer exponential. This why time resolved fluorescence spectroscopy can be used for studying the mobility of the monomer probes, for instance in membranes.

In general, for dynamic quenching processes, performing time-resolved fluorescence experiments in the absence and presence of a quencher provide a direct value of k_q. By measuring the fluorescence quantum yield in both cases leads to the Stern-Volmer relation:

$$\frac{\Phi_0}{\Phi} = \frac{I_0}{I} = 1 + k_q \tau_M [\mathrm{M}] \tag{3.8}$$

where Φ and Φ_0 are the fluorescence quantum yields in the presence and absence of a quencher, respectively. I and I_0 are the steady-state fluorescence intensities in presence and absence of a quencher. $k_q \tau_M$ is the Stern–Volmer constant. Plotting eq.(3.8) against the quencher concentration gives the Stern-Volmer constant if the plot showed a linear variation. Moreover, if τ_M is known then the excimer formation rate can be calculated [59].

In the case where the excimer formation process is much faster than the diffusion dynamics, the quenching rate constant is proportional to the diffusion rate and can be related to the translational diffusion using the simplified form of the Smoluchowski relation, valid for 3d processes:

$$k = 4\pi \mathcal{N} R_c D \tag{3.9}$$

where $\mathcal{N}$ is the Avogadro number divided by 1000, R_c is the distance of closest approach taken as the sum of the radius of the molecules and k in L.mol^{-1}.s^{-1}. D is the mutual (relative) diffusion coefficient given by the Stokes-Einstein relation

$$D = D_{\mathrm{M}} + D_{\mathrm{M}^*} = \frac{2kT}{f\pi\eta R_{\mathrm{M}}} \tag{3.10}$$

with η is the viscosity of the medium, and f is a coefficient that depends on the boundary conditions of the system, usually close to 6π. The translational diffusion depends on the viscosity of the system and provide information on the fluidity of the environment. However, it must take place in a time interval comparable to the excited state lifetime of the fluorophore (so-called experimental time window). For negligible transient effects, the quenching rate constant can be easily determined by measuring the fluorescence intensity or lifetime as a function of the quencher concentration; the results can be analysed using the Stern–Volmer relation (3.8).

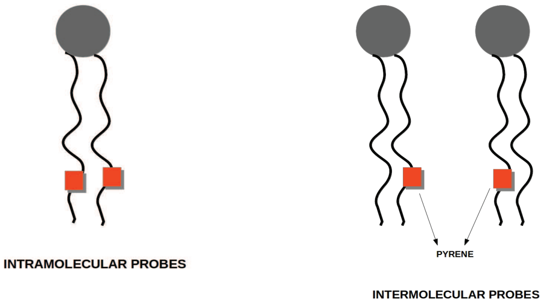

Figure 3.5: Presentation of intramolecular probes (left) and intermolecular probes (right) attached to phospholipids. The probes are represented by red cubes. Intramolecular probes are attached to the same lipid but on a different carbon chain while intermolecular probes are attached on a different lipid. In both cases, the reaction occurs when the distance separating the probes is smaller than a critical reaction radius.

Transient effects in the Smoluchovsky approach In reality, the excimer formation rate corresponds to a time dependent constant $k_q(t)$, for reasons mentioned above. The Smoluchowski theory for describing diffusion limited reactions is based on a reaction taking place as soon as the relative distance between the two molecules reaches a capture radius R_c [3]. The rate is obtained by imposing absorbing boundary conditions for species B, with species A kept at the center of the reference frame. The transient rate reads

$$k(t) = 4\pi N R_c D \left[1 + \frac{R_c}{(\pi D t)^{1/2}} \right] \tag{3.11}$$

There is behind this rate a hidden mean-field assumption which assumes that no correlation exists between the occurrence of a A-B reaction and the subsequent concentration fields [A](t) and [B](t), which remain homogeneous at all times.

Improvements upon the Smoluchowsky model exist, such as the Collins-Kimball theory [91] which assumes a distant dependant rate constant

$$k(r) = k_R \exp\Big(-\frac{r - R_c}{r_e} \Big) \tag{3.12}$$

where k_R is assumed to be proportional to the probability that the distance between the two monomers is in the interval $[R_c, R_c + \delta r]$, r_e parameter ranging between 0.5 and 2 $\mathring{A}$.

2 Two dimensional reaction rates and applications to membranes

The Naqvi result A derivation of the Smoluchovsky theory to 2d processes was introduced by Naqvi [92]. The result is not as simple as in the 3d case. In particular, the long-time behaviour of the Naqvi rate (the 2d equivalent of (3.11)) reads [93]:

$$k(t) = \frac{4\pi D}{\ln(4Dt/R^2) - 2\gamma_e} + \mathcal{O}(\ln(t)^{-2}) \tag{3.13}$$

Unlike in the 3d case, the rate constant decreases to 0 at long times. There is, strictly speaking, no diffusion limited rate constant in 2 dimensions.

Pyrene excimers as fluidity probes in membranes The excimer phenomenon is interesting as it reports on the collision dynamics of probe molecules embedded in a viscous fluid medium. The reaction is reversible (dimer dissociation) and the product can be detected spectroscopically (fluorescence emission intensity).

As for any dynamical quenching process, there is a strong concentration dependence of the emission curves. With the help of a model, it is possible to deduce the

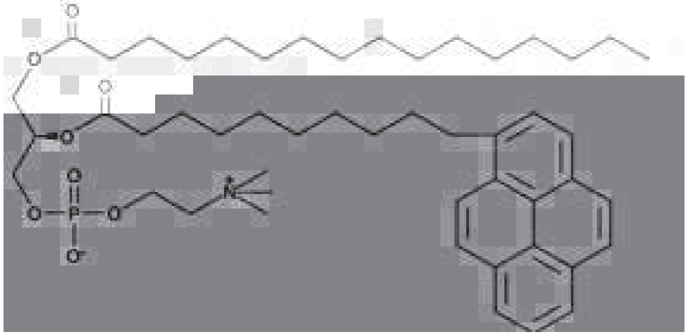

Figure 3.6: Phospholipid analogue with a pyrene group at the end of a 10 carbon chain

diffusion coefficient of the fluorescent probes from the continuous emission properties of solutions containing various probe concentrations. What is required is the ratio between the excimer and monomer emission intensity. By monitoring pyrene molecules dissolved in a bilayer, Galla and Sackmann measured in this way the fluidity of the membrane [94].

Such experiments were later repeated with pyrene derived lipid analogues, such as represented in Fig. 3.6, with the idea that the motion of the pyrene probe would be similar to the ones of the lipids. The use of pyrene derived lipids for understanding membrane dynamics is reviewed by Somerharju [95]. More generally, photophysical diffusion limited reactions are reviewed by Melo and Martins [96].

The model underlying the theoretical interpretation of the continuous intensity fluorescence of pyrene compounds is usually the Naqvi time-dependent reaction rate (3.13) or lattice based random walks. The simplest lattice model involves random walkers jumping until they occupy the central site, considered as the reaction site. Two dimensional random walks have been studied intensively, with analytical results available for the time distribution for the first passage of a walker at the origin [97]. More sophisticated models consider random walkers on hexagonal lattices, and reaction when the walker arrives next to the origin [6, 7]. Lipids are usually reduced to single points on a lattice.

The experimentally reported values of the lipid diffusion coefficients are often large. Sassaroli et al., for instance, report 11 $\mu\text{m}^2.\text{s}^{-1}$ for POPC at 20°C, using a random walk on lattice model for interpreting the data. The agreement with other techniques is better (3.1 $\mu\text{m}^2.\text{s}^{-1}$ for POPC at 25°C) when using the Naqvi theoretical rate for analyzing the shape of the time-resolved fluorescence intensity [98]. This suggests that the current interpretation framework might be improved by using a better model for modelling the reaction time statistics.

Excimer formation rates from molecular dynamics In this thesis, we show how in practice MD simulations can be used to interpret the excimer formation rate of pyrene-lipid analogues, and derive a lipid diffusion coefficient D. We also determine experimentally the acceleration factor of the Martini model at a given temperature, regarding processes taking place on the 10^2 ns time scale.

The starting point is the observation that once a molecule is excited, there is a probability p_M that the molecule deexcites as a monomer, and a complementary probability $p_E = 1 - p_M$ that it deexcites as an excimer. These probabilities are experimentally available as relative intensity emission rates $J_M(x)$, $J_E(x)$, with x the molar fraction of the probes in the bilayer.

p_M is then related to a survival probability $P_c(t)$ by the formula

$$p_M = \int_0^\infty \frac{\mathrm{d}t}{\tau_M} P_c(t) \exp\left(-\frac{t}{\tau_M}\right) \tag{3.14}$$

with τ_M the lifetime of the monomer in the dilute limit. $P_c(t)$ is the probability that an excited monomer has not yet met a ground state monomer after a time t following excitation.

The next step is to estimate $P_c(t)$ for arbitrary concentration x from realistic coarse-grained molecular dynamics trajectories. This approach does not make assumption on the Brownian dynamics of the lipids, and potentially include intramolecular and collective motion. We assume that pyrene-lipids behave the same as regular lipids. In other words, substituting a lipid for a probe is neutral (our neutrality assumption).

Then we perform a sampling of collisions *a posteriori* by relabelling lipids in multiple ways, but using the same trajectory. This give us an accurate sampling of the survival probability $P_c(t)$ associated for a pair of probes in a given sample containing, for instance 256 lipids per leaflets. What remains is to relate the general survival probability $P_c(t)$ (any number N of lipids and any fraction x of probes) to the previous reference case. This is done by making two more assumptions: a size-scaling assumption (for comparing systems with different sizes) and an independent pair assumption (when many probes compete for a single excited monomer).

We compare the excimer formation in the presence and in the absence of interleaflet excimer formation. Time-temperature superposition is also discussed. The main results are presented in our manuscript entitled “Excimer formation of pyrene labeled lipids interpreted by means of coarse-grained molecular dynamics simulations”, and reproduced in the next Chapter.

The numerically generated trajectories are used to compute the mean squared displacement, from which the so-called coarse-grained diffusion coefficient D_{CG} is determined as shown in fig. 3.7. As a result, and using the same experimental data as [6, 7], we reduce the initially reported values of D by a significant amount: for instance, D=4. $\mu\mathrm{m}^2.\mathrm{s}^{-1}$ in the absence of interleaflet excimer formation corresponding

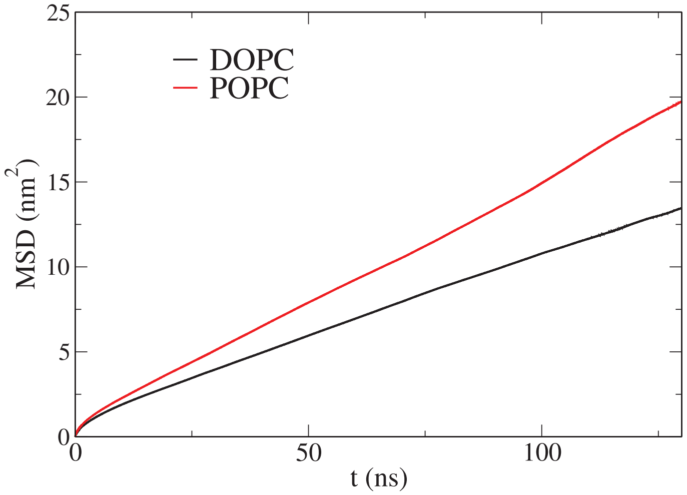

Figure 3.7: Mean squared displacement for DOPC and POPC bilayers at 283k and 293k respectivelly. The MSD was calculated using the GROMACS generated trajectories. The slope of the curves yields the "*numerical*" lateral diffusion coefficient D_{CG} equal to $26\,\mu m^2 s^{-1}$ in the case of DOPC bilayers and $36\,\mu m^2 s^{-1}$ for POPC bilayers.

to an acceleration factor $f = 9$ for POPC at 20°C.

3 Principle of the calculation

Classical treatment Excimer formation can be seen as dynamical quenching of excited monomers. The mean-field excimer formation rate $M + M^\star \to E^\star$ reads $-k[M][M^\star]$, with $[M]$ proportional to the probe molar fraction x. When a single excited monomer is considered, the average decay of an excited monomer reads

$$\frac{\mathrm{d}P_M}{\mathrm{d}t} = -\frac{P_M}{\tau_M} - KxP_M \tag{3.15}$$

with $Kx = k[M]$, τ_M the monomer lifetime in the diluted limit, and $P_M(t)$ the survival probability of the excited monomer at a time t following excitation. In this framework, the survival P_M decays exponentially. Introducing, as in Vauhkonen et al., and Sassaroli et al. the fraction $x^\ddagger$ which makes the rate $Kx^\ddagger$ equal to τ_M^{-1}, one finds

$$P_M(t) = \exp\left(-\frac{t}{\tau_M}(1 + \frac{x}{x^\ddagger})\right) \tag{3.16}$$

The relative intensity of the monomer emission line is

$$J_M = \int \frac{\mathrm{d}\,t}{\tau_M}\, P_M(t) = \frac{1}{1 + x/x^\ddagger} \tag{3.17}$$

or equivalently

$$\frac{1}{J_M} = 1 + \frac{x}{x^{\ddagger}} \tag{3.18}$$

The main conclusion is that a linear plot J_M^{-1} vs x is synonymous to exponential decay (Stern-Volmer behavior). Deviation from this linear law reveals a non exponential decay.

In his extension of the Smoluchowski theory to 2d membrane reactions, Naqvi obtains a time dependent rate $K(t)x$, relative to the excited time t. This rate takes into account the transient depletion of reacting probes at the vicinity of the excited molecule. The properties of the random 2d trajectories insures that the decay of P_c is non exponential. However, the calculation is restricted to ideal Brownian motion (Wiener process) of the reacting group.

Reduction to a reference system The connection with the titration curve is made thanks to the relation

$$J_M(x) = \int \frac{\mathrm{d}t}{\tau_M} P_c[x](t) e^{-t/\tau_M} \tag{3.19}$$

where P_c is a x dependent collision survival probability.

Let us assume first that no interleaflet association is allowed and let us consider a system; a membrane leaflet in our case; of N_t lipids containing N_p probes. At time $t = 0$, one of the probe is excited and the $N_p - 1$ remaining probes compete for "quenching" (by dimerization) the excited probe. We assume that the dimerization takes place when the terminal subgroup of a probe penetrates into a sphere of radius ρ_c centered around the excited subgroup. $P_s(\rho_c, N_p, N_t; t)$ represents the average survival probability for this system, *i.e.* the probability that none of the $N_p - 1$ remaining probe has "reacted" with the excited probe.

The independent pair approximation consists in neglecting three-bodies (two probes and one excited probe) interactions. The elementary process is the single pair survival probability $P_s(\rho_c, 2, N_t; t)$, with only one excited and one ground state probe present. If the quenching process is pairwise, the survival for $N_p = 3$ is the product of the survival of the first and the second reacting pair.

$$P_s(\rho_c, 3, N_t; t) = P_s(\rho_c, 2, N_t; t)_{\text{pair 1}} \times P_s(\rho_c, 2, N_t; t)_{\text{pair 2}} \tag{3.20}$$

Averaging over all the possible distributions of initial positions and trajectories of the pairs enables us to express $P_s(\rho_c, 3, N_t; t)$ in terms of $P_s(\rho_c, 2, N_t; t)$.

$$P_s(\rho_c, 3, N_t; t) = P_s(\rho_c, 2, N_t; t)^2 \tag{3.21}$$

Generalizing,

$$P_s(\rho_c, N_p, N_t; t) = P_s(\rho_c, 2, N_t; t)^{N_p - 1}. \tag{3.22}$$

It is now important to compare systems with different sizes N_t. We claim that the number of competing pairs $N_p - 1$ should scale linearly with size N_t, in order to maintain a constant fraction of quenching probes (ground state probes).

$$\left\{ \begin{array}{rcl} N'_t & = & \lambda N_t \\ N'_p - 1 & = & \lambda(N_p - 1) \end{array} \right. \tag{3.23}$$

The last relation implies $N'_p = 1 + \lambda(N_p - 1)$. Therefore, we assume that

$$P_s(\rho_c, N_p, N_t; t) \simeq P_s(\rho_c, N'_p, N'_t; t) = P_s(\rho_c, 1 + \lambda(N_p - 1), \lambda N_t; t) \tag{3.24}$$

As a particular case, for $\lambda = 4$ we have

$$P_s(\rho_c, 2, N_t; t) \simeq P_s(\rho_c, N'_p, N'_t; t) = P_s(\rho_c, 5, 4N_t; t) \tag{3.25}$$

We use the scaling relation to relate an arbitrary lipid patch size N_t to a reference patch size 256, therefore setting $\lambda N_t = 256$. If the fraction of probe lipids is $x = N_p/N_t$ then

$$\begin{aligned} P_s(\rho_c, N_p = xN_t, N_t; t) &\simeq P_s(\rho_c, 1 + \lambda x N_t - \lambda, \lambda N_t; t) \\ &= P_s(\rho_c, 1 + 256x - \lambda, 256; t) \qquad (3.26) \\ &= P_s(\rho_c, 2, 256; t)^{256x-\lambda} \qquad (3.27) \end{aligned}$$

Let us assume that N_t corresponds initially to a 100 nm diameter liposome containing 50000 lipids, and a single excited probe, one finds that $\lambda \simeq 256/50000 = 0.005$. Meanwhile, experimental probe fractions contain at least $x = 0.001$ probe. We therefore have in the exponent of (3.27) a term $256x$ of order 1 and a term λ much smaller. To be more general, λ is of the order of the ratio between the number of excited lipid molecules and total number of lipids, at a given time. For normal illumination intensities, this should be a small value.

We consequently neglect λ in (3.27) and derive a simpler scaling form

$$P_s(\rho_c, N_p = xN_t, N_t; t) \simeq P_s(\rho_c, 2, 256; t)^{256x} \tag{3.28}$$

This above equation, obtained by combining size scaling and independent pair assumptions, enable us to reduce any system with any concentration to a reference survival curve P_s.

When one now considers interleaflet association, one introduces another survival curve associated to the collision probability between probes belonging to two opposite leaflets $P_o(\rho_c, N_p = xN_t, N_t; t)$. The scaling form is simpler because one does not have to remove the excited probe from the list of quenchers. The extra λ factor in the exponent is not present.

$$P_o(\rho_c, N_p = xN_t, N_t; t) \simeq P_o(\rho_c, 1, 256; t)^{256x} \tag{3.29}$$

Allowing for both same and opposite leaflet formation is achieved by multiplying P_s and P_o. What is obtained is the total collision survival probability.

$$P_c[x](t) = P_o(\rho_c, 1, 256; t)^{256x} P_s(\rho_c, 2, 256; t)^{256x} \tag{3.30}$$

Sampling of the survival probability $P_s(\rho_c, 2, 256; t)$ is generated from an *a posteriori* ("rerun") analysis of trajectories of 256 lipids leaflets. A 150 ns trajectory (coarse-grained Martini time) was considered. Then, every possible pair (a total number of $256 \times 255/2$ of them) is picked-up for which the first passage time (collision time) is determined, provided it takes place during the available run time. An histogram of collision times is built, which provides the desired $P_s(\rho_c, 2, 256; t)$ curve. Considering all possible pairs belonging to opposite leaflets, one gets $P_o(\rho_c, 1, 256; t)$

Multiple passage times It is possible to deal with a non instantaneous excimer formation time by introducing a finite formation rate q. A simple implementation of the idea amounts to saying that excimer forms at a rate q so long as the two terminal subgroups relative distance is smaller than ρ_c. Mathematically, the survival of a given pair ij is

$$\frac{\mathrm{d}p_{ji}}{\mathrm{d}t}[r_{ij}(t)] = -q\chi(r_{ij}(t))p_{ij} \tag{3.31}$$

The survival probability p_{ij} depends on the relative distance $r_{ij}(t)$ associated to the initial positions and subsequent trajectory of the pair ij. χ can be as simple as 1 for $r_{ij} \leq \rho_c$ and 0 otherwise. p_{ij} can be integrated as

$$p_{ij}(t) = \exp\left[-\int_0^t \mathrm{d}\,t'\, q\chi(r_{ij}(t))\right] \tag{3.32}$$

and subsequently averaged over initial positions and trajectories, leading to

$$P_s(\rho_c, 2, 256; t) = \left\langle \exp\left[-\int_0^t \mathrm{d}\,t'\, q\chi(r_{ij}(t))\right]\right\rangle \tag{3.33}$$

The previous case is recovered as $q \to \infty$.

4 Algorithm

1. Run MD simulations, 256 lipids per leaflet, 5×10^6 steps (four times), corresponding to 150 ns (Coarse-Grained times).
2. Sample the survival probabilities $P_s(\rho_c = 0.5, 2, 256; t)$ and $P_o(\rho_c = 0.5, 1, 256; t)$ from the MD trajectories using a rerun procedure, and averaging over the 32640 possible pairs.

3. Integrate $J_M = \int \mathrm{d}t P_c e^{-t/\tau_M}/\tau_M$, with P_c given by eq. (3.30) (or similar) for a set of x values similar to the experimental results.

4. Fit $1/J_M(x)$ to published experimental data with τ_M as adjustable parameter.

5. Deduce the acceleration factor f, defined as $\tau_M(\text{exp})/\tau_M(\text{fit})$, with $\tau_M(\text{exp})$ obtained from lifetime measurements, and $\tau_M(\text{fit})$ in coarse-grained time units.

6. Get D_{CG} from a mean-squared displacement analysis, and infer the "true" $D = D_{CG}/f$ assuming homogeneous scaling of times.

Chapter 4

Submitted manuscript

Excimer formation of pyrene labeled lipids interpreted by means of coarse-grained molecular dynamics simulations

P. Ayoub, F. Thalmann

The excimer formation dynamics of pyrene-labeled molecules in lipid bilayers depends on molecular motion over distances of the order of 1-2 nm. From the concentration dependence of the excimer photoemission curve, it is possible to derive a value for the lipid self-diffusion coefficient. This technique has been intensively used in the past twenty years, leading to rather large numerical values for self-diffusion compared with other approaches based on fluorescent probes tracking. In most cases, the interpretation of the experimental data rely on models for diffusion limited 2d reaction rates, or comparison with 2d lattice random walks. Our approach uses realistic molecular dynamics trajectories to reinterpret these experiments. Based on a well established coarse-grained model for lipid MD simulations (Martini), we show how to relate simulation results to experimental data on excimer formation. Our procedure is quite general and is applicable to all diffusion-limited kinetic processes. Key to our approach is the determination of the acceleration factor of lipid coarse-grained numerical models compared to reality. We find a significant reduction of the diffusion coefficient values, in particular when interleaflet association is taken into account. Our work does not point to deviation from a diffusion-limited mechanism but indicates that the excimer formation across bilayer leaflets could be hindered.

I. INTRODUCTION

Most lipid self-diffusion determination methods rely on long range diffusion (Fluorescence Recovery After Photobleaching FRAP, Fluorescence Correlation Spectroscopy FCS, Pulse Field Gradient NMR). On the other edge, inelastic neutron scattering probes the lipid dynamics on very short time and length scales. The pyrene excimer formation approach, initiated long ago [1], is unique as far its characteristic time (100 ns) and length (1-2 nm) scales are concerned. It opens a window onto the nanometric scale in lipid membrane organization, currently subject to many supposed phenomena (rafts, static or dynamic nanodomains). How much is lipid diffusion dynamics on these scale regular or anomalous is a topic of great interest.

So far, numerical simulations are promising investigation tools to answer these questions. On the other hand, pyrene excimer formation experiments have been mostly interpreted in terms of 2d lattice random walks properties, which cannot describe faithfully the correlated motion of lipid molecules at this scale. There is little doubt that an analysis based on realistic molecular motion should outperform any approach based on point-like particles jumping over fixed discrete lattices.

In this article, we attempt to refine the past analysis of pyrene-lipid analogues diffusion by using coarse-grained (CG) molecular dynamics (MD) based on the celebrated Martini force-field [2]. Introducing a novel statistical approach that relates molecular dynamics trajectories to diffusion limited association kinetics among lipid chain subgroups, we obtain a numerical analogue to the excimer/monomer emission ratio as a function of the probe concentration. This allows us to obtain the experimental diffusion coefficient by matching the short time excimer formation rate to the long time diffusion displacement.

We find diffusion coefficients values significantly smaller than previously admitted. This provides an important clue as far as reducing the spread among all experimental values currently found in the literature.

Our paper is organized as follows. Section II introduces the principle of excimer formation dynamics. Section III explains how one can relate MD trajectories to experimentally relevant data. In Section IV we analyze data published by Vauhkonen et al., and Sassaroli et al. [3, 4]. Results are discussed in Section V followed by Conclusion.

II. EXCIMER FORMATION DYNAMICS

Excimers are complexes formed by two identical molecules, one being in an excited state, the other in its ground state. The fluorescence emission spectrum of the isolated molecules, commonly referred as monomers, markedly differs from the emission spectrum of the excimers, or dimers. This makes it possible to measure optically the fraction of fluorescent probes ending up into an excited dimer (excimer) state.

Excimer formation results from a diffusion limited mechanism of bimolecular reaction kinetics, and the formation rate is related to the self-diffusion coefficient of the fluorescent probes [5]. The probability that an excited monomer ends up forming an excimer is the outcome of a competitive process involving bimolecular collision rate on the one hand, and spontaneous de-excitation rate (inverse fluorescence lifetime) on the other hand.

Pyrene molecules form very stable excited dimer states. They can be incorporated, as pyrenyl groups, into phospholipid analogues and inserted in lipid membranes. These fluorophores are characterized by a longer than usual lifetime, ranging from 100 to 200 ns. The pyrene excimer formation is therefore reporting on the dynamical moves of lipid molecules on this time scale, corresponding to spatial displacements of the order of 1 to 2 nm in the bilayer. In this respect, this dynamics probes local molecular motions at a nanometric scale. The use of pyrene derivatives for the purpose of studying lipid membrane dynamics was reviewed by Somerharju [6]. A larger class of diffusion-limited excitation or deexcitation processes in membranes is covered in a review by Melo and Martins [7].

The determination of lipid diffusion coefficients D using pyrene derivatives is quite indirect. Fluorimetric techniques provides a “titration curve” of the monomer and excimer normalized emission intensities $J_M(x), J_E(x)$ as functions of the pyrene molar fraction x and monomer fluorescence lifetime τ_M. Statistical models of molecular diffusion must be used to relate the diffusion constant to the excimer formation rate. So far, approaches based on cubic and hexagonal lattice random walks, and Smoluchovsky-Naqvi theoretical models have been used to interpret the experimental data [1, 3, 4, 8–11]. The approaches based on lattice random walks tend to give larger diffusion coefficient values than the ones obtained, *e.g.*, by tracking fluorescent lipid probes over larger scales, such as in FRAP or FCS experiments (see Discussion).

Current theoretical approaches are limited to ideal random walks or Wiener diffusion processes and they also involves approximations [12–15]. Anomalous Brownian displacements of the pyrene groups, membrane heterogeneous nanodomains could both invalidate the current numerical estimates of lipid diffusion coefficients. Conversely, a robust microscopic description of pyrenyl derivatives excimer formation would certainly help to improve the description of short range dynamical properties of lipid membranes.

In this work, we propose to use a well-known coarse-grained model for lipid bilayers, the Martini force field, and to analyze the excimer fluorimetric data based on realistic molecular dynamics (MD) trajectories.

III. THEORY

A. First-passage reaction kinetics

Diffusion-limited bimolecular reactions represent a class of physical or chemical kinetics in which reagents react at first encounter with a yield equal to, or close to unity. This limit means that there is no activation energy barrier, nor orientation barrier opposing the formation of the product [16].

The reaction rate of a diffusion limited reaction depends exclusively on the diffusion dynamics of the two species and on the geometrical shape of the reaction region. The most natural treatment, initiated by Smoluchovsky, considers two spheres following ideal Brownian trajectories and reacting as soon as their relative distance drops below a critical value: the *capture radius* ρ_c. Naqvi derived a Smoluchowsky rate in the two dimensional case [12]. Both approaches predict a time-dependent reaction rate and are restricted to ordinary (Wiener) diffusion processes. They are mean-field in nature as relative spatial correlations of the reactants are neglected [14].

The experimental results reported in [4] were obtained with a pyrenyl group attached to a 10 atoms long alkyl chain. This group is mobile with respect to its parent molecule center of mass, and its Brownian displacement is affected by the intramolecular degrees of freedom on short time-scales. Its motion cannot be represented accurately by a Wiener process, as the associated *mean-squared displacement* is not just a linear function of time and includes intramolecular Rouse dynamics. The consequences of such deviations with respect to the simplest Brownian model description, on the collisional dynamics properties of the pyrenyl groups must be assessed.

The *Martini* force-field treats each phospholipid molecule as an assembly of 10 to 14 beads, according to a 4 atoms to 1 bead correspondence. This level of coarse-graining preserves to a certain extent the intramolecular conformational degrees of freedom of the original atomistic model. With access to submolecular details, one can attempt to improve the collisional dynamics description compared with lattice or continuous models reducing lipids to point-like objects. This is the *rationale* behind our treatment of pyrene derivative excimer formation dynamics.

On the other hand, CG models are characterized by a nonphysical accelerated time scale, so that they cannot predict transport properties without a reference element (experiment or all-atoms simulation). The reference element, in our case, is the experimental monomer/excimer fluorescence ratio.

B. Neutrality of fluorescent lipid probes substitution

Fluorescence is an extremely useful and versatile technique. Its use in the field of membrane studies includes imaging, life-time, anisotropy depolarization and resonant energy transfer studies. In most cases, the amount of necessary fluorophores is small, as fluorescence detection can be very sensitive. A common assumption of all these approaches is that the fluorescent labeled molecules, which often are made as similar to phospholipid molecules as possible, modifies only marginally the structure and the dynamics of the host membrane. For instance, the diffusion coefficient obtained in a FRAP experiment, is the one associated with the fluorescent probes. The identity between probe and normal lipid motions remains an assumption.

The pyrene excimer formation method requires relatively high amounts of pyrenyl derivatives, up to 10% molar ratio. It is assumed that the motion of the pyrenyl-grafted lipids is identical to the regular lipid compounds, and that the bilayer structure is not modified significantly. We therefore adopt this view and treat pyrene-labeled lipids as if they were ordinary phospholipid molecules. This is both a simplifying assumption and a limit of the present approach.

We do not have at our disposal a coarse-grained model of pyrene-labeled lipid molecule. The polyaromatic pyrenyl group is clearly bulky compared with standard alkyl chains, and the effective van-der-Waals interaction parameters should be increased to reflect its higher polarizability. It is difficult to estimate these parameters at coarse-grained level, and guesswork is unlikely to provide an acceptable set of interactions. Another difficulty arises when it comes to model the interaction between a photoexcited pyrene group and one in its ground state. It is believed that attractive interactions arise from resonant energy states, leading to stronger and longer range (r^{-3} with separation r) attractive forces, eventually leading to the complexed dimer state [5, 17]. In a realistic model, those modified interactions should be estimated and taken into account.

Even if a CG model of pyrenyl derivatives existed, simulating a diluted mixture of probes and repeated sequences of excitation → diffusion → excimer formation would require lengthy and multiple runs, to obtain just a rough statistics of the events. Our opinion is that such an intense computational effort would only make sense if a trusted and robust

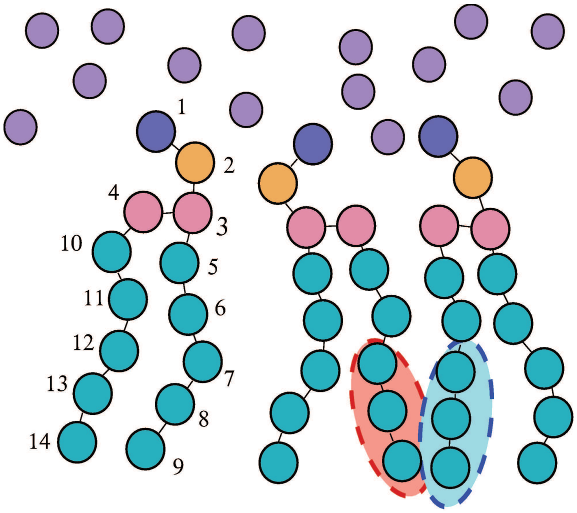

FIG. 1. Example of coarse-grained lipid molecule (DOPC) with bead labels, and two terminal subgroups during a “collision event”.

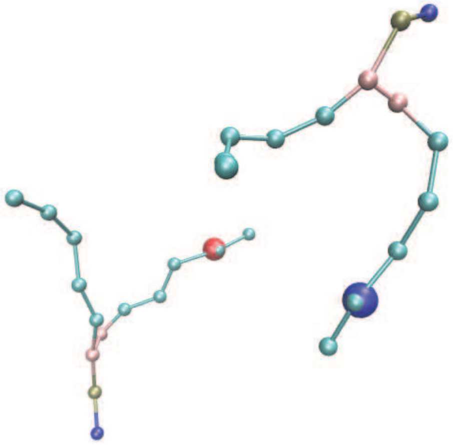

FIG. 2. Detail of two DOPC molecules, each in one leaflet, with terminal subgroups superimposed on top of them.

CG model of pyrenyl compounds was first established, including the modified interactions of the photoexcited pyrene group.

We remain faithful to the implicit assumption that fluorescent probes behave the same as the major lipid components. Ordinary MD simulation runs are performed and trajectories acquired. The equilibrated trajectories are then analyzed *a posteriori*, as if a few of the lipid beads were actually pyrenyl moieties. Our strategy is therefore to *rerun* the trajectory (without recomputing the forces) with a relabeling of some beads *a posteriori*. In practice, one can reduce the determination of the pyrene excimer formation assays to regular dynamical time dependent correlation functions of the ordinary lipid molecules. The next subsection introduces such dynamical quantities.

C. Survival probabilities

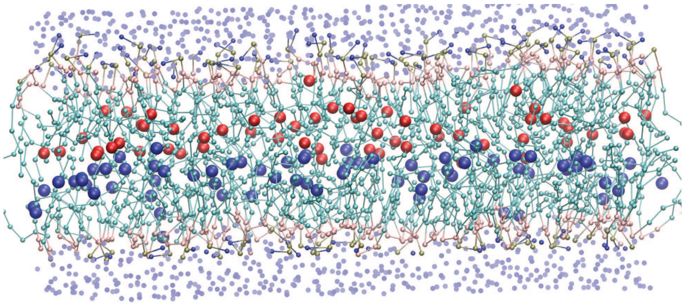

FIG. 3. Side view of a DOPC bilayer, with superimposed terminal subgroups from the upper and lower leaflets (using two different colors depending on the leaflet to which the molecule belongs).

A CG model of DOPC is represented on Fig. 1 and Fig. 2. We propose to assign to the pyrene group a set of three beads numbered from 12 to 14, hereafter referred as the *the fluorescent group*, or *terminal subgroup* (TS). A similar procedure defines the POPC terminal subgroup (not shown). We assume that the excimer association takes place as soon as the relative distance between two terminal subgroups becomes less than a critical radius, which we refer as the *capture radius* ρ_c, by reference to the Smoluchowsky description of first passage reaction kinetics. Fig. 3 shows a bilayer snapshot with its associated terminal subgroups.

Let us now consider a simulation box containing a total of N_t lipids, among which N_p will be considered *a posteriori* to be fluorescently labeled, in each leaflet. We denote L the side of a squared simulation box in the x, y directions, with periodic boundary conditions (pbc). We introduce the survival probability $P_s(\rho_c, N_p, N_t, L; t)$ as the probability that no excited fluorescent group have come into contact with any of the $N_p - 1$ remaining groups *in the same leaflet* during a time interval t.

P_s is the outcome of an averaging procedure over both initial conditions (the choice of the fluorescent groups and their actual spatial distribution) and subsequent trajectories (the Brownian displacements of these fluorescent groups). The negative time derivative $-\mathrm{d}P_s/\mathrm{d}t$ represents the probability of "capture" per unit of time, or first passage time distribution. By *capture* is meant that one of fluorescent group in its ground state penetrates into a sphere of radius ρ_c centered around the excited group for the first time during the interval $[t, t + \mathrm{d}t]$.

We define in a very similar way $P_o(\rho_c, N_p, N_t, L; t)$ the probability that any pair of fluorescent groups taken from randomly selected molecules *in two opposite leaflets*, have not come closer than a distance ρ_c during a time t. The collision dynamics controlling the formation of excimers is order of magnitude faster than the phospholipid flip-flop reversal times so that it makes sense to distinguish between the two subpopulations of lipids, and P_o effectively controls the influence of interleaflet monomer quenching.

The survival probabilities P_s, P_o can be efficiently sampled from regular MD trajectories. These dynamical quantities are well defined and related to the molecular displacements properties of the corresponding groups of beads. As we deal with realistic trajectories, we can address situations with transient dynamics, or non Gaussian self-intermediate scattering functions, and possibly improve upon most basic models of molecular diffusion. It remains, however, to relate these probabilities to the excimer/monomer fluorescence ratios which are experimentally obtained.

D. Size-scaling and independent pairs assumptions

Let us consider a lipid bilayer containing a total of N_t lipids in its upper leaflet, including a number N_p of fluorescent probes. For simplicity, we assume that both leaflets share the same composition, making the bilayer symmetric. The size of the bilayer is supposed to be unaltered by the presence of the probes, so that the size L of the system is directly related to the number of lipids N_t by means of the area per lipid a_0 ($N_t = L^2 a_0$).

Under normal illumination conditions, the fraction of time spent in the excited state is tiny, and at any given time the chances of finding two excited monomers in the same portion of membrane is statistically very low. One can therefore consider that one fluorophore at most is excited at a time, and that $N_p - 1$ monomers are available to combine as an excimer.

If the motions of the pyrene monomers are decorrelated, the survival probability $P_s(\rho_c, N_p, N_t; t)$ can be reduced to $P_s(\rho_c, 2, N_t; t)^{N_p - 1}$. This is because $N_p - 1$ different pairs compete independently, and that the effective collision time is *the minimum* of $N_p - 1$ independent first passage events. Note that the interaction between pyrene monomers is only possible when at least two of them are situated at the immediate vicinity of an excited probe. The outcome of such a situation involving a compact triplet of probes is difficult to ascertain, either enhancing, or disfavoring the formation of a stable excimer. We therefore refer to *independent pairs assumption* the possibility of factorizing the survival probability when the concentration x of probes is low enough.

When interleaflet interaction is allowed, the survival probability in the independent pairs assumption framework reads:

$$P_{\rm c}(t) = P_s(\rho_c, 2, N_t, L; t)^{N_p - 1} P_o(\rho_c, 1, N_t, L; t)^{N_p}. \tag{1}$$

We now address the issue of the sample size dependence. It sounds quite natural to assume that the survival probability depends on size (L or N_t) only throughout the intensive ratio $x = N_p/N_t$. If this holds, the survival probability for collisions between opposite leaflets, for instance, should obey the following scaling relation:

$$\begin{aligned} P_o(\rho_c, N_p, N_t; t) &= P_o(\rho_c, \lambda^2 N_p, \lambda^2 N_t; t) \\ &= P_o(\rho_c, \lambda^2 x N_t, \lambda^2 N_t; t). \end{aligned} \tag{2}$$

In the case of collisions between groups in the same leaflet, we observe that the excited pyrene group, *i.e.* the target, must be removed from the list of moving groups participating to the excimer quenching statistics. This has consequences when N_p is small, and the suggested size scaling form for the survival probability within a given leaflet must be slightly modified to account for the "missing" pyrene group.

$$\begin{aligned} P_s(\rho_c, N_p, N_t; t) &= P_s(\rho_c, 1 + \lambda^2 (N_p - 1), \lambda^2 N_t; t) \\ &= P_s(\rho_c, 1 + \lambda^2 (x N_t - 1), \lambda^2 N_t; t). \end{aligned} \tag{3}$$

We refer to these assumptions as the *size scaling* assumptions. There are reasons to believe, though, that the size scaling assumptions do not hold uniformly. As a matter of fact, collision time distributions do depend explicitly on sample size in 2d Brownian reaction-diffusion models. For instance, the probability of finding a target in a domain of linear size L involves $\ln(L)$ corrections with respect to the naive mean-field result. We claim however that these corrections are unlikely to change very much the short time dependence of the survival probability. As far as pyrene excimer formation is concerned, the contribution of long trajectories wandering on large distances $\sim L$ away from the capture radius are unlikely to contribute to the short time behavior of the survival probability, which turns out to dominate the excimer formation probability. However, they would give rise to significant contributions at longer times.

Combining *independent pairs* and *size scaling* assumptions, we can reduce the collision survival probability of an excited pyrenyl group to the survival probability of a single pair sitting in a bilayer of arbitrary size λL:

$$\begin{aligned} P_{\rm c}(t) &= P_s(\rho_c, 2, \lambda^2 N_t; t)^{\lambda^2 x N_t - \lambda^2} \\ &\quad \times P_o(\rho_c, 1, \lambda^2 N_t; t)^{\lambda^2 x N_t}, \\ &\simeq P_s(\rho_c, 2, \lambda^2 N_t; t)^{\lambda^2 x N_t} \\ &\quad \times P_o(\rho_c, 1, \lambda^2 N_t; t)^{\lambda^2 x N_t}. \end{aligned} \tag{4}$$

The resulting survival function $P_{\rm c}(t)$ is the global collision survival probability.

What remains to be done is to use a scaling factor λ corresponding to a tractable simulation scheme. In the present work, we use $\lambda^2 N_t = 256$ to sample P_s and P_o. In addition, we notice that in experimentally relevant situations, $\lambda^2 N_t$ is significantly smaller than the actual number of lipids in the physical system of interest (*e.g.* a liposome), and the λ^2 term in the exponent of P_s can be safely neglected in eq. (4).

E. From survival probabilities to excimer fluorescence intensity

The excimer formation probability is readily obtained from $P_{\rm c}(t)$. A monomer excited at $t = 0$ forms an excimer during the time interval $[t, t + {\rm d}t]$ with probability

$$-\frac{{\rm d}P_{\rm c}}{{\rm d}t} \exp\left(-\frac{t}{\tau_M}\right), \tag{5}$$

which is the probability of colliding with a ground state monomer while still in the excited state, with τ_M standing for the monomer fluorescence lifetime in the ultra-dilute case ($x \to 0$). The excimer formation probability J_E is therefore

$$\begin{aligned} J_E &= \int_0^\infty -\frac{\mathrm{d}P_\mathrm{c}}{\mathrm{d}t} \exp\left(-\frac{t}{\tau_M}\right) \mathrm{d}t \\ &= 1 - \int_0^\infty P_\mathrm{c}(t) \exp\left(-\frac{t}{\tau_M}\right) \frac{\mathrm{d}t}{\tau_M}. \end{aligned} \tag{6}$$

$1 - J_E$ is the Laplace transform of the survival probability. Naturally, the probability of returning to ground state from the excited monomer state is $J_M = 1 - J_E$. The probe ratio x dependence of the monomer/excimer fluorescence intensity curves $J_M(x), J_E(x)$ comes from the x dependence of the survival probability $P_\mathrm{c}(t)$, such as expressed in eq. (4). Alternatively, the integrand

$$\frac{1}{\tau_M} P_\mathrm{c}(t) \exp\left(-\frac{t}{\tau_M}\right) \tag{7}$$

corresponds to the time-resolved emission intensity of the monomer probe.

F. Intermolecular formation rates

In principle, the survival probability P_c must be extracted from the microscopic model for any arbitrary value of x, and the normalized emission intensities J_E and J_M become dependent on the molecular ratio x. The variation of the fluorescence intensities therefore reports on the concentration of monomeric (or dimeric) probes, and behaves as in a standard titration experiment, except that for practical reasons x cannot be changed during the course of the experiment.

One peculiar value $x = x^\ddagger$ makes the excimer formation probability equal to 1/2:

$$J_M(x^\ddagger) = J_E(x^\ddagger) = 1/2. \tag{8}$$

This value turns out to plays a key role in the interpretation of the experimental titration curves $J_E(x), J_M(x)$ by Vauhkonen et al. [3] .

Let us assume first that the survival probability $P_\mathrm{c}(t)$ is exponentially decaying as $\exp(-t/\tau_c(x))$. In this case, $x^\ddagger$ is nothing but the concentration for which the collision time $\tau_c(x^\ddagger)$ equals the monomer spontaneous decay time τ_M,

$$\tau_c(x^\ddagger) = \tau_M. \tag{9}$$

It is common to treat the excimer formation dynamics as an ordinary *bimolecular kinetic process* $M + M^\star \to (MM)^\star$ with formation rate $K(x)$, and to take the reverse dissociation as negligible. As the monomer is in excess, the situation corresponds to an ideal pseudo-first order reaction kinetics, consistent with an exponential decay of the excited monomer population. The decrease rate of the excited probes reads $\mathrm{d}[M^\star] = -(K(x) + \tau_M^{-1})[M^\star]\mathrm{d}t$, leading to the monomer emission intensity

$$\frac{1}{J_M(x)} = 1 + \tau_M K(x). \tag{10}$$

For a pure mean-field, constant rate bimolecular mechanism, $K(x)$ is expected to depend linearly on x, enabling us to rewrite the previous expression as

$$\frac{1}{J_M(x)} = 1 + \frac{x}{x^\ddagger}. \tag{11}$$

The corresponding normalized emission intensity curves then reduce to simple rational functions.

$$J_M(x) = \frac{x^\ddagger}{x + x^\ddagger} \; ; \; J_E(x) = \frac{x}{x + x^\ddagger}. \tag{12}$$

It can be shown that pseudo-first order excimer formation kinetics and exponential survival behavior are two equivalent assumptions. Conversely, any deviation from linear behavior of the inverse emission intensity $1/J_M(x)$ points to a *non exponential survival behavior* of the excited monomeric probes, or a *non constant rate mechanism.* Example of diffusion limited models leading to such time dependent rates are discussed, for instance, in [14]. Our analysis does not make any assumption regarding the kinetic rate coefficients, and the survival probability is sampled from MD trajectories.

G. Multiple passage times

The lack of detailed evidence for the molecular excimer formation mechanism makes it necessary to adopt a phenomenological and probabilistic view on the outcome of the collisional dynamics. Even though the excimer formation is expected to be diffusion dominated, there is nevertheless a chance that collisions does not lead to excimer state with perfect yield.

It is possible to introduce a distance dependent excimer formation rate, such as *e.g.* the distance dependent energy transfer rate of a Förster resonant pair. In this case, the excimer formation probability depends on the integrated time spent by the pair at close distance.

Denoting by $r(t)$ the relative distance of a single pair, the survival probability of an excited monomer associated with a trajectory $\{r(t)\}$ reads

$$\exp\left(-q\int_0^t \chi\left[\frac{r(t')}{\rho_c}\right]\,\mathrm{d}t'\right), \tag{13}$$

with q denoting a tunable excimer formation rate, ρ_c a characteristic capture radius, and χ a positive function decaying from 1 to 0.

The generalization of the survival probability is obtained by averaging over the initial positions and subsequent trajectories $r(t)$:

$$P_s(q,\rho_c,2,\lambda^2 N_t;t) = \left\langle \exp\left(-q\int_0^t \chi\left[\frac{r(t')}{\rho_c}\right]\,\mathrm{d}t'\right)\right\rangle_{\{r(t)\}}, \tag{14}$$

with the same notation as in eq. (3). One notices that the first passage survival probability can be obtained as a limit case of a step function $\chi[v] = 1$ for $v \leq 1$ and 0 otherwise, combined with $q \to \infty$. The survival probability for an arbitrary x concentration follows from the size-scaling relation.

Functions P_s, P_o defined as in eq. (14) can be conveniently sampled from molecular dynamics trajectories. This approach to multiple passage dynamics is simple to implement, and contains the first passage capture process as a limit case.

Low values of q correspond to low excimer formation rate. A general feature, as we found, is that the resulting $P_s(t)$ becomes more and more exponential as q decreases, with an average survival time increasing as expected. The resulting inverse probability $1/J_E$ is therefore expected to become more and more linear with x as q decreases, giving us a chance of estimating q. This turned out not to be the case in practice.

H. Estimating the capture radius

There is arbitrariness when it comes to giving a numerical value to the reaction, or capture radius ρ_c. In the Martini model, the van der Waals radii of the coarse-grained beads are set to 0.47 nm. Closer approach between beads can only be associated to enthalpic repulsive interactions, which are not supposed to intervene in a diffusion-limited association process.

On the other hand, in order to represent as well as possible the motion of pyrene groups, we bunched together the last beads of each hydrophobic chain groups. The generalized coordinates representing the "pyrene" center of masses, are themselves not materialized as beads and their mutual interaction potential is softer, to some extent, than the one of the original beads. Fig. 4 represents the 2d pair distribution function of group belonging to a given leaflet.

It can be seen that steric hindrance between pyrene center of masses becomes significant for values of r smaller than 0.5 nm. We therefore take $\rho_c = 0.5$ nm as our capture radius value.

I. Real systems vs coarse-grained dynamics

A first question arises, as to which extent coarse-grained dynamics is faithful to the trajectories of the real phospholipid molecules that it is intended to model. It is established that most large scale transport properties such as self-diffusion, transverse viscosity, etc are *in fine* controlled by *cis-trans* isomerization dynamics of the lipid alkyl

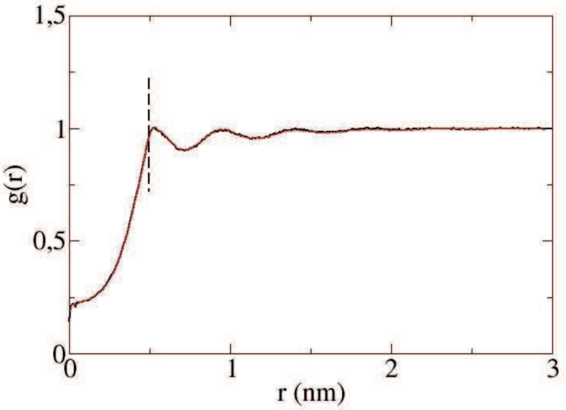

FIG. 4. Pair distribution of terminal subgroups. The vertical dashed line indicates the horizontal separation $r = 0.5$.

chains [18]. These degrees of freedom are obviously missing at the level of the Martini coarse-grained description, and substituted for by an effective "Kremer-Grest" dynamics of beads and springs polymer chains subject to van-der-Waals interaction. This accounts for the largest fraction of the difference seen between the coarse-grained and atomistic molecular kinetics. Martini simulation are sped up by an acceleration factor f commonly taken of the order of 4. As a by-product, CG molecular dynamics cannot, alone, provides quantitative estimates of the lipid transport coefficients.

The *cis-trans* chain isomerization moves are temperature dependent, activated processes. As a result, the membrane fluidity strongly depends on temperature, showing Arrhenius dependence in the absence of phase transition. The Martini activation energy is lower than the experimental one. The factor f is therefore likely to depend significantly on temperature. On the other hand, it is not necessary to match precisely the temperature of the CG simulation with the experimental system that one aims at reproducing, provided one restrict ourselves to the same structural phase. We may therefore rely on a kind of *time-temperature* superposition approximation to adjust to experimental data. Note that irrespective to changes occurring with lipid dynamics, the monomer fluorescence life-time is also a decreasing function of temperature, and must be provided as an external experimental input.

We assume in our approach that the acceleration factor f applies in a uniform way, from short chain reorganization time scales up to long range hydrodynamic limit. In other words, if one can determine f based on the intermediate time regime associated with fluorescence life-time and collision induced excimer formation, one should be able to give a quantitative prediction of the physical lipid diffusion constant D as $D = D_{\mathrm{MD}}/f$, where D_{MD} represents the molecular dynamics diffusion coefficient obtained from the mean-squared displacement. This can be assimilated to a *matching procedure*.

Another difference between real molecules and CG models lies into the repartition of masses within lipids. The Martini model ascribes an identical mass (72 amu) to all beads, while in reality the phosphate headgroup concentrates more mass than the alkyl chains for comparable steric volumes. As dynamical properties depend on masses (unlike thermodynamics) this could cause differences between real and simulated trajectories. In the present work, we assume that such differences can be disregarded.

IV. NUMERICAL RESULTS AND COMPARISON WITH EXPERIMENTS

A. Diffusion properties of the terminal subgroups, and survival probabilities

Survival probabilities were sampled by simulating patches of 512 lipids, respectively POPC at 293K and DOPC at 283K, using 4 trajectories of 150 ns (Martini time). Frames were recorded every 6 ps for the collision statistics, and averages over all the possible pairs of molecules were taken in order to sample $P_s(t, 2, 256)$ and $P_o(t, 1, 256)$. Trajectories were generated with Gromacs-4.6 [19] using a NVT Nose-Hoover thermostat scheme, and the Martini force-field *v2* for the lipids.

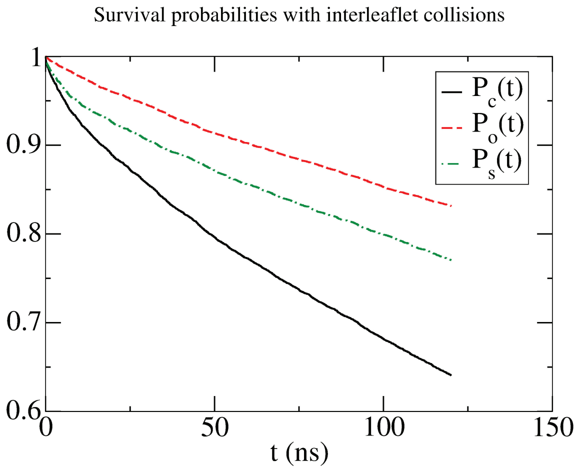

FIG. 5. Survival probabilities restricted to same leaflet, opposite leaflet and product of both. Trajectories are from DOPC at 283 K, with a capture radius $\rho_c = 0.5$ nm and frames taken every 6 ps of simulation time.

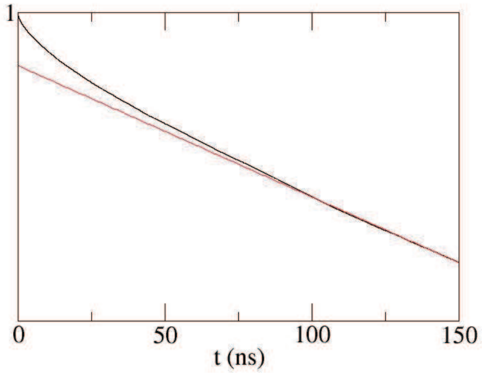

FIG. 6. Survival probability $P_c(t)$ when collisions are unrestricted (DOPC at 283 K). The vertical axis is logarithmic, and a straight line representing the asymptotic behavior $0.926 \exp(-0.00196t)$ (t in ns) is also shown. The straight line goes from 0.926 (t=0) to 0.687 (t=150 ns), and the distance to upper curve represents a deviation from pure exponential behavior of P_c. The curve represented above corresponds to a concentration $x = 1/256$, and the non-exponential behavior at short times is reinforced as the concentration x increases.

Fig. 5 shows the survival probability when collisions are restricted to molecules belonging to the same leaflet $P_s(2, 256, t)$, to opposite leaflets $P_o(1, 256, t)$, and then the product $P_c = P_o P_s$. The latter is expected to rule unrestricted excimer formation. Introducing collisions between opposite leaflets increases significantly the survival decay rate.

Fig. 6 shows the collisional survival probability $P_c(2, 256, t)$ of the chain subgroups, that is central to our reaction kinetics modeling, on a semi-logarithmic plot. As discussed in the previous section, such non exponential behavior can be related to deviation from the Stern-Volmer linear plot of the titration curves.

A direct test of the size-scaling approximation is provided in Fig. 7, when survival probabilities obtained from a single pair of monomers embedded respectively in leaflets of 256 and 1024 lipids are displayed. The scaled survival curve $P_s(2, 1024, t)^4$ matches $P_s(2, 256, t)$ at short times, while departing from it at longer times. This expected behavior originates from trajectories showing a large separation between reacting pairs, allowed in the large system but forbidden (due to periodic boundary conditions) in the small system. It is also a signature of the size dependence

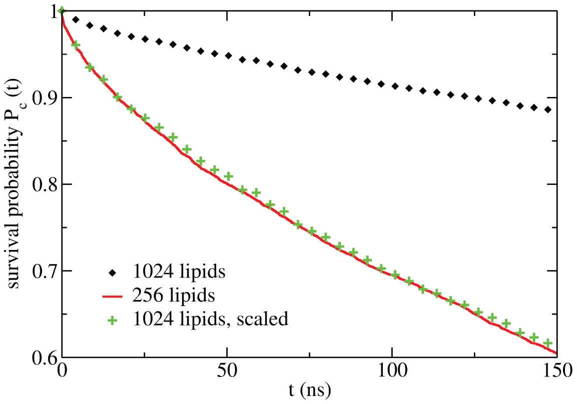

FIG. 7. Size-scaling approximation for DOPC molecules, using 512 and 2048 lipids in the simulations.

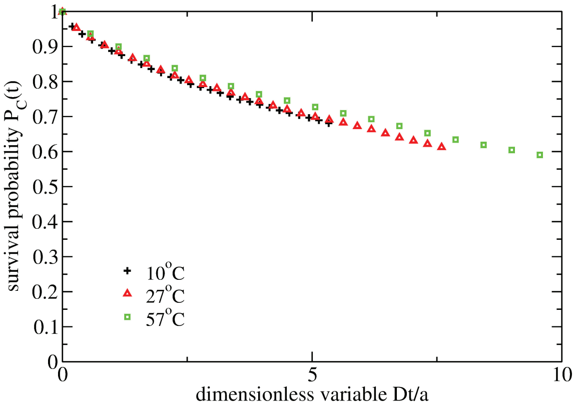

FIG. 8. Time temperature superposition of the survival probability for DOPC bilayers. Simulated temperatures are 283, 300 and 330K.

of Brownian diffusion limited reaction dynamics in two-dimensional systems. Clearly, departure from the size scaling assumptions is visible on this curve, at large times. However, the most relevant region, as far as excimer formation is concerned, is the short time regime, and this is especially true at large probe concentrations x. Therefore, we consider that the size-scaling assumption is valid in our case.

Fig. 8 shows that survival probabilities obtained from trajectories at different temperatures almost superimpose, once a dimensionless time variable $u = Dt/a_0$ is used on the horizontal axis.

B. Experimental titration curves

The experimental data on monomer to excimer emission ratio are taken from Fig. 3 in reference [3] (read from the graph) and displayed in Table I. The experimental values of the monomer fluorescence lifetime, which depends on temperature, are taken from Table 1 in reference [4]. The lifetimes of the isolated monomers are estimated from Fig. 5 in [3] to be respectively 140 ns for POPC at 20°C and 160 ns for DOPC at 10°C. It must be stressed that the final results are very much dependent on the actual τ_M values.

C. Fit of the excimer formation dynamics

	DOPC			POPC	
x	$1/J_M(x)$	$J_M(x)$	x	$1/J_M(x)$	$J_M(x)$
0.003	1.02	0.98	0.003	1.03	0.97
0.012	1.09	0.92	0.012	1.14	0.88
0.034	1.31	0.76	0.033	1.52	0.66
0.055	1.58	0.63	0.056	1.93	0.52
0.102	2.45	0.41	0.102	3.25	0.31

TABLE I. Monomer fraction $J_M(x)$ *vs* probe concentration x

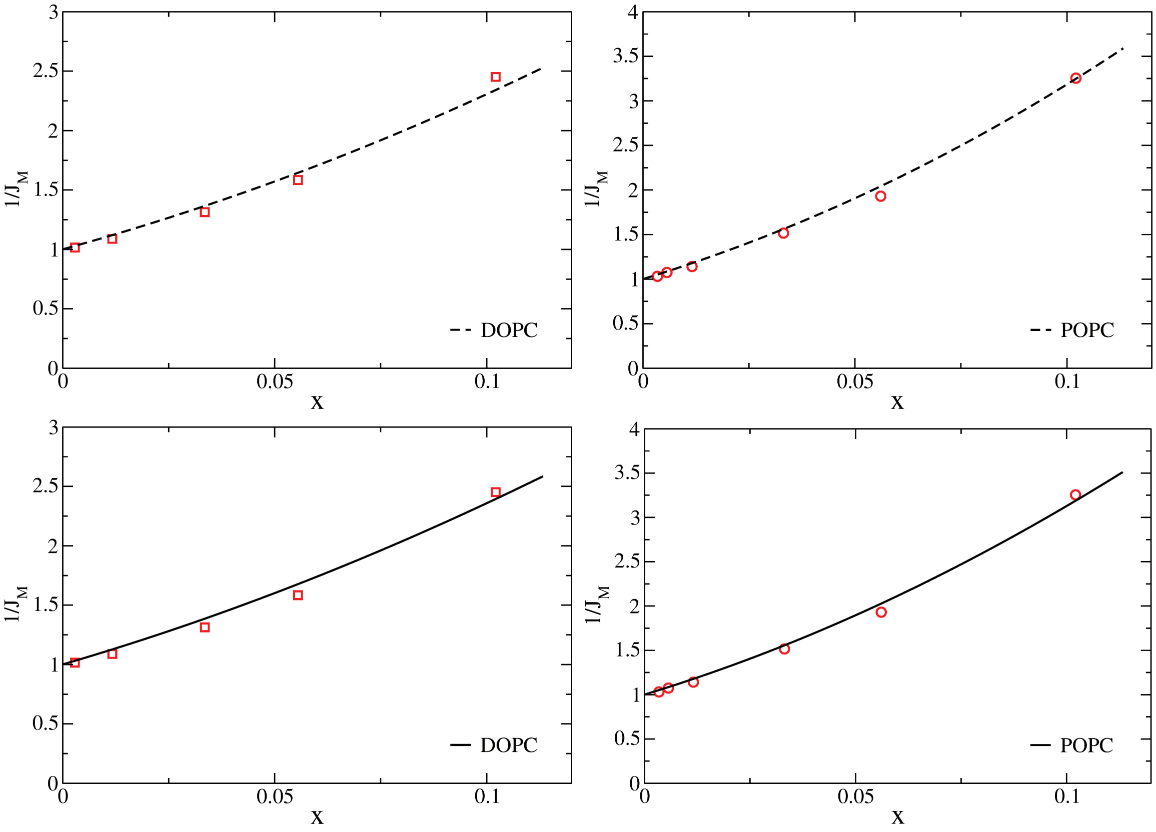

FIG. 9. *Top left:* fit of $1/J_M(x)$ in the DOPC case when association is restricted to molecules within a single leaflet. *Top right:* fit of $1/J_M(x)$ in the POPC case when association is restricted to molecules within a single leaflet. *Bottom left:* fit of $1/J_M(x)$ in the DOPC case when association originates from both leaflets. *Bottom right:* fit of $1/J_M(x)$ in the POPC case when association originates from both leaflets.

Fig. 9(*top left*) shows the agreement between the experimental values and the numerical prediction extracted from the survival probability of Fig. 6. The best agreement is obtained with "numerical" fluorescence lifetime $\tau_{M,CG}$ equals to 10.7 ns. The ratio between the experimental and the numerical lifetimes determines the acceleration factor $f = \tau_M/\tau_{M,CG} = 15$, given that $\tau_M = 160$ ns. The coarse-grained diffusion constant D_{CG} is assumed to scale as fD, with f the acceleration factor and D the real time diffusion constant. This approach predicts a value $D = 1.6$ μm.s^{-1} for DOPC molecules in a bilayer at 10°C, if no interleaflet association are allowed.

When adjustment is made with POPC trajectories at 20 K, as shown in Fig. 9(*top right*), the best fit is obtained with a numerical lifetime $\tau_{M,CG}$ equal to 15.6 ns. The acceleration factor is now $f = 9$ and the associated diffusion constant found for POPC at 20°C is $D = 4.0$ μm.s^{-1}.

Fig. 9(*bottom left*) shows the best agreement between the experimental and numerical curves, when the survival probability $P_c(t) = P_s(t) \times P_o(t)$ corresponding to unrestricted excimer formation is used. As the decay is now faster than in the previous case, a larger acceleration factor must be used to match the MD trajectories to the observed excimer formation rate. We obtain for DOPC at 10°C a factor $\alpha = 26$, leading to a diffusion constant $D = 1.0$ μm.s^{-1}. A similar adjustment to the experimental data leads, for a POPC bilayer at 20°C, to an acceleration factor $f = 20$ and $D = 1.8$ μm.s^{-1}, shown in Fig. 9(*bottom right*).

Lipid	Original D	MD D	MD D'
POPC (293 K)	11	1.8	4.0
DOPC (283 K)	6	1.0	1.6

TABLE II. Comparison of diffusion constants, obtained with the milling crowd analysis of [3] (column 2) and with the current approach, assuming reaction at first contact and allowing for interleaflet association (column 3) or excluding interleaflet association (column 4).

V. DISCUSSION

We first observe that our procedure reproduce to some extend the upward curvature seen on the $1/J_M(x)$ plots, even though a larger curvature would be required to optimally fit the data.

In Table II, we compare our new values to those originally published by Vauhkonen et al. (Table 1 of ref. [3]). Strictly speaking, the modeling of Vauhkonen et al excludes interleaflet excimer formation, and their values should be compared with our column 4. We find a significant reduction of the diffusion constant compared with their analysis.

Our diffusion constant in the case of allowed interleaflet formation is even smaller. On the one hand, if one trusts the coarse-grained MD trajectories, there is no reason to discard interleaflet association which occurs at a non negligible rate. In other words, $P_c(t)$ differs enough from $P_s(t)$ to alter significantly the final results. The pyrene probes by Vauhkonen et al. are the same, irrespective of the bilayers under consideration. Interleaflet association is expected to occur significantly for short lipids (*e.g.* DMPC) but to be disfavored for longer lipid (*e.g.* DOPC, DPPC, POPC) if there is a barrier preventing pyrene groups from interdigitating. Our coarse-grained model does not show evidence to this, but there is the possibility that it misses this point.

On the other hand, the results obtained by restricting pyrene association to same leaflet are closer from the body of published experimental coefficients. The Handbook of phospholipid bilayers published by Marsh [20] reports for DOPC at 25°C the following two values: $6.3\mu\text{m}^2.s^{-1}$ (fluorescence correlation spectroscopy) and 1.8 $\mu\text{m}^2.s^{-1}$ (electron spin resonance). Using an energy activation $E_a \sim 11$ kJ.mol^{-1}, these values transpose to respectively 5 and 1.4 $\mu\text{m}^2.s^{-1}$. It appears that the experimental diffusion coefficients reported in [20] are widely scattered, and much higher values of D are even reported. For POPC at 20°C a FRAP value of 3.4 $\mu\text{m}^2.s^{-1}$ is given. Again, it is consistent with our value in the absence of interleaflet association. Moreover, our new value is closer to FRAP than the original interpretation of the same data.

To conclude with diffusion coefficients, we find that when interleaflet association is allowed, our coefficients are a factor 2 smaller than those corresponding to fluorescent probe diffusion (FRAP or FCS). A better agreement is obtained by restricting pyrene association to probes occupying the same leaflet.

An outcome of the present work is the determination of the acceleration factor f of a Martini CG lipid bilayer model. At 10°C, f lies between 15 and 25, depending on interleaflet association. At 20°C it is reduced to 10-20. This is significantly higher than $f = 4$ which is sometimes assumed. The $f = 4$ factor corresponds indeed to the equivalent solvent (water) diffusion model, but seems higher as far as lipid motion is concerned. As the CG activation energy (14 kJ/mol) is likely to differ from the real activation energy, the agreement between CG model and reality should improve in the temperature range 300-330 K for which this model is supposed to perform best. Working at low temperatures enlarge the dynamical spread between numerical and real trajectories.

Coarse-graining raises the question of whether one can trust the resulting time correlation functions. There is no reason to assume that the acceleration factor applies uniformly for each time interval. If one denotes $C_{AB}^{CG}(t) = \langle A(t)B(0)\rangle$ the correlation function of a pair of observables, and $C_{AB}(t) = \langle A(t)B(0)\rangle$ the experimental (or all-atom simulated) counterpart, a correspondence $C_{AB}^{CG}(T(t)) = C_{AB}(t)$ is expected, with possibly a non-linear monotonous time correspondence $T(t)$ between the two correlations.

An homogeneous acceleration factor corresponds to $T(t) = t/f$. An inhomogeneous correspondence could explain why is the short time collisional dynamics faster than the long time diffusion process. Our work sets bounds on such a phenomenon. If interleaflet association is forbidden, the agreement between numerical and experimental values of D is consistent with an homogeneous acceleration factor. If interleaflet association is allowed, the time-scale dependent effective factor $f = 25$ (DOPC) or $f = 20$ (POPC) that acts on short time separation, reduced by a factor 2, would be again consistent with a diffusion coefficient of respectively 2 and 3.6 $\mu\text{m}^2.s^{-1}$.

Another way of slowing down the collision dynamics would be to challenge the diffusion limited character of the excimer formation, by requiring repeated collisions between monomers prior to complexation. This effect can be introduced by changing the excimer formation rate q in equation (14). For DOPC, interleaflet association allowed, a diffusion coefficient $D = 2.2\ \mu\text{m}^2.s^{-1}$ can be obtained by reducing q to a value such that it would take 1.1 ns of real time for the excimer to form, with both monomers maintained at close vicinity. This extra time could be related to a need of the terminal subgroups to align parallel, prior to excimer formation.

A drawback of slowing back in such a way the dynamics is that the effective survival probability becomes closer and closer to exponential shape, and therefore does not lead to the desired upward curvature of the $1/J_M(x)$ plot. Therefore, we do not find that it improves the agreement with experimental data to introduce such an intrinsic excimer formation time. A clue to whether such a delay is necessary, and its order of magnitude could be obtained from time-resolved excimer formation.

VI. CONCLUSION

We have presented a very general and efficient method to derive association kinetic coefficients in the case of diffusion limited processes, based on realistic molecular motions in lipid bilayers. The time-dependent reaction rate is derived from a survival probability, which itself comes from *a posteriori* trajectory analysis. A virtual relabeling of the simulated molecules enables us to efficiently gather collision statistics. No assumptions are made regarding the Brownian nature of the molecular motion, and intramolecular fluctuation effects are taken into account, within the limits of the coarse-graining procedure.

Our main assumptions are that lipid probes behave similarly to the major lipid components, and do not interact strongly with each other. We also require the dynamical acceleration factor of the coarse-grained numerical model to be uniform over the relevant time scales.

It is first shown that simulations at different sizes and temperatures can be compared, and used for the purpose of studying the collision dynamics between virtually labeled lipids. A likely capture radius $\rho_c = 0.5\ nm$ is obtained from a pair correlation analysis of the reactive groups.

Two main situations are considered, depending on whether interleaflet excimer association is allowed or not. Based on CG simulations considerations, interleaflet association should be allowed, but lead to small values of the diffusion coefficients. If one forbids interleaflet association, given that there could barriers opposing it that our CG model misses, the resulting diffusion constants fall in a range comparable to other independent experimental procedures.

The possibility of an intrinsic excimer formation time is not completely ruled out, but does not seem to improve the agreement with the experimental data that were used throughout this study.

In any case, our approach leads to a significant reduction of the diffusion coefficients compared to those originally published. We suggest that the coefficients found in similar diffusion limited processes, which often lie above the values obtained from long range fluorescent probes diffusion, should be reanalyzed along the lines of our present approach. We suspect that these diffusion coefficients are overestimated due to analysis bias, as our example shows.

Our standing is that we have possibly explained the discrepancy between these two different approaches to lipid diffusion determination. More modeling work is needed in order to determine the degree of interdigitation of pyrene groups pertaining to different leaflets, as well as regarding the effect of non trivial dispersion forces between resonant fluorescent groups.

The application of this technique to complex membranes with dynamical heterogeneities would certainly be interesting, now that a convenient framework for diffusion limited reaction rate analysis, based on molecular dynamics, is available.

AUTHOR CONTRIBUTIONS

P.A. did the simulation and numerical work, the data fitting and composed the figures (4-9). F.T. wrote the manuscript. Both authors contributed to the theoretical model and to figures (1-3).

ACKNOWLEDGMENTS

F.T. would like to thank G. Duportail, C.M. Marques and J. Léonard for discussions. The authors acknowledge support from the High Performance Cluster Equip@Meso of the University of Strasbourg for providing computational

resources.

[1] Hans-Joachim Galla and Erich Sackmann. Lateral diffusion in the hydrophobic region of membranes: use of pyrene excimers as optical probes. *Biochimica et Biophysica Acta (BBA) - Biomembranes*, 339(1):103 – 115, 1974.

[2] Siewert J. Marrink, H. Jelger Risselada, Serge Yefimov, D. Peter Tieleman, and Alex H. de Vries. The martini force field: coarse grained model for biomolecular simulations. *The Journal of Physical Chemistry B*, 111(27):7812–7824, 2007. PMID: 17569554.

[3] M. Vauhkonen, M. Sassaroli, P. Somerharju, and J. Eisinger. Dipyrenylphosphatidylcholines as membrane fluidity probes. relationship between intramolecular and intermolecular excimer formation rates. *Biophysical Journal*, 57(2):291 – 300, 1990.

[4] M. Sassaroli, M. Vauhkonen, D. Perry, and J. Eisinger. Lateral diffusivity of lipid analogue excimeric probes in dimyristoylphosphatidylcholine bilayers. *Biophysical Journal*, 57(2):281 – 290, 1990.

[5] J. B. Birks. Excimers. *Reports on Progress in Physics*, 38(8):903, 1975.

[6] Pentti Somerharju. Pyrene-labeled lipids as tools in membrane biophysics and cell biology. *Chemistry and Physics of Lipids*, 116(12):57 – 74, 2002.

[7] Eurico Melo and Jorge Martins. Kinetics of bimolecular reactions in model bilayers and biological membranes. a critical review. *Biophysical Chemistry*, 123(23):77 – 94, 2006.

[8] H.-J. Galla, W. Hartmann, U. Theilen, and E. Sackmann. On two-dimensional passive random walk in lipid bilayers and fluid pathways in biomembranes. *The Journal of Membrane Biology*, 48:215–236, 1979.

[9] Jorge Martins, Winchil L. C. Vaz, and Eurico Melo. Long-range diffusion coefficients in two-dimensional fluid media measured by the pyrene excimer reaction. *The Journal of Physical Chemistry*, 100(5):1889–1895, 1996.

[10] Jorge Martins and Eurico Melo. Molecular mechanism of lateral diffusion of py10-pc and free pyrene in fluid {DMPC} bilayers. *Biophysical Journal*, 80(2):832 – 840, 2001.

[11] EG Novikov and AJWG Visser. Inter- and intramolecular dynamics of pyrenyl lipids in bilayer membranes from time-resolved fluorescence spectroscopy. *Journal of Fluorescence*, 11(4):297–305, 2001.

[12] K. Razi Naqvi. Diffusion-controlled reactions in two-dimensional fluids: discussion of measurements of lateral diffusion of lipids in biological membranes. *Chemical Physics Letters*, 28(2):280 – 284, 1974.

[13] K.Razi Naqvi, Jean-Paul Behr, and D. Chapman. Methods for probing lateral diffusion of membrane components: triplet-triplet annihilation and tripletttriplet energy transfer. *Chemical Physics Letters*, 26(3):440 – 444, 1974.

[14] D. C. Torney and H. M. McConnell. Diffusion-limited reaction rate theory for two-dimensional systems. *Proceedings of the Royal Society of London. A*, 387(1792):147–170, 1983.

[15] Attila Szabo. Theory of diffusion-influenced fluorescence quenching. *The Journal of Physical Chemistry*, 93(19):6929–6939, 1989.

[16] Huan-Xiang Zhou. Rate theories for biologists. *Quarterly Review of Biophysics*, 43(2):219–293, 2010.

[17] M. J. Stephen. Firstorder dispersion forces. *The Journal of Chemical Physics*, 40(3):669–673, 1964.

[18] Gregor Cevc and Derek Marsh. *Phospholipid Bilayers. Physical Principles and Models.* John Wiley & Sons, New-York, 1987.

[19] Berk Hess, Carsten Kutzner, David van der Spoel, and Erik Lindahl. Gromacs 4: algorithms for highly efficient, load-balanced, and scalable molecular simulation. *Journal of Chemical Theory and Computation*, 4(3):435–447, 2008.

[20] Derek Marsh. *Handbook of Lipid Bilayers.* CRC Press, Boca Raton, 2nd edition, 2013.

Chapter 4

Peroxidised Lipid Mixtures

A pure liquid is by definition made of a single component or chemical species. We define a solution as an homogeneous mixture of more than one compound. In this chapter we address the question of mixing between two different lipid species. For instance, how does the average area per lipid depend on concentration, does it exist of a mean interaction potential, is the system stable with respect to lateral lipid separation?

Our approach will again be based on the Martini model, and systems with various lipid concentrations will be systematically investigated. These systems are binary lipid mixtures, with one species having an unsaturated lipid chain, and the other the corresponding peroxidised lipid chain.

The model for peroxidised lipid chains has been introduced in ref. [2], it defines a single peroxidised molecule HP-POPC obtained by modifying a POPC lipid, and a double peroxidised lipid molecule DHP-DOPC derived from a DOPC lipid. The HP-POPC molecule will also sometimes be referred as POBU, and DHP-DOPC as DOBU.

1 Introduction

1.1 Peroxidised lipids

Auto-oxidation Lipid peroxidation is a molecular reaction that consists in adding a peroxide group OOH at a cis-unsaturated double bond in the unsaturated chain. Lipid peroxides can be the result of free radical chain propagation, or a direct interaction with singlet oxygen. The radical mechanism is composed of three steps:

Initiation. In this step, one phospholipid reacts with one initiator, usually reactive oxygen species (ROS: reactive molecules containing oxygen). The initial step produces water and lipid radicals.

$$LH + ROS \longrightarrow L^* + H^* \tag{4.1}$$

Propagation. The fatty acid produced during the initiation process is very unstable. The molecular reaction between the lipid radical and a free oxygen creates another unstable product, peroxyl-fatty acid radical. The peroxyl radical combines with another fatty acid hydrogen creating a lipid peroxide in the process. A product of this reaction is a fatty acid radical ensuring the continuation of the cycle.

$$\begin{gathered} L^* + O_2 \longrightarrow LOO^* \\ LOO^* + LH \longrightarrow LOOH + L^* \end{gathered} \tag{4.2}$$

Termination. The end of the cycle is achieved principally when two radicals react with each other creating a non radical molecule, therefore breaking the chain reaction of a radical combining with a non radical to produce a radical. The probability of the terminating the oxidation reaction increases with the concentration of the radicals.

$$\left.\begin{array}{l} 2LOO^* \\ LOO^* + L^* \\ 2L^* \end{array}\right\} \quad \longrightarrow \quad \text{Nonradical products} \tag{4.3}$$

Lipid peroxides are usually only intermediates in the lipid degradation cascade. They are themselves subject to further degradation.

Photooxidation processes Photooxidation takes place when excitable molecules (dye, fluorescent group) transfer their energy to dioxygen molecules, producing singlet oxygen. The singlet oxygen diffuses and creates a peroxide upon reaction with an unsaturated carbon-carbon bond. This way of making ROS is called dye sensitization. Excited dyes sometimes interact directly with the unsaturation, which result in further chain degradation such as cleavage, aldehyde or carboxylic group formation.

As shown in ref. [9], in-vitro photooxidation can be achieved in a very controlled manner, so that peroxides are quasi-exclusively produced. This is how some of the structural properties of peroxidised lipid bilayers were obtained, which in turn were the basis of the parametrization of the numerical Coarse-Grained model. Another crucial observation is that fully peroxidised bilayers are found to be experimentally stable, either resulting from in-situ photooxidation, or from giant vesicles grown out of oxidised lipid products. It therefore makes sense to perform simulations of fully or partially peroxidised lipid bilayers.

Consequences of lipid oxidation Lipid oxidation is subject to sophisticated in-vivo control mechanism. This is a crucial issue in mitochondria, which are the place for respiration and energy producing metabolic reactions. On the other hand, biological membrane composition comprises unsaturated chain groups such as POPC, or even polyunsaturated chains in nerve cells. Lipophilic anti-oxidant molecules are present in the membrane, with the purpose of trapping ROS and preventing the attack of those unsaturated species, along with other targets (cholesterol, proteins,. . .).

A low level of oxidised product is allowed (and probably normal) in biological membranes. An excessive amount of oxidised product is harmful. Studies of model bilayer lipid oxidation is therefore instructive as far as understanding the mechanisms of oxidized membranes possible dysfunctions. Fully peroxidised membranes is an extreme situation, characterized by a smaller stretching elastic coefficient and a larger area per lipid [9], a thinner membrane and a softer bending modulus (according to [2]). A thinner membrane, for instance, could give rise to anomalous hydrophobic matching interaction between transmembrane proteins. It is also believed that water permeation is significantly increased [99] and pore formation facilitated.

When mixtures are considered, a natural question arises as far as whether mixtures are stable. It is well known that mixtures of saturated and unsaturated phospholipid molecules can lead to binary phase separation, due to gel-fluid mutual incompatibility. Oxidation (not just peroxidation) of model lipid membrane is usually associated with membrane permeation prior to membrane destruction, a situation for which a mechanism based on the possible aggregation of oxidized species was put forward [100]. It is therefore crucial to determine whether lipid peroxides are prone to separation or not.

1.2 Solutions and mixtures

Binary solutions are classically described in terms of theory of regular solutions. According to this thermodynamical approach, a free-energy difference associated to mixing is introduced, which reads

$$\frac{1}{kT}\Delta G_{\mathrm{mix}}(x_1, x_2) = x_1 \ln x_1 + x_2 \ln x_2 + \chi_{11} x_1^2/2 + \chi_{12} x_1 x_2 + \chi_{22} x_2^2/2 \tag{4.4}$$

with x_1 and x_2 the molar fraction of each binary species. The term $x_1 \ln x_1 + x_2 \ln x_2$ is the (ideal) entropy of mixing, while the quadratic term represents non ideal interaction corrections. Such an approach is expected to be valid so long as the two species are similar in terms of structure and chemistry to the extent that substituting one species for the other does not cause a radical reorganization of the local fluid structure.

For dilute species, a perturbative approach is possible, based on the virial expansion, which makes it possible to express the interaction coefficient χ in terms of radial distribution functions. A more advanced approach relates the χ coefficients of the theory of regular solutions to the direct correlation functions of the fluids. These relations are outlined in the Appendix A2. Again, the χ_{ab} can be expressed in terms of space integrals of the radial distribution functions.

Two species are prone to mixing is the combination $\chi = \chi_{12} - (\chi_{11} + \chi_{22})/2$ is negative, and prone to demixing otherwise. The function $\Delta G(x, 1-x)$ must be convex for any value x between 0 and 1. According to this model, the two species separates as soon as $\chi > 2$.

1.3 Radial Distribution Function

The radial distribution function (rdf) (see figure 4.1), also known as pair correlation function, measures the probability of finding a particle at a distance r from a reference particle. In the case of ordinary liquids, the rdf is a powerful investigation tool that allows one to calculate macroscopic thermodynamic properties. Furthermore, knowledge of the pair correlation $g(r)$ yields information on the local structure of simple and complex fluids.

Radial distribution function of a pure system If we consider a system of N identical particles in a volume V at a temperature T, the probability density that the N particles are at the positions $\mathbf{r}_1, \mathbf{r}_2, ..., \mathbf{r}_N$ reads:

$$P_N(\mathbf{r}^N) = \frac{e^{-\beta U(\mathbf{r}^N)}}{Z_N(V,T)}, \tag{4.5}$$

where Z is the partition function in the canonical ensemble:

$$Z_N(V,T) = \int \mathrm{d}\mathbf{r}^N e^{-\beta U(\mathbf{r}^N)} \tag{4.6}$$

$$g_N(r) = \frac{V}{N(N-1)} \int \mathrm{d}\mathbf{r}^N P_N(\mathbf{r}^N) \sum_{i \neq j} \delta(\mathbf{r} - \mathbf{r}_j + \mathbf{r}_j) \tag{4.7}$$

$\rho g_N(r)$ is the average density of particles at a distance r from the reference one, and integrating $\rho g_N(r)$ over the volume leads to total number of particles minus the one used as a reference.

$$\rho \int_V \mathrm{d}\mathbf{r} g_N(r) = N - 1 \tag{4.8}$$

From the definition of $g_N(r)$ in eq. (4.7), one can deduce some of the properties of the pair correlation function: at large distances $r \gg$ correlation length $\xi(T)$, particles are decorrelated. The presence of the reference particle at a position r_0 does not affect the position of another particle at position r far apart. The fluid is uncorrelated, as in an ideal gas. This corresponds to a pair correlation $g(r \to \infty) = 1$. Introducing $h(r) = g(r) - 1$ one also has $h(r \to \infty) = 0$.

Rdfs can be computed numerically from molecular dynamics simulations, based on histograms of mutual relative distances, averaged over MD trajectories.

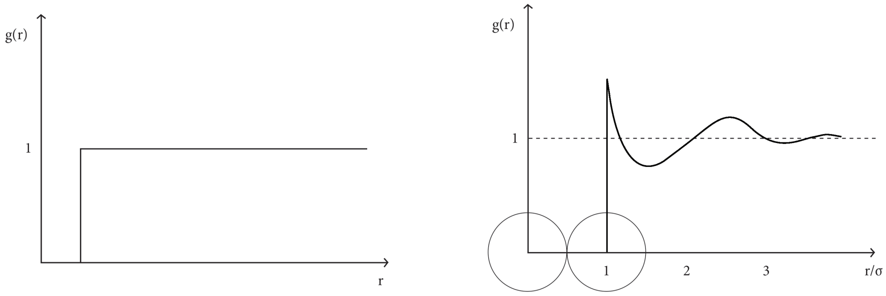

(a) Gas **(b)** Hard sphere

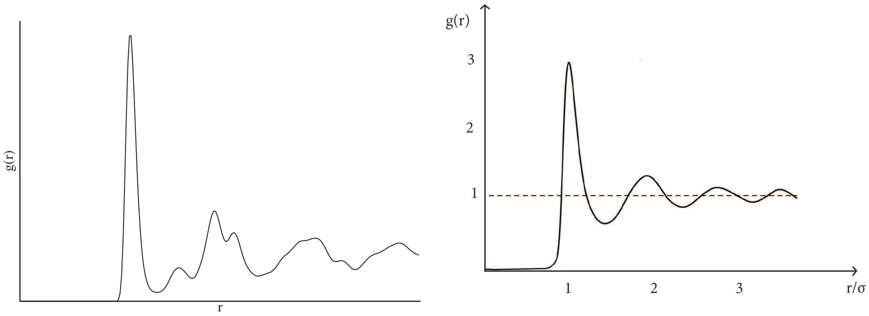

(c) Solid **(d)** Liquid

Figure 4.1: Examples of pair correlation functions. (a) is $g(r)$ for a *VDW gas*, showing a hard sphere repulsion in the beginning and a uniform distribution otherwise. The $g(r)$ of a *Lennard-Jones liquid* (d), and of *hard spheres* (b). (c) shows the pair correlation for solids which have long range order.

Determining $g(r)$ experimentally for simple liquids The pair correlation function in molecular fluids can be determined experimentally by scattering experiments. The purpose of scattering experiments is to probe local ordering over distances of the order of the particle size and nearest-neighbour distance. Therefore, X-rays and neutron scattering are used for atomic liquids where distances are of the order of Ångstroms, while colloidal systems are probed by light and low angle neutron scattering since sizes and distances are fractions of microns.

During a scattering experiment, monochromatic radiation of wavelength λ interacts with the sample, and is scattered in the process at an angle θ. The deviated beam goes into a detector which measures its average intensity. For scattering from spherical particles:

$$I(q) \propto \langle N \rangle P(q) S(q), \tag{4.9}$$

where $\langle N \rangle$ is the average number of particles in the illuminated region of sample, q is the modulus of the wave vector $\mathbf{q} = \mathbf{K}_f - \mathbf{K}_i$. The form factor $P(q)$ contains information on the particle size and form. $S(q)$ is called structure factor and it reveals information related to the inter-particle interactions and correlations. By definition the static structure factor can be written as :

$$S(q) = \left\langle \frac{1}{N} \sum_{i,j}^{N} e^{i\mathbf{q}(\mathbf{r}_i - \mathbf{r}_j)} \right\rangle = \left\langle \left| \frac{1}{\sqrt{N}} \sum_{i}^{N} e^{i\mathbf{q}.\mathbf{r}_i} \right|^2 \right\rangle, \tag{4.10}$$

where the brackets denotes an equilibrium ensemble average. If we consider $q = 4\pi/\lambda \sin(\theta/2)$, by expanding the double sum for $i = j$ and $i \neq j$, and using the definition of $g(r)$, the structure factor reads

$$S(q) = 1 + \rho \int \mathrm{d}\mathbf{r} e^{i\mathbf{q}.\mathbf{r}} [g(r) - 1] = 1 + 4\pi\rho \int_0^\infty \mathrm{d}r\, r^2 h(r) \frac{\sin(qr)}{qr} \tag{4.11}$$

Eq.(4.11) establishes a relation between the structure factor and the pair correlation function: $S(q) - 1$ is the Fourier transform of $\rho\, h(r)$. As a conclusion, knowing $S(q)$ allows the calculation of $h(r)$ and thus $g(r)$.

1.4 Theoretical determination of $g(r)$ and the Orstein-Zernike equation

Properties of liquids can be related to integrals of the pair correlation function $g(r)$ and pair interaction potential $u(r)$ through several means such as the energy equation, the pressure equation and the compressibility equation (Appendix A2).

In the precedent section, we discussed how to determine $g(r)$ experimentally through scattering, we proceed to present theoretical methods to calculate the distribution function. These methods are based on the Orstein-Zernike (OZ) equation, that defines the direct correlation $c(r)$ and relates it to the total correlation function $h(r)$. The Orstein-Zernike equation of a homogeneous and isotropic system is given by

$$h(r_{12}) = c(r_{12}) + \rho \int \mathrm{d}\mathbf{r}_3 \, c(r_{13}) h(r_{23}) \tag{4.12}$$

The OZ equation can be interpreted physically as the following: the total correlation function is a measure of the influence of a particle i on a particle j, separated by a distance r_{ij}. The influence can be split into a direct and indirect contribution. The direct correlation function $c(r_{ij})$ determines the direct contribution. Assuming that particle i affects a third particle k, which in turn, influences particle j then the indirect part is related to this indirect correlation due to direct correlations between intermediate particles and is expressed as the integral of this processes over all possible positions of particle k.

In order to determine the pair correlation function from the OZ equation, additional relations between the direct correlation $c(r)$ on one hand, and the pair potential $u(r)$ and total correlation $h(r)$ on the other hand, are needed. These relations are known as closure relations. These approximations, combined with the OZ equation, give integral equations for $g(r)$ which can be solved numerically to provide an “analytical” expression for the pair correlation. Unfortunately, none of these closure equations provides the true pair correlation $g(r)$ starting from a pair potential $v(r)$.

Such closure terms could be used in a reverse way, to extract effective pair potential out of correlation functions. From simpler to more sophisticate, one has

- the potential of mean force $g(r) = \exp(-v(r))$ which relates the pair potential to the rdf directly in real space
- the random phase approximation (RPA) which assumes that $c(r) = -\beta v(r)$
- more complex closure equations such as Percus-Yevick $g(r) = e^{-\beta v(r)}(g(r) - c(r))$ which mixes total and direct correlation functions in real space

None of these scheme is fully thermodynamically consistent.

1.5 Liquid state approach of lipid mixtures

Phospholipid bilayers can be seen as quasi 2-dimensional (2d) fluids. Coarse-grained models are themselves molecular fluids comprising between 10 and 16 beads. To fully benefit from the concepts and method of the theory of simple liquids, one must further reduce the complexity of these systems by reducing the molecules *e.g.* to *center of masses*. The x, y projection of the lipid center of masses can be seen as a 2d fluid, for which the rdf can be easily obtained. However, one cannot expect that this 2d fluid is ruled by pairwise interactions, unlike most simple liquids models. It is clear that any pair potential derived in this way will be a phenomenological effective potential.

In practice, due to lack of time, we will only extract potentials of mean forces from the radial distribution functions.

1.6 Mixtures of coarse-grained peroxidised lipids

We use molecular dynamics simulations to characterize the effect of lipid peroxidation on the properties and structure of 1-palmitoyl-2-oleoyl-sn-glycero-3-phosphocholine (POPC) lipid bilayers and 1,2-dioleoyl-sn-glycero-3-phosphocholine (DOPC) bilayers at different oxidation levels.

Models for coarse-grained peroxidized lipids have been proposed by Guo et al. [2]. They consist in a slightly modified version of a DOPC lipid where a peroxide group OOH [2] has been added to the hydrophobic chain right at the unsaturated C=C bond. The same was done on POPC. We will refer to these coarse-grained model of hydroperoxidized lipids as DHP-DOPC and HP-POPC, but also DOBU and POBU (fig. 4.2).

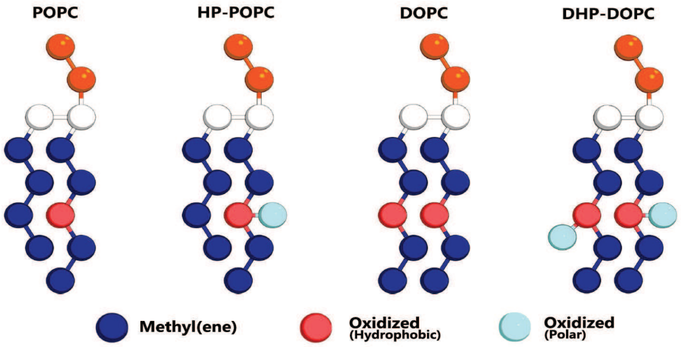

Figure 4.2: Schematic representation of the oxidised lipid molecules HP-POPC and DHP-DOPC based on MARTINI coarse-grained models for POPC and DOPC phospholipids respectively (adapted from [2]).

2 Bilayer setup and simulation details

The systems were generated starting from an equilibrium configuration of a DOPC bilayer containing 512 lipids. We replaced 16, 128 and 256 DOPC lipid molecules with DHP-DOPC, obtaining in the process three different bilayers with oxidized lipid concentrations of 3.1%, 25% and 50%, respectively. The DOPC bilayer is symmetric, containing 256 lipid per leaflet, and the oxidised lipids were equally distributed on both leaflets, so that the two bilayer leaflets contained the same number of oxidised lipids and total number of lipids. All these systems consisted of 512 lipids molecules (normal and oxidised lipids), and 3072 CG-water molecules.

The preparation scheme consists in three steps: 1/ renaming molecules and adding the peroxide group, 2/ energy minimization/relaxation, 3/ thermalization/equilibration.

The second step is a non-dynamical run, where no kinetic energy is given, *i.e* temperature is set to zero. This minimization is needed before starting MD runs to relax large stresses consecutive to changing the identity or number of beads present in the system. Starting from a stressed configuration commonly leads to simulation crashes in spite of the presence of a regulating thermostat.

The minimization step results in a configuration with a minimum potential energy (inherent structure) close to the starting configuration. Then we perform an equilibration run for another 40 ns. During equilibration, we allow the bilayer to evolve while coupled to thermostats and, in this case, barostats. We used the Nose-Hoover thermostat in this step. For the barostat, we used a semi-isotropic pressure coupling with transverse z direction normal to the bilayer [83].

Once the system is equilibrated, we performed a total run of 10 μs, with an integration step of 40 fs. We remained in the NPT ensemble where the temperature was fixed to 300K using the *v-rescale* heat bath and a semi-isotropic *Parrinello-Rahman* barostat keeping separately the pressure constant at 1 bar along both of the xy plane and the z axes. This normally ensures that the bilayer is tension free.

The same simulation scheme was applied to POPC bilayers mixed with the hydroperoxidised lipid HP-POPC. The trajectories generated by the runs are analyzed *a-posteriori*, leading to radial distribution functions, or area per lipid values.

2.1 Results

Pair correlation functions The lipids are first separated into two categories, depending on which leaflet they belong. Each leaflet is treated as a distinct system, even though both leaflets should lead to the same statistical distribution by symmetry. Then, center of masses are extracted.

We computed the pair correlation functions $g(r)$ using the **g_rdf** analysis tools, which is part of the gromacs-4.6 package. This application builds histograms of relative distances between centres of masses averaged over a given trajectory. If

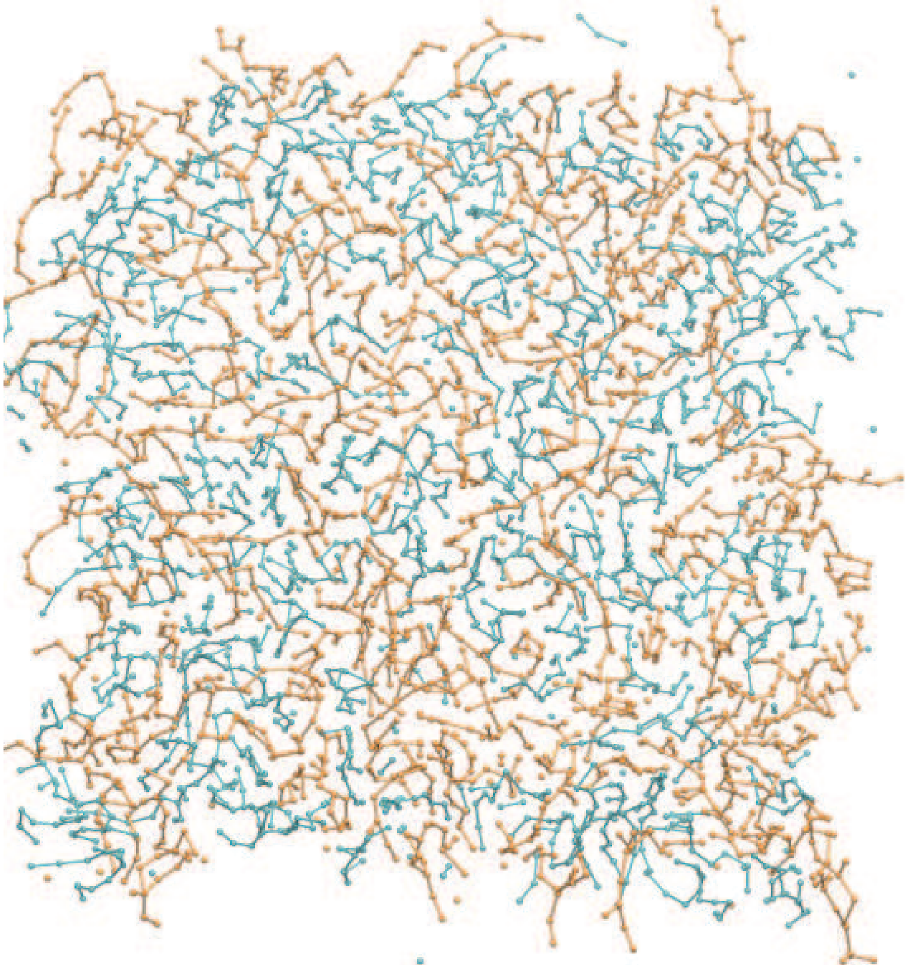

Figure 4.3: Top view of a POPC:HP-POPC bilayer for an oxidation concentration of 50% (cyan POPC, orange HP-POPC).

molecules are labelled according to their molecular type (A or B), the functions $g_{AA}(r), g_{AB}(r)$ et $g_{BB}(r)$ can be obtained, where each function is defined as

$$\begin{aligned} g_{AA}(r) &= \frac{1}{\langle\rho_A\rangle_{local}}\frac{1}{N_A}\sum_{i\in A}^{N_A}\sum_{j\in A}^{N_A}\frac{\delta(r_{ij}-r)}{4\pi r^2} \\ g_{AB}(r) &= \frac{1}{\langle\rho_B\rangle_{local}}\frac{1}{N_A}\sum_{i\in A}^{N_A}\sum_{j\in B}^{N_B}\frac{\delta(r_{ij}-r)}{4\pi r^2} \\ g_{BB}(r) &= \frac{1}{\langle\rho_B\rangle_{local}}\frac{1}{N_B}\sum_{i\in B}^{N_B}\sum_{j\in B}^{N_B}\frac{\delta(r_{ij}-r)}{4\pi r^2} \qquad (4.13) \end{aligned}$$

where $\langle\rho_B\rangle_{local}$ is the average density of particles B sitting in a sphere surrounding

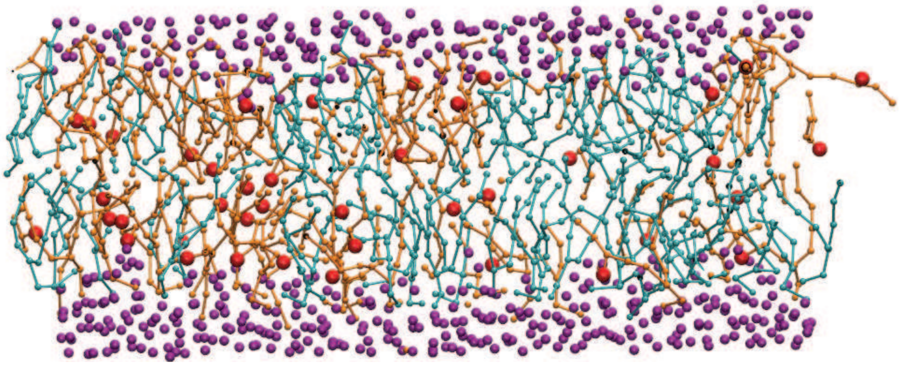

Figure 4.4: Side view of a POPC:HP-POPC bilayer for an oxidation concentration of 50% (cyan POPC, orange POPC, violet water, red peroxide side groups).

particles A of a radius r_{max}, usually taken to be half of the simulation box length. Numerically, the delta function becomes an histogram bin with a width equal to δr.

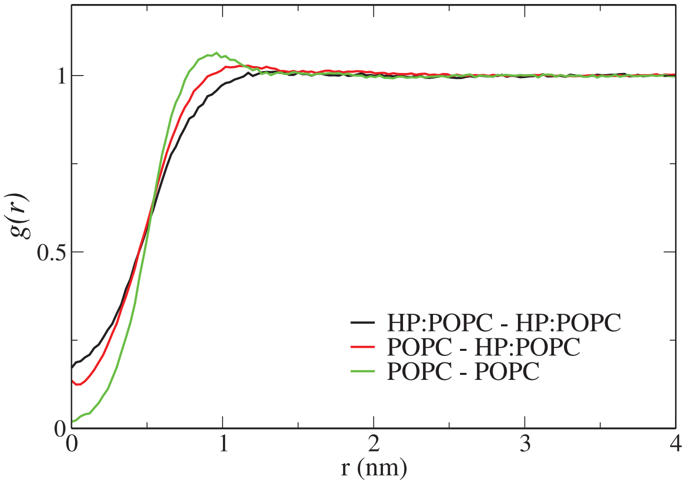

Figure 4.5: The pair correlation function of POPC:HP-POPC bilayers for an oxidation concentration of 50%.

Figure 4.5 displays the pair correlation function of a POPC : HP-POPC bilayer, in which half of the lipids were peroxidized. The radial distribution function was computed for POPC : POPC pairs, HP-POPC : HP-POPC and POPC : HP-POPC pairs, represented by the respective curves. For large pair separation r_{ij}, all three curves converge to 1, which is one of the properties of the pair correlation function:

$g(r) \xrightarrow{r\to\infty} 1$.

There is a difference with hard sphere models or Lennard-Jones models at short separations (near the origin $r = 0$), of the order of the size of the average bead radius.

We attribute this divergence to the fact that the trajectories used in the calculations of the correlation functions correspond to the center of mass of the lipids. The effective interaction is therefore softer, and there is also a non vanishing probability that two centers of mass occupy the same projected position in x, y.

The first maxima of the pair correlation functions follow the order $g_{\text{POPC-POPC}} > g_{\text{POPC-HP:POPC}} > g_{\text{HP:POPC-HP:POPC}}$.

Figure 4.6 represents the correlation function of a DOPC : DHP-DOPC bilayer where the oxidation ratio is at 50%. The curves display similar behaviour compared to the ones of POPC : HP-POPC bilayer for large pair separation and distances smaller than bead size. However, a slight difference can be observed in the order of the maxima. For the DOPC : DHP-DOPC bilayer, we found $g_{\text{DOPC-DOPC}} > g_{\text{DHP:DOPC-DHP:DOPC}} > g_{\text{DOPC-DHP:POPC}}$.

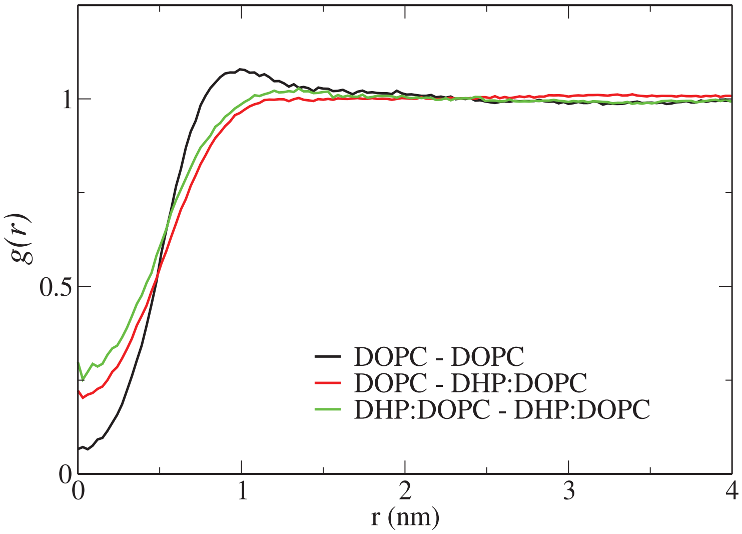

Figure 4.6: The pair correlation function of DOPC:DHP-DOPC bilayers for an oxidation concentration of 50%

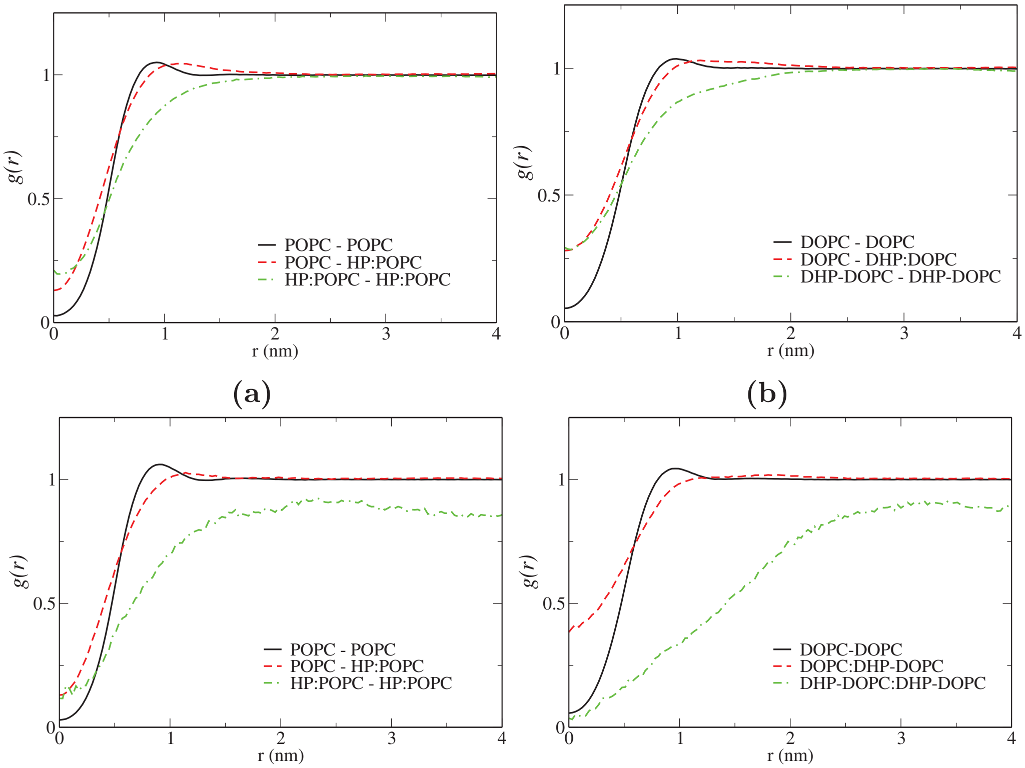

(a) **(b)**

(c) **(d)**

Figure 4.7: The pair correlation function of POPC:HP-POPC (a,c) and DOPC:DHP-DOPC (b,d) bilayers for an oxidation concentration of 25% (a,b) and 3.1% (c,d).

Figure 4.7 displays the pair correlation function of POPC : HP-POPC bilayers (Fig. 4.7a and 4.7c) and DOPC : DHP-DOPC bilayers (Fig. 4.7b and 4.7d) for an oxidised lipid concentration of 25% and 3.1%. Note that *g_rdf* does not normalize to 1 and the number of molecules is small (8 oxidized molecules in the case of 3.1%).

Pair interaction potential

We now derive from the previous rdfs, the corresponding potential of mean forces. This corresponds to the simplest possible closure scheme for the $g(r)$. This is a rough kind of mean-field approximation where indirect particle correlations are not taken at all into account. In the case of simple fluids, the pair distribution function reads

$$g(r) = e^{-\beta u(r)} \tag{4.14}$$

Equation (4.14) holds for fluid mixtures. For a system containing two species A and

B, the potential of mean force approximation is the following:

$$g_{AB}(r) = e^{-\beta u_{AB}(r)} \tag{4.15}$$

Thus, computing the logarithm of the pair correlation function is sufficient to determine the pair interaction potential:

$$u^{(pmf)}(r) = -\frac{1}{\beta} \ln\left(g(r)\right) \tag{4.16}$$

Figure 4.8 represents the effective pair interaction potential between all possible pairs in a DOPC : DHP-DOPC and POPC : HP-POPC bilayers. The interaction potential curves vanish for large separation as a result of $g(r) \longrightarrow 1$, this is only natural due to absence interactions (correlation) between the pairs for large separations. The negative part of the interaction potential is an indication on the presence of a weak attraction between pairs. This part was absent for the DHP-DOPC : DHP-DOPC as well as HP-POPC : HP-POPC interaction in all of the simulated systems.

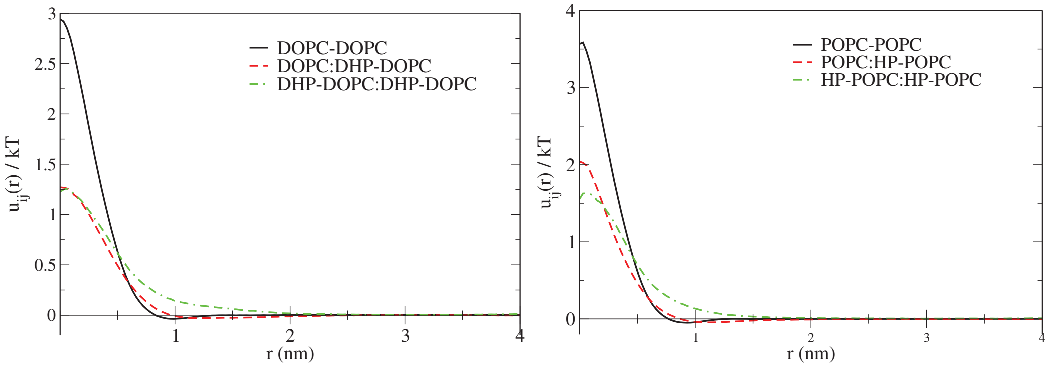

(a) DOPC:DHP-DOPC **(b)** POPC:HP-POPC

Figure 4.8: The pair interaction potential of DOPC:DHP-DOPC and POPC:HP-POPC bilayers for an oxidation concentration of 25%

In addition, we compare the potentials for each pair as a function of the oxidation concentration. In order to be valid, a pair interaction potential should not depend on the system concentrations. In other terms, one must check whether the pair interaction potential remains constant for different oxidation levels. This assumption is tested in Fig. 4.9. However, the more the particles are diluted, the more inconsistent the results were. This can be interpreted by lack of statistics, such is the case of the correlation function of the oxidized DOPC lipids 4.7d (in green).

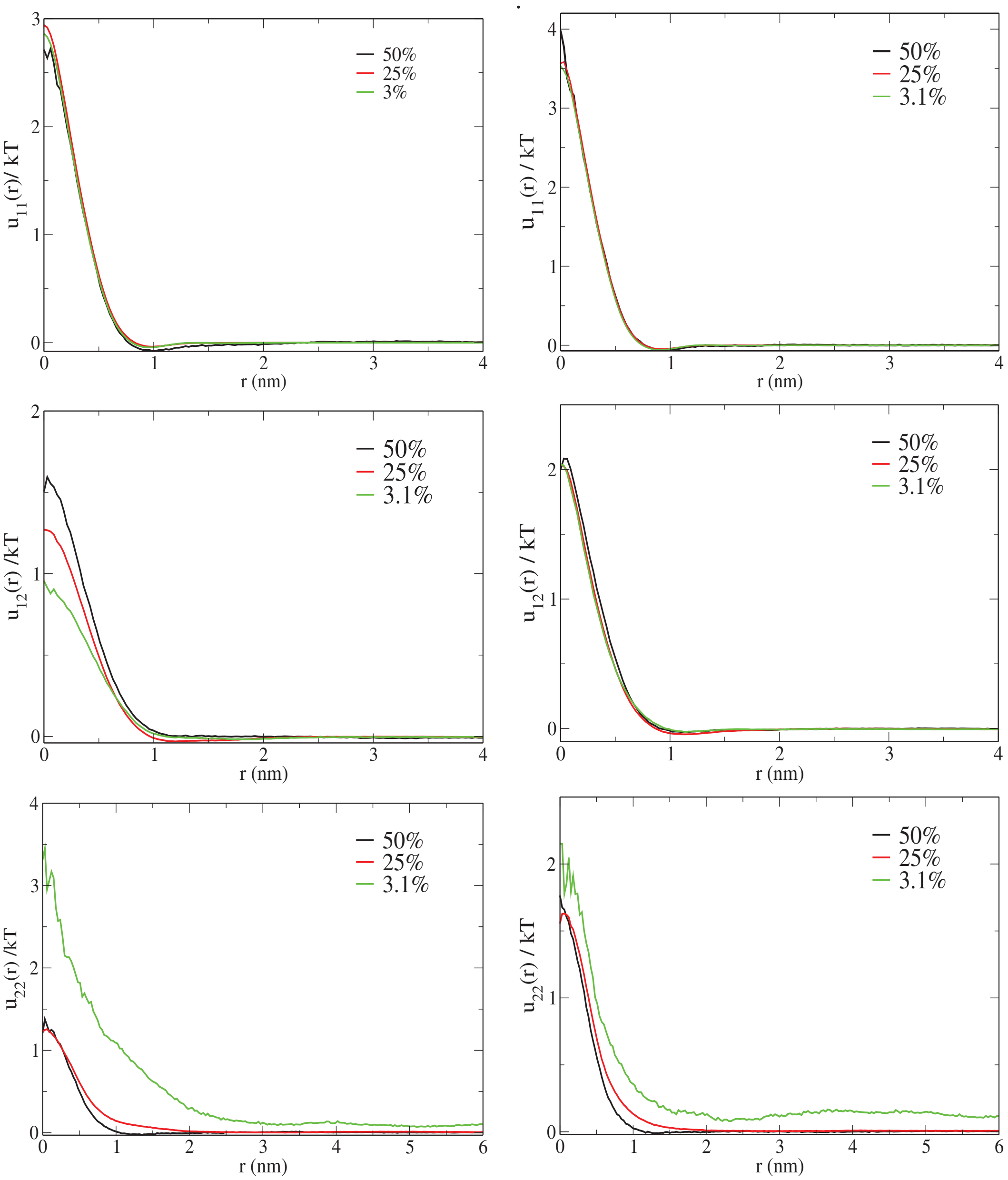

Figure 4.9: The pair interaction potential of DOPC:DHP-DOPC (left) and POPC:HP-POPC (right) bilayers for different concentrations. Subscripts refer to the species; 1 indicates the normal phospholipid while 2 indicates the hydroperoxidized lipid.

	Concentration of oxidised lipids (%)	Interaction parameter χ	χ_{11}	χ_{22}	χ_{12}
DOPC:DHP-DOPC	3.1	-4.058	0.978	8.538	0.67
	25	$-1{,}074$	1.027	2.371	0.625
	50	0,391	0.573	0.934	1.145
POPC:HP-POPC	3.1	-1.002	0.882	2.789	0.971
	25	-1.062	1.039	2.346	0.629
	50	-0.253	0.924	1.242	0.829

Table 4.1: Mixing parameters for DOPC:DHP-DOPC and POPC:HP-POPC bilayers. The χ parameters were determined using Eq. (A2.14). $\chi \leq 0$ indicates that the mixture is prone to mixing. In contrast, a positive χ suggests separation.

Determination of the mixing parameter χ

The χ parameters were determined using the virial approximation scheme exposed in (A2.14), page 113. For a 75:25 mixtures of POPC-HP-POPC for example, one finds that $\chi_{11} = 1.039$, $\chi_{12} = 0.629$, $\chi_{22} = 2.346$ and therefore negative value for $\chi = -1.062$ which indicates that lipid and peroxidized lipid are prone to mixing. The χ parameters were calculated for the other mixtures as well, the results are shown in Table 4.1. All the systems simulated were subject to mixing, for the exception of the 50:50 mixture of DOPC/DHP-DOPC lipids. In fact, we found a positive mixing parameter, which suggests that the system tends to demix, but only weakly ($\chi \leq 2$).

Average area per lipid

Area per lipids are one of the most important structural parameters in lipid fluid bilayers. The determination of the area per lipid usually comes from X-rays and neutron scattering, and is always challenging [101]. On the other hand, area per lipids of fully peroxidized bilayers were directly measured on giant vesicles systems [9, 102], and area per lipids for peroxides mixtures should in principle, be measurable.

We measured the average area per lipid in the simulated systems for the different concentration (Table 4.2). We also show the thickness of the simulation box. The results are displayed in fig. 4.10. For both lipid mixtures, the area per lipid increases with concentration of the oxidised lipids, while the thickness decreased, as expected. This increase in area per lipid is consistent with experimental results showing that

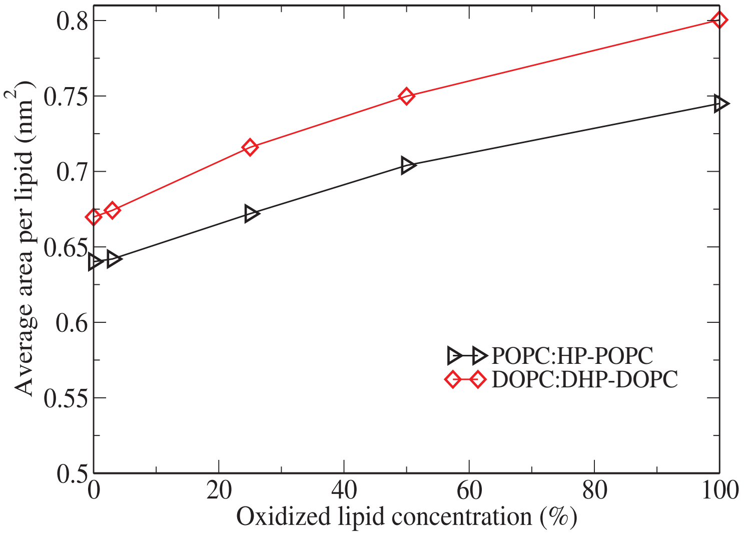

Figure 4.10: Average area per lipid for DOPC:DHP-DOPC and POPC:HP-POPC bilayers for various oxidation concentrations.

peroxide radical comes into contact with water [10, 11]. The average area per lipid does not increase linearly with concentration, displaying some kind of non-ideal area of mixing.

The area per lipid change upon peroxidation is usually interpreted in terms of exposure of the peroxide group to the water interfacial region. It was observed that there is a non trivial balance between the ratio of peroxides exposed to the interface, and the peroxides remaining buried inside the hydrophobic membrane core. The observed average area per lipid should reflect this balance.

3 Summary

To sum up, we considered mixtures of oxidized-non oxidized lipid species and we computed the rdf of the center of masses. Within the virial approximation, we derived effective mixing parameters which indicate that peroxidized lipids do not want to separate from the original lipids, except perhaps for 50:50 DOPC/DHP-DOPC systems. It seems that interaction are not repulsive enough to induce separation.

A potential of mean-force can be extracted. For POPC systems, it does not depend so much on the oxidized concentration. For DOPC systems, the situation seems slightly more complex, the effect of oxidation being stronger.

	Concentration of oxidised lipids (%)	Average area per lipid (nm^2)	Average box thickness (nm)	Average volume (nm^3)
DOPC:DHP-DOPC	0	0.67	6.57	1127.67
	3.1	0.674	6.54	1129.6
	25	0.716	6.25	1145.63
	50	0.75	6.07	1165.19
	100	0.8	5.87	1203.55
POPC:HP-POPC	0	0.64	6.551	1072.04
	3.1	0.642	6.52	1073.01
	25	0.672	6.28	1080.76
	50	0.704	6.05	1090.61
	100	0.745	5.82	1110.63

Table 4.2: Average properties of the simulation box (we refer to the simulation box as the system consisting of the bilayer and the water bead surrounding it) and area per lipid for different mixtures at different concentrations.

Conclusion

In this thesis, we used coarse-grained molecular dynamics to study pyrene excimer formation dynamics and lipid oxidation in model bilayers, mainly DOPC and POPC, that were simulated using the Martini force field. In all cases, the analysis was done *a posteriori* using generated data and trajectories. We developed most of the analysis tools needed, from constructing a symmetric bilayer to algorithm calculating the mean squared displacement.

Excimer formation dynamics We have presented a realistic model (within the limits of the CG procedure) to extract the kinetic coefficients of a diffusion limited process in general, and the dynamics of excimer reactions in lipids bilayers in particular. Previous statistical models considered the system as points on a lattice, undergoing jumps from site to site, or relied on theoretical mean-field treatments.

The time dependent reaction rate is derived from survival probabilities obtained from *a posteriori* generated trajectories. The systems we considered were DOPC at 283 K and POPC at 293 K. Collision statistics was determined by virtually relabelling the simulated molecules. Equivalently, we assumed that fluorescent probes behave the same as ordinary lipids in the system. However, no assumptions were made regarding the kinetic rate of the excimer formation process.

We obtained two sets of results concerning the two dimensional lateral diffusion coefficients, depending on whether interleaflet association is considered or not. The same capture radius of 0.5 nm, distance at which the probes react, was used in both cases.

Restricting the excimer formation to the same leaflet, leads to diffusion coefficient comparable to other experimental techniques. Allowing for interleaflet association reduces further the diffusion coefficient of the species. In either ways, the diffusion coefficients measured were significantly smaller than those obtained from the lattice jumps model. These values could be improved by considering multiple passage models in which the reaction probability is smaller than one: probes need to spend time inside the capture radius before forming an excimer. However, this goes against our assumption that treats pyrene excimer formation as a diffusion limited process in which the reaction is considered instantaneous. Moreover, the high probe concentration leads to a non exponential survival probability at small times, hence a time dependent reaction rate, visible as a curvature in the $1/J_M(x)$ curve. An intrinsic excimer formation time does not improve the agreement with the experimental data (titration curves).

Furthermore, relating Martini dynamics to real fluorescence experiments reveals information concerning the always debatable Martini acceleration factor, which is usually considered equal to 4. In other words the Martini dynamics is usually taken as 4 times faster than in real experiments. In this study, it has been assumed that the dynamics were sped uniformly on all timescales. However, the acceleration factor found through fitting our numerical findings to the experimental titration curve was always larger than 4. Our values range between 9 and 22, depending on temperature and interleaflet association. This is consistent with other authors who have also found acceleration factors ranging from 1 to 22 [88].

Oxidation We studied mixtures of oxidised-non oxidised DOPC and POPC. We used a hydroperoxidized model of these two lipids proposed by Guo et al. [2]. They studied fully oxidized bilayers and their mechanical properties among other. Here, we considered mixtures in which we varied the concentration of the oxidized component (3.1% , 25% and 50%). We extracted structural information concerning the systems using the pair correlation functions. As a first approximation $g(r)$ could be approximated by the Boltzmann distribution law, where particles interact through a mean field potential, relatively independent on the composition. Computing the interaction potentials reveals a reasonable agreement with that, except for the dilute systems (3.1%) for which the convergence of the correlation functions is very slow.

In addition, we calculated the mixing parameters within the framework of the virial expansion. The negative value of the coefficients leads us to assume that the two components mix well, except in one case (50:50 oxidized DOPC). Then we estimate the average area per lipid. The values obtained fall inside the two extremes (fully oxidized bilayer and normal bilayer) previously determined by Guo et al. [2]. Indeed, increasing the oxidation concentration leads to a larger area per lipid, which is in agreement with previous work.

Appendices

Chapter A1

Equations of motion for atomic systems

1 Equations of motion

Consider a system of N molecules having a set of coordinates $\boldsymbol{q_i}$ and momenta $\boldsymbol{p_i}$ for each molecule i . Adopting a condensed notation

$$\boldsymbol{q} = (\boldsymbol{q_1}, \boldsymbol{q_2}, ..., \boldsymbol{q_N}) \tag{A1.1}$$

$$\boldsymbol{p} = (\boldsymbol{p_1}, \boldsymbol{p_2}, ..., \boldsymbol{p_N}) \tag{A1.2}$$

the Lagrangian equation of motion can be written as

$$\frac{\mathrm{d}}{\mathrm{d}t}(\partial \mathcal{L}/\partial \dot{q}_k) - (\partial \mathcal{L}/\partial q_k) = 0 \tag{A1.3}$$

where the Lagrangian function $\mathcal{L}(\boldsymbol{q_k}, \boldsymbol{\dot{q}_k})$ is function of the generalised coordinates q_k and their time derivative $\dot{q}_k$. The Lagrangian can be defined by

$$\mathcal{L} = T - U \tag{A1.4}$$

where T is the kinetic energy and U is the potential energy. If we consider a system of atoms, with Cartesian coordinates $\boldsymbol{r}_i$

$$T = \sum_{i=1}^{N} \sum_{\alpha} p_{i\alpha}^2 / 2m_i \tag{A1.5}$$

where m_i is the mass of molecule i and the index α denotes the (x, y, z) component of the momentum of molecule i. The potential U contains information regarding the intermolecular interactions. And eq. A1.3 becomes

$$m_i \ddot{\boldsymbol{r}}_i = \boldsymbol{f}_i \tag{A1.6}$$

where $\boldsymbol{f}_i$ is the force on the atom i

$$\boldsymbol{f}_i = \boldsymbol{\nabla}_{\boldsymbol{r_i}} \mathcal{L} = -\boldsymbol{\nabla}_{\boldsymbol{r_i}} U \tag{A1.7}$$

The generalized momentum p_k conjugate of q_k is defined as

$$p_k = \partial \mathcal{L} / \partial q_k \tag{A1.8}$$

The Hamiltonian is defined by the equation

$$\mathcal{H}(\boldsymbol{p}, \boldsymbol{q}) = \sum_k \dot{q}_k p_k - \mathcal{L}(\boldsymbol{q}, \dot{\boldsymbol{q}}) \tag{A1.9}$$

The Hamiltonian equation of motion

$$\dot{q}_k = \partial \mathcal{H} / \partial p_k \tag{A1.10}$$

$$\dot{p}_k = -\partial \mathcal{H} / \partial q_k \tag{A1.11}$$

For Cartesian coordinates, Hamilton's equation becomes

$$\dot{\boldsymbol{r}}_{\boldsymbol{i}} = \boldsymbol{p}_{\boldsymbol{i}} / m_i \tag{A1.12}$$

$$\dot{\boldsymbol{p}}_{\boldsymbol{i}} = -\nabla_{r_i} U = \boldsymbol{f}_{\boldsymbol{i}} \tag{A1.13}$$

2 Stress

The isotropic stress is defined as $\sigma = (\sigma_{xx} + \sigma_{yy} + \sigma_{zz})/3$, where each stress component is defined as below

$$\sigma_{xx} = \frac{1}{V} \left(\sum_i^N m_i v_{i,x}^2 + \sum_{i<j} (x_{|ij|}) f_{x,|ij|} \right) \tag{A1.14}$$

and similar with x replaced by y and z. $v_{i,x}$ is the x component of the velocity along x, $x_{|ij|}$ the x component of the relative distance between i and j in the minimal image convention and $f_{x,|ij|}$ the x component of the force exerted by atom j onto atom i.

At equilibrium $\sigma = -p$, with p pressure. If $-\sigma > p$ the barostat must increase the simulation box size, if $-\sigma < p$ it must compress the system.

Chapter A2

On mixtures

1 Thermodynamic relations involving rdfs for pure fluids

All the thermodynamic quantities involving averages of observables obtained as a sum over all pairs of particles can be expressed using pair correlation functions. For a 3d fluid of N particles subject to pairwise interaction potentials $v(r)$, the internal energy reads

$$U = \frac{3NkT}{2} + \frac{1}{2}\int \mathrm{d}\mathbf{r}\, g(r)v(r) \tag{A2.1}$$

the virial equation gives the pressure

$$\frac{P}{\rho k_B T} = 1 - \frac{\rho}{6}\int \mathrm{d}\boldsymbol{r}\, g(r)rv'(r) \tag{A2.2}$$

The isothermal compressibility χ_T is itself related to the limit $q \to 0$ of the structure factor. In particular:

$$\rho k_B T \chi_T = S(q=0) = 1 + \rho \int \mathrm{d}\mathbf{r}(g(r) - 1) \tag{A2.3}$$

(A2.3) is just a special case of a linear response function of fluid density subject to a periodically modulated external field (see Section on direct correlation function below).

For a 2d fluid, eq. (A2.2) becomes

$$\frac{P}{\rho k_B T} = 1 - \frac{\rho}{4}\int \mathrm{d}\mathbf{r}\, g(r)rv'(r) \tag{A2.4}$$

eq. (A2.5)

$$U = NkT + \frac{1}{2}\int \mathrm{d}\mathbf{r}\, g(r)v(r) \tag{A2.5}$$

and (A2.3) remains unchanged.

We note that for a coarse-grained fluid, the effective potential $U(\mathbf{r}^N)$ may not adequately reduce to a sum of pair-wise interactions. As a result, equations (A2.5) - (A2.4) are ill-defined. In particular, one must define first which $v(r)$ is used in these relations. By contrast, eq. (A2.3) does not rely on pairwise decomposition.

2 A virial expansion for mixtures

Let us consider a binary mixture with configurational integral

$$Z = \frac{1}{N_1!N_2!}\int \prod_{i=1}^{N_1+N_2} \mathrm{d}\mathbf{r}_i e^{-\beta\sum_{i,j} v_{ij}(r_{ij})} \tag{A2.6}$$

where the index runs from 1 to N_1 (species 1) and N_1+1 to N_1+N_2 (species 2). At low densities, one defines $f_{ij} = e^{-\beta v_{ij}(r_{ij})} - 1$ and rewrites the configuration function

$$\begin{aligned} Z &= \frac{1}{N_1!N_2!}\int \prod_{i=1}^{N_1} \mathrm{d}\mathbf{r}_i \prod_{i<j}(1+f_{ij}) \\ &\quad + \frac{V^{N_1+N_2}}{N_1!N_2!}\int \prod \frac{\mathrm{d}\mathbf{r}_i}{V}\left(1+\sum_{i<j} f_{ij}\right) \end{aligned} \tag{A2.7}$$

which is then expanded in powers of f (Mayer cluster expansion) [103, 104]. One finds

$$\begin{aligned} \ln(Z) &= \ln\left(\frac{V^{N_1+N_2}}{N_1!N_2!}\right) + \ln\left(1 + \frac{N_1(N_1-1)}{2}\int f_{12}\frac{\mathrm{d}\mathbf{r}_1}{V}\frac{\mathrm{d}\mathbf{r}_2}{V}\right. \\ &= \left. N_1N_2\int f_{12'}\frac{\mathrm{d}\mathbf{r}_1}{V}\frac{\mathrm{d}\mathbf{r}'_2}{V} + \frac{N_2(N_2-1)}{2}\int f_{1'2'}\frac{\mathrm{d}\mathbf{r}'_1}{V}\frac{\mathrm{d}\mathbf{r}'_2}{V}\right) \end{aligned} \tag{A2.8}$$

where 1,2 designate particles of type 1 and 1',2' particles of type 2. For $N_1, N_2 \gg 1$, one has

$$\begin{aligned} \ln(Z) &= \ln\left(\frac{V^{N_1+N_2}}{N_1!N_2!}\right) + \frac{\rho_1^2}{2}\int f_{12}\mathrm{d}\mathbf{r}_1\mathrm{d}\mathbf{r}_2 \\ &\quad + \rho_1\rho_2\int f_{12'}\mathrm{d}\mathbf{r}_1\mathrm{d}\mathbf{r}'_2 + \frac{\rho_2^2}{2}\int f_{1'2'}\mathrm{d}\mathbf{r}'_1\mathrm{d}\mathbf{r}'_2 \end{aligned} \tag{A2.9}$$

The Helmholtz free-energy $-kT\ln Z$ reads

$$\begin{aligned} F &= F_{id} - k_BT\rho^2V\left\{\frac{x_1^2}{2}\int(e^{-\beta v_{12}}-1)\mathrm{d}\mathbf{r}\right. \\ &\quad \left. + x_1x_2\int(e^{-\beta v_{12'}}-1)\mathrm{d}\mathbf{r} + \frac{x_2^2}{2}\int(e^{-\beta v_{1'2'}}-1)\mathrm{d}\mathbf{r}\right\} \end{aligned} \tag{A2.10}$$

The ideal free-energy term is

$$\begin{aligned} F_{id} &= -k_B T \ln\left(\frac{V^{N_1+N_2}}{N_1!N_2!}\right) \\ &= k_B T V(\rho_1 \ln \rho_1 - \rho_1 + \rho_2 \ln \rho_2 - \rho_2) \\ &\quad + k_B T \rho^2 V(x_1 \ln x_1 + x_2 \ln x_2 - 1) \end{aligned} \tag{A2.11}$$

The virial expansion for a binary mixture gives a theory of regular solutions, where the χ coefficients are given by virial coefficients.

$$\beta F = x_1 \ln x_1 + x_2 \ln x_2 + \chi_{11}\frac{x_1^2}{2} + \chi_{22}\frac{x_2^2}{2} + \chi_{12}x_1x_2 \tag{A2.12}$$

with

$$\begin{aligned} \chi_{11} &= \rho \int (1 - e^{-\beta v^{(11)}})\mathrm{d}\mathbf{r} \\ \chi_{12} &= \rho \int (1 - e^{-\beta v^{(12)}})\mathrm{d}\mathbf{r} \\ \chi_{22} &= \rho \int (1 - e^{-\beta v^{(22)}})\mathrm{d}\mathbf{r} \end{aligned} \tag{A2.13}$$

Here $\rho = (N_1 + N_2)/V$ is the total number density, $v^{(11)}$ the pair potential acting between two molecules of type 1, $v^{(12)}$ between one molecule of type 1 and one molecule of type 2 and $v^{(22)}$ between two molecules of type 2.

At the virial expansion level, the pair correlation functions read $g^{(11)} = \exp(-\beta v^{(11)})$, $g^{(12)} = \exp(-\beta v^{(12)})$, $g^{(22)} = \exp(-\beta v^{(22)})$. In other words, the pair potentials are equivalent to the potentials of mean force $v^{(\alpha\beta)} = -k_B T \ln(g^{(\alpha\beta)})$. The first order virial expansion gives

$$\begin{aligned} \chi_{11} &= \rho \int (1 - g^{(11)})\mathrm{d}\mathbf{r} \\ &= -\rho H^{(11)} \\ \chi_{12} &= \rho \int (1 - g^{(12)})\mathrm{d}\mathbf{r} \\ &= -\rho H^{(12)} \\ \chi_{22} &= \rho \int (1 - g^{(22)})\mathrm{d}\mathbf{r} \\ &= -\rho H^{(22)} \end{aligned} \tag{A2.14}$$

A positive $\chi = \chi_{12} - (\chi_{11} + \chi_{22})/2$ shows a tendency to demix, while a negative χ means that both species tend to intersperse.

3 The direct correlation functions

Let us introduce an external energy field $\phi^{(1)}(\mathbf{r})$ coupled to particles of type 1 and $\phi^{(2)}(\mathbf{r})$ coupled to particles of type 2.

$$\begin{aligned} \hat{\rho}^{(1)} &= \sum_{i=1}^{N_1} \delta(\mathbf{r} - \mathbf{r}_i(t)) \\ \hat{\rho}^{(2)} &= \sum_{j=N_1+1}^{N_1+N_2} \delta(\mathbf{r} - \mathbf{r}_j(t)) \qquad \text{(A2.15)} \\ & \qquad \text{(A2.16)} \end{aligned}$$

are the density operators for species 1 and 2 respectively. Let $\mathcal{H}_0$ be the interaction Hamiltonian. The total Hamiltonian in the presence of external fields reads $\mathcal{H} = \mathcal{H}_0 - \int \mathrm{d}\mathbf{r}(\hat{\rho}^{(1)}\phi^{(1)} + \hat{\rho}^{(2)}\phi^{(2)})$. The $\phi^{(\alpha)}$ act like space dependent chemical potentials which spatially modulate the average density $\rho^{(a)} = \langle \hat{\rho}^{(a)} \rangle$ of each species.

The partition function can be written

$$Z = \int \mathrm{d}\mu \, e^{-\beta\mathcal{H}_0 + \beta \int \mathrm{d}\mathbf{r}(\hat{\rho}^{(1)}\phi_1 + \hat{\rho}^{(2)}\phi_2)} \qquad \text{(A2.17)}$$

Derivatives of $\ln Z$ give the average density fields

$$\frac{\delta \ln Z}{\delta \phi^{(a)}(\mathbf{r})} = \langle \beta \hat{\rho}^{(a)}(\mathbf{r}) \rangle = \beta \rho^{(a)}(\mathbf{r}) \qquad \text{(A2.18)}$$

Second functional derivatives gives the second cumulant (centered correlation functions)

$$\frac{\delta^2 \ln Z}{\delta \phi^{(a)}(\mathbf{r}) \delta \phi^{(b)}(\mathbf{r}')} = \beta^2 \langle \hat{\rho}^{(a)}(\mathbf{r}) \hat{\rho}^{(b)}(\mathbf{r}') \rangle_c \qquad \text{(A2.19)}$$

The averages are $(a \neq b)$

$$\begin{aligned} \langle \hat{\rho}^{(a)}(\mathbf{r}) \hat{\rho}^{(a)}(\mathbf{r}') \rangle_c &= \rho^{(a)} \delta(\mathbf{r} - \mathbf{r}') + (\rho^{(a)})^2 (g^{(aa)}(||\mathbf{r} - \mathbf{r}'||) - 1) \\ \langle \hat{\rho}^{(a)}(\mathbf{r}) \hat{\rho}^{(b)}(\mathbf{r}') \rangle_c &= \rho^{(a)} \rho^{(b)} (g^{(ab)}(||\mathbf{r} - \mathbf{r}'||) - 1) \qquad \text{(A2.20)} \end{aligned}$$

Denoting $A = -k_B T \ln Z$ the free-energy,

$$\frac{\delta \rho^{(a)}(\mathbf{r})}{\delta \phi^{(b)}(\mathbf{r}')} = -\frac{\delta^2 A}{\delta \phi^{(a)}(\mathbf{r}) \delta \phi^{(b)}(\mathbf{r}')} = \frac{1}{k_B T} \left[\rho^{(a)} \delta_{ab} \delta(\mathbf{r} - \mathbf{r}') + \rho^{(a)} \rho^{(b)} h^{(ab)}(\mathbf{r} - \mathbf{r}') \right] \qquad \text{(A2.21)}$$

The ideal gas case is recovered when $h^{(ab)} = 0$. To obtain the density functional, one performs a Legendre transform of A w.r.t. the density field

$$\rho^{(a)}(\mathbf{r}) = -\frac{\delta A}{\delta \phi^{(a)}(\mathbf{r})} \qquad \text{(A2.22)}$$

and therefore

$$F = A + \int \mathrm{d}\mathbf{r}\,(\phi^{(1)}\rho^{(1)} + \phi^{(2)}\rho^{(2)}) \tag{A2.23}$$

from which one deduces

$$\phi^{(a)}(\mathbf{r}) = \frac{\delta F}{\delta\rho^{(a)}(\mathbf{r})} \tag{A2.24}$$

The $\delta\phi/\delta\rho$ and $\delta\rho/\delta\phi$ are *functional inverses*:

$$\begin{aligned} \sum_c \int \mathrm{d}\mathbf{r}'' \frac{\delta\rho^{(a)}(\mathbf{r})}{\delta\phi^{(c)}(\mathbf{r}'')} \frac{\delta\phi^{(c)}(\mathbf{r}'')}{\delta\rho^{(b)}(\mathbf{r}')} &= \delta_{ab}\delta(\mathbf{r}-\mathbf{r}') \qquad \text{(A2.25)} \\ &= -\sum_c \int \mathrm{d}\mathbf{r}'' \frac{\delta^2 F}{\delta\rho^{(a)}(\mathbf{r})\delta\rho^{(c)}(\mathbf{r}'')} \frac{\delta^2 A}{\delta\phi^{(c)}(\mathbf{r}')\phi^{(b)}(\mathbf{r}')} \end{aligned}$$

On the other hand, F can be split into a ideal part and an excess part

$$\begin{aligned} F &= F_{id} + F_{exc} \\ \beta F_{id} &= \int (\rho_1 \ln\rho_1 - \rho_1 + \rho_2 \ln\rho_2 - \rho_2)\mathrm{d}\mathbf{r} \end{aligned} \tag{A2.26}$$

The direct correlation functions corresponds to the functional expansion of F_{exc} in powers of the densities $\rho^{(a)}$. In particular, the direct correlation functions of order 2 are defined by

$$c^{(ab)}(\mathbf{r}-\mathbf{r}') = -\beta \frac{\delta^2 F_{exc}}{\delta\rho^{(a)}(\mathbf{r})\delta\rho^{(b)}(\mathbf{r}')} \tag{A2.27}$$

The functional inversion relation (A2.25), together with the definitions (A2.21) of the total correlation functions and (A2.27) of the direct correlation functions gives a general Orstein-Zernike relation for the mixture. For a homogeneous binary mixture

$$\begin{aligned} h^{(11)}(\mathbf{r}) &= c^{(11)}(\mathbf{r}) + \int \left[c^{(11)}(\mathbf{r}')\rho^{(1)}h^{(11)}(\mathbf{r}-\mathbf{r}') + c^{(12)}(\mathbf{r}')\rho^{(2)}h^{(21)}(\mathbf{r}-\mathbf{r}')\right]\mathrm{d}\mathbf{r}' \\ h^{(12)}(\mathbf{r}) &= c^{(12)}(\mathbf{r}) + \int \left[c^{(11)}(\mathbf{r}')\rho^{(1)}h^{(12)}(\mathbf{r}-\mathbf{r}') + c^{(12)}(\mathbf{r}')\rho^{(2)}h^{(22)}(\mathbf{r}-\mathbf{r}')\right]\mathrm{d}\mathbf{r}' \\ h^{(22)}(\mathbf{r}) &= c^{(22)}(\mathbf{r}) + \int \left[c^{(21)}(\mathbf{r}')\rho^{(1)}h^{(12)}(\mathbf{r}-\mathbf{r}') + c^{(22)}(\mathbf{r}')\rho^{(2)}h^{(22)}(\mathbf{r}-\mathbf{r}')\right]\mathrm{d}\mathbf{r}' \end{aligned} \tag{A2.28}$$

Eq. (A2.29) makes it possible in practice to compute numerically the direct correlation functions knowing the pair distribution functions.

A theory of regular solutions can be formally recovered by expanding the free-energy F up to second order in the fields ρs. At this order (equivalent to a

Ramakrishnan-Yussouf approximation [105]).

$$\begin{aligned}\beta F \simeq & \int(\rho_1 \ln\rho_1 - \rho_1 + \rho_2\ln\rho_2 - \rho_2)\mathrm{d}\mathbf{r} \\ & -\frac{1}{2}\int \mathrm{d}\mathbf{r}\mathrm{d}\mathbf{r}'\, c^{(11)}(\mathbf{r}-\mathbf{r}')\rho^{(1)}(\mathbf{r})\rho^{(1)}(\mathbf{r}') \\ & -\frac{1}{2}\int \mathrm{d}\mathbf{r}\mathrm{d}\mathbf{r}'\, c^{(22)}(\mathbf{r}-\mathbf{r}')\rho^{(2)}(\mathbf{r})\rho^{(2)}(\mathbf{r}') \\ & -\int \mathrm{d}\mathbf{r}\mathrm{d}\mathbf{r}'\, c^{(12)}(\mathbf{r}-\mathbf{r}')\rho^{(1)}(\mathbf{r})\rho^{(2)}(\mathbf{r}') \end{aligned} \qquad (A2.29)$$

The stability of the free-energy with respect to fluctuations of density requires that, in Fourier space the matrix

$$\begin{pmatrix} \frac{1}{\rho^{(1)}} - \tilde{c}^{(11)}(q) & -\tilde{c}^{(12)}(q) \\ -\tilde{c}^{(12)}(q) & \frac{1}{\rho^{(2)}} - \tilde{c}^{(22)}(q) \end{pmatrix} \qquad (A2.30)$$

is positive definite. Macroscopic binary phase separation is associated with the $q \to 0$ limit of the above matrix. To this extent, the χ_{ab} parameters of the regular solutions theory are related to the Fourier coefficients $\tilde{c}^{(ab)}(q=0)$. These coefficients can be in turn related to the integrals $\int h^{(ab)}\mathrm{d}\mathbf{r} = \tilde{h}^{(ab)}(q=0)$.

In particular, defining

$$\hat{C} = \begin{pmatrix} c^{(11)}(q=0) & c^{(12)}(q=0) \\ c^{(12)}(q=0) & c^{(22)}(q=0) \end{pmatrix}, \qquad (A2.31)$$

$$\hat{H} = \begin{pmatrix} h^{(11)}(q=0) & h^{(12)}(q=0) \\ h^{(12)}(q=0) & h^{(22)}(q=0) \end{pmatrix} \qquad (A2.32)$$

and

$$\hat{R} = \begin{pmatrix} \rho^{(1)} & 0 \\ 0 & \rho^{(2)} \end{pmatrix}, \qquad (A2.33)$$

one obtains the Ornstein-Zernike relations in Fourier space and matrix form:

$$\hat{C}^{-1} = \hat{R} + \hat{H}^{-1} \qquad (A2.34)$$

More precisely, the free-energy of the mixture (A2.29) is now the sum of two contributions $F_{id} + F_{exc}$ with

$$\frac{\beta F_{id}}{V} = \rho\ln\rho - \rho + \rho(x_1\ln x_1 + x_2 \ln x_2) \qquad (A2.35)$$

$$\frac{\beta F_{exc}}{V} = -\frac{\rho}{2}\left(\rho\tilde{c}^{(11)}(0)x_1^2 + \rho\tilde{c}^{(22)}(0)x_2^2 + 2\rho\tilde{c}^{(12)}(0)x_1x_2\right) \qquad (A2.36)$$

One therefore recognizes the χ_{ab} interaction parameters as

$$\begin{aligned}\chi_{11} &= -\rho\tilde{c}^{(11)}(0)\\ \chi_{12} &= -\rho\tilde{c}^{(12)}(0)\\ \chi_{22} &= -\rho\tilde{c}^{(22)}(0)\end{aligned}\tag{A2.37}$$

Meanwhile, a direct inversion of (A2.34) leads to

$$\rho\hat{C} = \frac{1}{1 + x_1 H^{(11)} + x_2 H^{(22)} + x_1 x_2 \mathcal{D}}\begin{pmatrix} H^{(11)} + x_2\mathcal{D} & H^{(12)} \\ H^{(12)} & H^{(22)} + x_1\mathcal{D}\end{pmatrix}\tag{A2.38}$$

where $H^{(11)} = \rho\tilde{h}^{(11)}(0) = \rho\int \mathrm{d}\mathbf{r}(g^{(11)}(r)-1)$, $H^{(12)} = \rho\tilde{h}^{(12)}(0) = \rho\int \mathrm{d}\mathbf{r}(g^{(12)}(r)-1)$, $H^{(22)} = \rho\tilde{h}^{(22)}(0) = \rho\int \mathrm{d}\mathbf{r}(g^{(22)}(r)-1)$, $\mathcal{D} = H^{(11)}H^{(22)} - (H^{(12)})^2$ and $\rho = (N_1 + N_2)/V$.

4 Numerical determination of the rdf

In addition to the **g_rdf** command, we built our own numerical tools that allowed us to analyze the structure of the model bilayer after the simulation was completed.

By definition, the pair correlation function is the number of particles at a distance r from a reference particle, normalized by the number of particles at the same distance in an ideal gas with the same density [106].

$$n_{ideal} = \frac{4\pi\rho}{3}[\,(r+\delta r)^3 - r^3\,]\tag{A2.39}$$

For two dimensional systems eq.(A2.39) becomes

$$n_{ideal} = \pi\rho\,[\,(r+\delta r)^2 - r^2\,]\tag{A2.40}$$

Keeping the definition of $g(r)$ in mind, the pair correlation function reads

$$g(r) = n/n_{ideal}\tag{A2.41}$$

In practice, n is calculated from the trajectory files generated by the molecular dynamics by sorting pairs into an histogram. The first step is to calculate the separations r_{ij} between all pairs according to the nearest image convention. The second step is to sort the minimum image separations into bins b that have a width δr. Therefore, if the separation of pair ij is r_{ij}, the particle counter will increase in the respective bin that extends from r to $r+\delta r$ such that $r_{ij} \in [r, r+\delta r]$.

Chapter A3

Simulation-details

1 Dynamical quantities

The dynamical CG-DOPC consists of 14 beads, out of which chain terminal group correspond to beads 12 to 14. Let us denote by $\vec{r}_{i,\alpha}(t) = (x_{i,\alpha}(t), y_{i,\alpha}(t), z_{i,\alpha}(t))$ the trajectory of a bead, i being the index of the molecule and $1 < \alpha < 14$ the index of the bead. Center of mass (CM) and and terminal subgroup (TS) positions are defined as

$$\vec{r}_{i,CM} = \frac{1}{14} \sum_{\alpha=1}^{14} \vec{r}_{i,\alpha}(t) \tag{A3.1}$$

$$\vec{r}_{i,TS} = \frac{1}{3} \sum_{\alpha=12}^{14} \vec{r}_{i,\alpha}(t) \tag{A3.2}$$

Mean square displacements are obtained from unwrapped trajectories

$$g_{CM}(t) = \frac{1}{N_t} \langle [\, x_{i,CM}(t) - x_{i,CM}(0)\,]^2 \rangle \tag{A3.3}$$

$$g_{TS}(t) = \frac{1}{N_t} \langle [\, x_{i,TS}(t) - x_{i,TS}(0)\,]^2 \rangle \tag{A3.4}$$

Collisions occurs when two terminal subgroups are found within an interaction sphere of radius ρ_c. In other words, two groups are within reaction distance if

$$\Delta(\vec{r}_{i,TS}(t), \vec{r}_{j,TS}(t)) \leq \rho_c^2 \tag{A3.5}$$

where Δ stands for the Euclidean distance between groups i and j in the minimal image distance convention.

2 Numerical integration of the monomer emission intensity

Numerical sampling of the survival functions, such as outlined in eq. (13) in chapter 3, provides a function $P_c(t)$ sampled at equal times up to a cutoff value. The behaviour at longer times is, within good approximation exponential.

The long time behaviour does not dominate the following quadrature for two reasons

$$J_M = \frac{1}{\tau_M} \int_0^\infty \mathrm{d}t \, P_c(t) \, \exp\left(-\frac{t}{\tau_M}\right) \tag{A3.6}$$

First, the integration is naturally cutoff by the spontaneous monomer decay rate $\exp(t/\tau_M)$ and second, increasing the probe concentration x has the effect of putting more weight on the short time regimes, making the long time regime irrelevant as far as computing J_E and J_M is concerned.

Therefore, a trapezoid integration rule was found to give satisfying accurate results. Such an integration is required for each value of the acceleration factor, and each choice of for x. The acceleration factor f was determined by trial and errors, until best visual fit to the titration curves in Figs. 9, 10 and 11 in the Manuscript.

3 Simulation details for the excimer problem

Simulations were performed with GROMACS 4.6 on the High Performance Cluster (HPC) of the university of Strasbourg. We have simulated symmetric patches of bilayers made of respectively 512 DOPC and 512 POPC Martini coarse-grained molecules. Constant volume simulations (for a pressure close to 1 bar) and *v-rescale* thermostat were used. Four trajectories of 5×10^6 steps were used for each system : DOPC at 283 K and POPC at 293 K. The solvent consisted of 3072 CG-water molecules which corresponds to a 1:6 scaling(6 water molecules to 1 lipid).

The preparation scheme consists in four steps: 1/ energy minimization/relaxation, 2/ thermalization/equilibration, 3/ rescaling the volume of the system, 4/ thermalization/equilibration.

The first step is a non-dynamical run, where no kinetic energy is given, *i.e* temperature is set to zero. This minimization is needed before starting MD runs to relax large stresses consecutive to changing the identity or number of beads present in the system. Starting from a stressed configuration commonly leads to simulation crashes in spite of the presence of a regulating thermostat.

The minimization step results in a configuration with a minimum potential energy (inherent structure) close to the starting configuration. Then we perform a first equilibration run for another 30 ns (10^6 steps). During equilibration, we allow the bilayer to evolve while coupled to thermostats and, in this case, barostats. We used the Nose-Hoover thermostat in this step. For the barostat, we used a semi-isotropic *Parrinello-Rahman* pressure coupling with transverse z direction normal to the bilayer [83].

During the first equilibration step, the volume of the system was allowed to fluctuate. We compute the average volume using GROMACS built in function **g_energy**. We rescale the simulation box to this volume, in an attempt to reduce pressure fluctuation when running simulations in the NVT ensemble. We repeat step two starting from the new configuration with the modified volume.

Once the system is equilibrated, we performed a total run of 450 ns, with an integration step of 30 fs. We are now in the NVT ensemble where the temperature was fixed to 283K for the DOPC bilayer and 293 for the POPC bilayer using the *v-rescale* heat bath and no pressure coupling was used. This normally ensures that the bilayer is at constant volume.

Trajectory frames are collected every 200 steps (6 ps) for the collision analysis. This frame frequency is significantly higher than what is normally required when computing membrane equilibrium properties. The simulation time was found to be sufficient, given the spontaneous monomer deexcitation dynamics which restricts excimer formation to the initial part of $P_c(t)$. The same simulation scheme was applied to POPC bilayers.

A patch of 2048 DOPC lipids was also simulated to provide the size-scaling assumption comparison in Fig. 7.

4 Simulation details for the lipid mixtures problem

Systems of 512 lipids and 3072 solvent beads were also used. The composition are 8 oxidized and 248 normal lipids per leaflet (3.1% composition), 64 oxidized and 192 normal lipids per leaflet (25% composition), 128 oxidized and 128 normal lipids per leaflet (50% composition). Simulations are carried on in the NPT ensemble (v-rescale thermostat and Parrinello-Rahman barostat).

Diluted systems are slow to converge: our data include 250×10^6 steps. The other systems are less demanding.

List of Figures

1 La probabilité de survie du dérivé pyrène dans une bicouche de DOPC à 10°. 4

2 Axe horizontal: concentration x, axe vertical $1/J_M$. Émission normalisée des groupes pyrènes dans les bicouches DOPC et POPC, mesurées à 10°C et 20°C respectivement. Le paramètre τ_M est choisi pour donner le meilleur fit des courbes de titration expérimentales représentées par les carrés □. 5

3 Fonction de corrélation de paires de DOPC:DHP-DOPC (b,d) et POPC:HP-POPC (a,c) pour une concentration de 25% (a,b) and 3.1% (c,d). 7

4 Aire moyen par lipide pour un mélange DOPC:DHP-DOPC et POPC:HP-POPC pour différentes concentrations d' oxydation. 8

5 Le potentiel d'interaction de paires de DOPC:DHP-DOPC et POPC:HP-POPC pour une concentration d'oxydation de 25%. 9

1.1 Highly schematic, internal view of an eukaryote cell, characterized by a membrane-bound nucleus. 12

1.2 Fluid mosaic model in which integral proteins are inserted into a fluid structure pf phospholipids. Peripheral proteins do not react with the hydrophobic part of lipids, instead they are bound to the membrane by protein-protein interaction. 14

1.3 Schematic representation of phosphatidylcholine representing the hydrophilic and hydrophobic part. The kink results from a double bond in the carbon chain. 15

1.4 Chemical structure of two phospholipids $1,2-dioleoyl-sn-glycero-3-phosphocholine$, DOPC and $1-palmitoyl-2-oleoyl-sn-glycero-3-phosphocholine$, POPC. One presents a mono saturation (POPC) while the other have both tails unsaturated (DOPC). 16

1.5 Chemical structure of cholesterol. 17

1.6 Interaction between cholesterol and phospholipids in a monolayer. . . 18

1.7 Interactive energy (attractive, repulsive and total) as a function of mean area per molecule a. Optimal headgroup area a_0 is obtained when the total interaction energy is minimized ($a = a_0$). 19
1.8 Packing arrangements of lipid molecules in an aqueous environment. Lipid molecules spontaneously form one or other of these structures in water, depending on their shape (from [29]). 20
1.9 Scheme illustrating different phases of a lipid bilayer in an aqueous medium as a function of temperature. 21
1.10 Surface pressure vs area isotherms of a Langmuir monolayer. The monolayer exhibits states transition from gaseous state, to liquid expanded (LE), liquid condensed (LC) and finally solid state upon compression. 22
1.11 Langmuir trough used to compress molecules on the surface of a subphase. 22
1.12 Langmuir-Blodgett deposition. 24
1.13 Schematic view of a spherical vesicle two lipid thick (liposomes), a micelle and lipid bilayer. 25
1.14 A scattering experiment setup. In the *Fraunhofer approximation*, the incident beam and the beam reaching the detector are considered a plane wave due to the fact that the distances between the source-sample and sample-detector are significantly larger than the size of the sample. 26
1.15 Phase difference between a beam scattered at the origin A and a beam at a position $\mathbf{r}$. 27
1.16 Plot of the dispersion relation on a double logarithmic scale. The energy-wavelength plot for neutron, electron and photon helps determining the most appropriate investigative method for the system in hand. 29
1.17 The nuclear spin energy levels of a spin 1/2 nucleus in the presence of a magnetic field. 29
1.18 Illustration of the pulse-field gradient method. Nuclei diffusing in the presence of a balanced gradient pair. The two gradients are separated by a diffusion time interval δ and are very short ($\delta \ll \tau$). A diffusion gradient changes the phase of a spin depending on its position. The result is two signals; the signal obtained without any diffusion gradients, and the signal attenuated due to phase dispersion caused by the diffusion gradient pair. 31
1.19 Perrin-Jablonski diagram illustrating the possible de-excitation processes of a molecule with no surrounding. Figure from [59]. 32
1.20 Illustration of the integral overlap between the emission spectrum of the donor and the absorption of the acceptor. Figure from [59]. . . . 33

1.21 Data collecting during a FRAP experiment. The fluorescence intensity is uniformly distributed (1). Then photobleaching occurs (2), diminishing the fluorescent signal. Over time, the amount of fluorescence in the photobleached area increases as unbleached molecules diffuse into this area (3).Eventually uniform intensity is restored (4). The diffusion coefficient is determined by the slope of the curve (3). The steeper the curve, the faster the recovery and therefore, the more mobile the molecules. 35
1.22 Individual lipid movement in a bilayer, chain conformational move, rotation along the lipid axis, protrusion, lateral diffusion and flip-flop [67]. 37
1.23 Hierarchy of the lipid motions in a bilayer, from the fastest (chain conformational transition) to the slowest (transverse diffusion). 38

2.1 The general scheme of a discrete MD simulation. (a) predict the positions, velocities, accelerations etc., at a time t + δt, using the current values of these quantities; (b) evaluate the forces, and hence accelerations, from the new positions; (c) calculate any variables of interest, such as the energy, virial, order parameters, ready for the accumulation of time averages, before returning to (a) for the next step. 42
2.2 Martini interaction matrix. Level of interaction indicates the well depth in the Lennard-Jones potential: : O, ϵ = 5.6 kJ/mol; I,ϵ = 5.0 kJ/mol; II, ϵ =4.5 kJ/mol; III, ϵ = 4 kJ/mol ; IV, ϵ = 3.5 kJ/mol; V; ϵ = 3.1 kJ/mol; VI, ϵ = 2.7 kJ/mol; VII, ϵ = 2.3 kJ/mol; VIII, ϵ = 2.0 kJ/mol; IX, ϵ = 2.0 kJ/mol. The Lennard-Jones parameter, σ = 0.47 nm for all interacion levels except level IX for which σ = 0.62 nm. (adapted form [86]). 47
2.3 Mapping between the chemical structure and the coarse grained model for DPPC. The coarse grained bead types which determine their relative hydrophilicity are indicated (from [86]). 48

3.1 Excimer formation reaction. 55
3.2 Energy gap between the first excited state and ground state for an excited monomer (left) and an excited excimer (right). Because $\nu_M \geq \nu_E$ the monomer fluorescence emission band occurs at shorter wavelengths than that of the monomer. 56
3.3 Competition between monomer and excimer deexcitation in a diffusion controlled reaction. 57
3.4 Fluorescence spectra of pyrene derivatives for different concentrations varying from G = 10^{-4} mol.L^{-1} to A= 10^{-2} mol.L^{-1}(adapted form [90]). 58

3.5 Presentation of intramolecular probes (left) and intermolecular probes (right) attached to phospholipids. The probes are represented by red cubes. Intramolecular probes are attached to the same lipid but on a different carbon chain while intermolecular probes are attached on a different lipid. In both cases, the reaction occurs when the distance separating the probes is smaller than a critical reaction radius. 59
3.6 Phospholipid analogue with a pyrene group at the end of a 10 carbon chain 61
3.7 Mean squared displacement for DOPC and POPC bilayers at 283k and 293k respectivelly. The MSD was calculated using the GROMACS generated trajectories. The slope of the curves yields the "*numerical*" lateral diffusion coefficient D_{CG} equal to $26\,\mu m^2 s^{-1}$ in the case of DOPC bilayers and $36\,\mu m^2 s^{-1}$ for POPC bilayers. 63

4.1 Examples of pair correlation functions. (a) is $g(r)$ for a *VDW gas*, showing a hard sphere repulsion in the beginning and a uniform distribution otherwise. The $g(r)$ of a *Lennard-Jones liquid* (d), and of *hard spheres* (b). (c) shows the pair correlation for solids which have long range order. 91
4.2 Schematic representation of the oxidised lipid molecules HP-POPC and DHP-DOPC based on MARTINI coarse-grained models for POPC and DOPC phospholipids respectively (adapted from [2]). 94
4.3 Top view of a POPC:HP-POPC bilayer for an oxidation concentration of 50% (cyan POPC, orange POPC). 96
4.4 Side view of a POPC:HP-POPC bilayer for an oxidation concentration of 50% (cyan POPC, orange POPC, violet water, red peroxide side groups). . 97
4.5 The pair correlation function of POPC:HP-POPC bilayers for an oxidation concentration of 50%. 97
4.6 The pair correlation function of DOPC:DHP-DOPC bilayers for an oxidation concentration of 50% 98
4.7 The pair correlation function of POPC:HP-POPC (a,c) and DOPC:DHP-DOPC (b,d) bilayers for an oxidation concentration of 25% (a,b) and 3.1% (c,d). 99
4.8 The pair interaction potential of DOPC:DHP-DOPC and POPC:HP-POPC bilayers for an oxidation concentration of 25% 100
4.9 The pair interaction potential of DOPC:DHP-DOPC (left) and POPC:HP-POPC (right) bilayers for different concentrations. Subscripts refer to the species; 1 indicates the normal phospholipid while 2 indicates the hydroperoxidized lipid. 101
4.10 Average area per lipid for DOPC:DHP-DOPC and POPC:HP-POPC bilayers for various oxidation concentrations. 103

List of Tables

1 Coefficient de diffusion et facteur d'accélération du pyrène dans les bicouches de DOPC et POPC à 10° et 20° respectivement, pour un seul feuillet (*) et quand l'association entre feuillets est autorisée. . . 6
2 Propriétés moyennes de la boite de simulation et aire par lipide pour différents mélanges à différentes concentrations. 7
3 Paramètres de mélange pour des bicouches DOPC:DHP-DOPC and POPC:HP-POPC. $\chi \leq 0$ indique un système ayant tendance à ce mélanger. Alors qu' une valeur de χ positive suggère la séparation des composants. 8

2.1 Details of the DOPC CG molecule. The force constant K_{angle} is equal to 25 kJ mol^{-1} with an equilibrium bond angle $\theta = 180\,\text{deg}$ for aliphatic chains. The force constant for the angles involving the cis double bond is set to $K_{angle} = 45$ kJ mol^{-1}. The equilibrium angle remains at $\theta = 120\,\text{deg}$.Bonded interactions were not presented here but they remain the same between different interaction sites, with an equilibrium distance $R_{bond} = \sigma = 0.47$ nm and a force constant of $K_{bond} = 1250$ kJ mol^{-1} nm^{-2}. 50

4.1 Mixing parameters for DOPC:DHP-DOPC and POPC:HP-POPC bilayers. The χ parameters were determined using Eq. (A2.14). $\chi \leq 0$ indicates that the mixture is prone to mixing. In contrast, a positive χ suggests separation. 102
4.2 Average properties of the simulation box and area per lipid for different mixtures at different concentrations. 104

Bibliography

[1] F. Dumas, M.M. Sperotto, M.C. Lebrun, J.F. Tocanne, and O.G. Mouritsen. Molecular sorting of lipids by bacteriorhodopsin in dilauroylphosphatidylcholine/distearoylphosphatidylcholine lipid bilayers. *Biophysical Journal*, 73(4):1940 – 1953, 1997.

[2] Y. Guo, V. Baulin, and F. Thalmann. Peroxidised phospholipid bilayers: insight from coarse-grained molecular dynamics simulations. Submitted to *Soft Matter*.

[3] Marian von Smoluchowski. Versuch einer mathematischen theorie der koagulationskinetik kolloider lösungen. *Zeitschrift fuer physikalische Chemie*, 92:129–168, 1917.

[4] David G. Ackerman, Frederick A. Heberle, and Gerald W. Feigenson. Limited perturbation of a dppc bilayer by fluorescent lipid probes: A molecular dynamics study. *The Journal of Physical Chemistry B*, 117(17):4844–4852, 2013.

[5] Siewert J. Marrink, Alex H. de Vries, and Alan E. Mark. Coarse grained model for semiquantitative lipid simulations. *Journal of Physical Chemistry B*, 108:750–760, 2004.

[6] M. Sassaroli, M. Vauhkonen, D. Perry, and J. Eisinger. Lateral diffusivity of lipid analogue excimeric probes in dimyristoylphosphatidylcholine bilayers. *Biophysical Journal*, 57(2):281 – 290, 1990.

[7] M. Vauhkonen, M. Sassaroli, P. Somerharju, and J. Eisinger. Dipyrenylphosphatidylcholines as membrane fluidity probes. relationship between intramolecular and intermolecular excimer formation rates. *Biophysical Journal*, 57(2):291 – 300, 1990.

[8] Michael H. Brodnitz. Autoxidation of saturated fatty acids. a review. *Journal of Agricultural and Food Chemistry*, 16(6):994–999, 1968.

[9] Georges Weber, Thierry Charitat, Mauricio S. Baptista, Adjaci F. Uchoa, Christiane Pavani, Helena C. Junqueira, Yachong Guo, Vladimir A. Baulin, Rosangela Itri, Carlos M. Marques, and Andre P. Schroder. Lipid oxidation induces structural changes in biomimetic membranes. *Soft Matter*, 10:4241–4247, 2014.

[10] Deepti Pradhan, Marybeth Weiser, Katherine Lumley-Sapanski, David Frazier, Susan Kemper, Patrick Williamson, and Robert A Schlegel. Peroxidation-induced perturbations of erythrocyte lipid organization. *Biochimica et Biophysica Acta (BBA)-Biomembranes*, 1023(3):398–404, 1990.

[11] Karen Sabatini, Juha-Pekka Mattila, Francesco M Megli, and Paavo KJ Kinnunen. Characterization of two oxidatively modified phospholipids in mixed monolayers with dppc. *Biophysical journal*, 90(12):4488–4499, 2006.

[12] Christiaan Sybesma. *Biophysics: an introduction*. Springer Science & Business Media, 2012.

[13] LB Leverett, JD Hellums, CP Alfrey, and EC Lynch. Red blood cell damage by shear stress. *Biophysical journal*, 12(3):257, 1972.

[14] Ole G. Mouritsen. *Life-as a matter of fat: the emerging science of lipidomics*. Springer, 2005.

[15] Irving Langmuir. The constitution and fundamental properties of solids and liquids. ii. liquids. 1. *Journal of the American Chemical Society*, 39(9):1848–1906, 1917.

[16] Evert Gorter and FJEM Grendel. On bimolecular layers of lipoids on the chromocytes of the blood. *The Journal of experimental medicine*, 41(4):439–443, 1925.

[17] W.M Sperry. Lipid excretion. iii. further studies of the quantitative relations of fecal lipids. *Journal of Biological Chemistry*, 68:357–383, 1926.

[18] James Frederic Danielli and Hugh Davson. A contribution to the theory of permeability of thin films. *Journal of cellular and comparative physiology*, 5(4):495–508, 1935.

[19] Mark S Bretscher. Asymmetrical lipid bilayer structure for biological membranes. *Nature*, 236(61):11–12, 1972.

[20] S.J. Singer and G.L. Nicolson. The fluid mosaic model of the structure of cell membranes. *Science*, 175:720–731, 1972.

[21] Kai Simons, Elina Ikonen, et al. Functional rafts in cell membranes. *Nature*, 387(6633):569–572, 1997.

[22] Alan D McNaught and Alan D McNaught. *Compendium of chemical terminology*, volume 1669. Blackwell Science Oxford, 1997.

[23] M Gobley. Recherches chimiques sur le jaune d'œuf. 2. mémoire. *J. Pharm. Chim.(Paris)*, 12(1), 1847.

[24] Nicolas Théodore Gobley. *Recherches chimiques sur les œufs de carpe*. E. Martinet, 1850.

[25] Horia I Petrache, Steven W Dodd, and Michael F Brown. Area per lipid and acyl length distributions in fluid phosphatidylcholines determined by 2 h nmr spectroscopy. *Biophysical journal*, 79(6):3172–3192, 2000.

[26] Joseph L Gay-Lussac. imprimée dans le deuxième volume des annales de chimie et de physique. *Ann. Chim. Phys., Ser*, 2(7):339–372, 1817.

[27] Robert E Olson. Discovery of the lipoproteins, their role in fat transport and their significance as risk factors. *The Journal of nutrition*, 128(2):439S–443S, 1998.

[28] Henna Ohvo-Rekilä, Bodil Ramstedt, Petra Leppimäki, and J Peter Slotte. Cholesterol interactions with phospholipids in membranes. *Progress in lipid research*, 41(1):66–97, 2002.

[29] Deborah Leckband and Jacob Israelachvili. Intermolecular forces in biology. *Quarterly Review of Biophysics*, 34(02):105–267, 2001.

[30] Charles Tanford. *The Hydrophobic Effect: Formation of Micelles and Biological Membranes 2d Ed.* J. Wiley., 1980.

[31] Barbara A Lewis and Donald M Engelman. Lipid bilayer thickness varies linearly with acyl chain length in fluid phosphatidylcholine vesicles. *Journal of molecular biology*, 166(2):211–217, 1983.

[32] Jacob N Israelachvili, D John Mitchell, and Barry W Ninham. Theory of self-assembly of hydrocarbon amphiphiles into micelles and bilayers. *Journal of the Chemical Society, Faraday Transactions 2: Molecular and Chemical Physics*, 72:1525–1568, 1976.

[33] A Tardieu, Vittorio Luzzati, and FC Reman. Structure and polymorphism of the hydrocarbon chains of lipids: a study of lecithin-water phases. *Journal of molecular biology*, 75(4):711–733, 1973.

[34] Krister Holmberg, Dinesh Ochhavlal Shah, and Milan J Schwuger. *Handbook of applied surface and colloid chemistry*, volume 1. Wiley New York, 2002.

[35] Marc Eeman and Magali Deleu. From biological membranes to biomimetic model membranes. *Base*, 2010.

[36] Yves F Dufrêne, William R Barger, John-Bruce D Green, and Gil U Lee. Nanometer-scale surface properties of mixed phospholipid monolayers and bilayers. *Langmuir*, 13(18):4779–4784, 1997.

[37] Hilde A Rinia, Rudy A Demel, Jan PJM van der Eerden, and Ben de Kruijff. Blistering of langmuir-blodgett bilayers containing anionic phospholipids as observed by atomic force microscopy. *Biophysical journal*, 77(3):1683–1693, 1999.

[38] F Jähnig. What is the surface tension of a lipid bilayer membrane? *Biophysical journal*, 71(3):1348–1349, 1996.

[39] V Vie, N Van Mau, E Lesniewska, JP Goudonnet, F Heitz, and C Le Grimellec. Distribution of ganglioside gm1 between two-component, two-phase phosphatidylcholine monolayers. *Langmuir*, 14(16):4574–4583, 1998.

[40] Adrienne A Brian and Harden M McConnell. Allogeneic stimulation of cytotoxic t cells by supported planar membranes. *Proceedings of the National Academy of Sciences*, 81(19):6159–6163, 1984.

[41] Roger G Horn. Direct measurement of the force between two lipid bilayers and observation of their fusion. *Biochimica et Biophysica Acta (BBA)-Biomembranes*, 778(1):224–228, 1984.

[42] Jana Jass, Torbjörn Tjärnhage, and Gertrud Puu. From liposomes to supported, planar bilayer structures on hydrophilic and hydrophobic surfaces: an atomic force microscopy study. *Biophysical journal*, 79(6):3153–3163, 2000.

[43] Ralf P Richter and Alain R Brisson. Following the formation of supported lipid bilayers on mica: a study combining afm, qcm-d, and ellipsometry. *Biophysical journal*, 88(5):3422–3433, 2005.

[44] Magdalena Przybylo, Jan Sỳkora, Jana Humpolíčková, Aleš Benda, Anna Zan, and Martin Hof. Lipid diffusion in giant unilamellar vesicles is more than 2 times faster than in supported phospholipid bilayers under identical conditions. *Langmuir*, 22(22):9096–9099, 2006.

[45] Linda Malaquin, Thierry Charitat, and Jean Daillant. Supported bilayers: Combined specular and diffuse x-ray scattering. *The European Physical Journal E: Soft Matter and Biological Physics*, 31(3):285–301, 2010.

[46] David H Murray, Lukas K Tamm, and Volker Kiessling. Supported double membranes. *Journal of structural biology*, 168(1):183–189, 2009.

[47] Erich Sackmann. Supported membranes: scientific and practical applications. *Science*, 271(5245):43–48, 1996.

[48] John P Reeves and Robert M Dowben. Formation and properties of thin-walled phospholipid vesicles. *Journal of cellular physiology*, 73(1):49–60, 1969.

[49] Uri Pick. Liposomes with a large trapping capacity prepared by freezing and thawing of sonicated phospholipid mixtures. *Archives of biochemistry and biophysics*, 212(1):186–194, 1981.

[50] MJ Hope, MB Bally, G Webb, and PR Cullis. Production of large unilamellar vesicles by a rapid extrusion procedure. characterization of size distribution, trapped volume and ability to maintain a membrane potential. *Biochimica et Biophysica Acta (BBA)-Biomembranes*, 812(1):55–65, 1985.

[51] Miglena I Angelova and Dimiter S Dimitrov. Liposome electroformation. *Faraday discussions of the Chemical Society*, 81:303–311, 1986.

[52] Theresa M Allen and Pieter R Cullis. Drug delivery systems: entering the mainstream. *Science*, 303(5665):1818–1822, 2004.

[53] W. Rawicz, K.C. Olbrich, T. McIntosh, D. Needham, and E. Evans. Effect of chain length and unsaturation on elasticity of lipid bilayers. *Biophysical Journal*, 79(1):328 – 339, 2000.

[54] John F Nagle and Stephanie Tristram-Nagle. Structure of lipid bilayers. *Biochimica et Biophysica Acta (BBA)-Reviews on Biomembranes*, 1469(3):159–195, 2000.

[55] Sebastian Busch, Luis Carlos Pardo, Christoph Smuda, and Tobias Unruh. The picosecond dynamics of the phospholipid dimyristoylphosphatidylcholine in mono- and bilayers. *Soft Matter*, 8:3576–3585, 2012.

[56] Göran Lindblom and Greger Orädd. Nmr studies of translational diffusion in lyotropic liquid crystals and lipid membranes. *Progress in Nuclear Magnetic Resonance Spectroscopy*, 26:483–515, 1994.

[57] C Dolainsky, P Karakatsanis, and TM Bayerl. Lipid domains as obstacles for lateral diffusion in supported bilayers probed at different time and length scales by two-dimensional exchange and field gradient solid state nmr. *Physical Review E*, 55(4):4512, 1997.

[58] EO Stejskal and JE Tanner. Spin diffusion measurements: spin echoes in the presence of a time-dependent field gradient. *The journal of chemical physics*, 42(1):288–292, 1965.

[59] Bernard Valeur. *Molecular Fluorescence: Principle and Applications*. Wiley-VCH, 2002.

[60] Luís MS Loura and Manuel Prieto. Fluorescence resonance energy transfer to characterize cholesterol-induced domains. In *Methods in Membrane Lipids*, pages 489–501. Springer, 2007.

[61] JCG Blonk, A Don, H van Aalst, and JJ Birmingham. Fluorescence photobleaching recovery in the confocal scanning light microscope. *Journal of Microscopy*, 169(3):363–374, 1993.

[62] Ulrich Kubitscheck, Peter Wedekind, and Reiner Peters. Lateral diffusion measurement at high spatial resolution by scanning microphotolysis in a confocal microscope. *Biophysical journal*, 67(3):948, 1994.

[63] Adam D Douglass and Ronald D Vale. Single-molecule microscopy reveals plasma membrane microdomains created by protein-protein networks that exclude or trap signaling molecules in t cells. *Cell*, 121(6):937–950, 2005.

[64] Norman Bobroff. Position measurement with a resolution and noise-limited instrument. *Review of Scientific Instruments*, 57(6):1152–1157, 1986.

[65] Michael J Saxton and Ken Jacobson. Single-particle tracking: applications to membrane dynamics. *Annual review of biophysics and biomolecular structure*, 26(1):373–399, 1997.

[66] GJ Schütz, H Schindler, and Th Schmidt. Single-molecule microscopy on model membranes reveals anomalous diffusion. *Biophysical journal*, 73(2):1073, 1997.

[67] P. Bongrand. *Handbook of Biological Physics*, chapter 16 Adhesion of Cells, pages 755–802. Elsevier, 1995.

[68] Jürgen Tuchtenhagen, Wolfgang Ziegler, and Alfred Blume. Acyl chain conformational ordering in liquid-crystalline bilayers: comparative ft-ir and 2h-nmr studies of phospholipids differing in headgroup structure and chain length. *European Biophysics Journal*, 23(5):323–335, 1994.

[69] Scott E Feller, Daxu Yin, Richard W Pastor, and Alexander D MacKerell Jr. Molecular dynamics simulation of unsaturated lipid bilayers at low hydration: parameterization and comparison with diffraction studies. *Biophysical journal*, 73(5):2269, 1997.

[70] Jeffery B Klauda, Mary F Roberts, Alfred G Redfield, Bernard R Brooks, and Richard W Pastor. Rotation of lipids in membranes: molecular dynamics simulation, 31 p spin-lattice relaxation, and rigid-body dynamics. *Biophysical journal*, 94(8):3074–3083, 2008.

[71] Winchil LC Vaz, Robert M Clegg, and Dieter Hallmann. Translational diffusion of lipids in liquid crystalline phase phosphatidylcholine multibilayers. a comparison of experiment with theory. *Biochemistry*, 24(3):781–786, 1985.

[72] Agnieszka E Hac, Heiko M Seeger, Matthias Fidorra, and Thomas Heimburg. Diffusion in two-component lipid membranes—a fluorescence correlation spectroscopy and monte carlo simulation study. *Biophysical journal*, 88(1):317–333, 2005.

[73] Harden M. McConnell and Roger D. Kornberg. Inside-outside transitions of phospholipids in vesicle membranes. *Biochemistry*, 10(7):1111–1120, 1971.

[74] Edouard M Bevers, Paul Comfurius, David WC Dekkers, and Robert FA Zwaal. Lipid translocation across the plasma membrane of mammalian cells. *Biochimica et Biophysica Acta (BBA)-Molecular and Cell Biology of Lipids*, 1439(3):317–330, 1999.

[75] T Pomorski and AK Menon. Lipid flippases and their biological functions. *Cellular and Molecular Life Sciences CMLS*, 63(24):2908–2921, 2006.

[76] Andrey A Gurtovenko, Olajide I Onike, and Jamshed Anwar. Chemically induced phospholipid translocation across biological membranes. *Langmuir*, 24(17):9656–9660, 2008.

[77] D Peter Tieleman and Siewert-Jan Marrink. Lipids out of equilibrium: Energetics of desorption and pore mediated flip-flop. *Journal of the American Chemical Society*, 128(38):12462–12467, 2006.

[78] Pietro Cicuta, Sarah L Keller, and Sarah L Veatch. Diffusion of liquid domains in lipid bilayer membranes. *The Journal of Physical Chemistry B*, 111(13):3328–3331, 2007.

[79] Nicholas Metropolis, Arianna W Rosenbluth, Marshall N Rosenbluth, Augusta H Teller, and Edward Teller. Equation of state calculations by fast computing machines. *The journal of chemical physics*, 21(6):1087–1092, 1953.

[80] Thomas Heimburg. *Thermal Biophysics of Membranes.* Wiley-VCH, 2007.

[81] Martin Karplus et al. Charmm: A program for macromolecular energy, minimization, and dynamics calculations. *J Comput Chem*, 4:187217, 1983.

[82] Walter RP Scott, Philippe H Hünenberger, Ilario G Tironi, Alan E Mark, Salomon R Billeter, Jens Fennen, Andrew E Torda, Thomas Huber, Peter Krüger, and Wilfred F van Gunsteren. The gromos biomolecular simulation program package. *The Journal of Physical Chemistry A*, 103(19):3596–3607, 1999.

[83] Daan Frenkel and Berend Smit. *Understanding Molecular Simulations: From Algorithms to Applications.* Academic Press, 2002.

[84] Giovanni Bussi, Davide Donadio, and Michele Parrinello. Canonical sampling through velocity rescaling. *The Journal of Chemical Physics*, 126(1):–, 2007.

[85] David E Shaw, Ron O Dror, John K Salmon, JP Grossman, Kenneth M Mackenzie, Joseph Bank, Cliff Young, Martin M Deneroff, Brannon Batson, Kevin J Bowers, et al. Millisecond-scale molecular dynamics simulations on anton. In *High Performance Computing Networking, Storage and Analysis, Proceedings of the Conference on*, pages 1–11. IEEE, 2009.

[86] Siewert J. Marrink, H. Jelger Risselada, Serge Yefimov, D. Peter Tieleman, and Alex H. de Vries. The martini force field: coarse grained model for biomolecular simulations. *The Journal of Physical Chemistry B*, 111(27):7812–7824, 2007. PMID: 17569554.

[87] Dominik Fritz, Konstantin Koschke, Vagelis A Harmandaris, Nico FA van der Vegt, and Kurt Kremer. Multiscale modeling of soft matter: scaling of dynamics. *Physical Chemistry Chemical Physics*, 13(22):10412–10420, 2011.

[88] Djurre Hendrik de Jong. *A molecular view on the organizational complexity of proteins in membranes.* PhD thesis, University of Groningen, 2013.

[89] J. B. Birks. Excimers. *Reports on Progress in Physics*, 38(8):903, 1975.

[90] JB Birks and LG Christophorou. Excimer fluorescence spectra of pyrene derivatives. *Spectrochimica Acta*, 19(2):401–410, 1963.

[91] Frank C Collins and George E Kimball. Diffusion-controlled reaction rates. *Journal of colloid science*, 4(4):425–437, 1949.

[92] K. Razi Naqvi. Diffusion-controlled reactions in two-dimensional fluids: discussion of measurements of lateral diffusion of lipids in biological membranes. *Chemical Physics Letters*, 28(2):280 – 284, 1974.

[93] D. C. Torney and H. M. McConnell. Diffusion-limited reaction rate theory for two-dimensional systems. 387(1792):147–170, 1983.

[94] Hans-Joachim Galla and Erich Sackmann. Lateral diffusion in the hydrophobic region of membranes: use of pyrene excimers as optical probes. *Biochimica et Biophysica Acta (BBA) - Biomembranes*, 339(1):103 – 115, 1974.

[95] Pentti Somerharju. Pyrene-labeled lipids as tools in membrane biophysics and cell biology. *Chemistry and Physics of Lipids*, 116(1–2):57 – 74, 2002.

[96] Eurico Melo and Jorge Martins. Kinetics of bimolecular reactions in model bilayers and biological membranes. a critical review. *Biophysical Chemistry*, 123(2–3):77 – 94, 2006.

[97] E.J. Montroll and B.J. West. *Fluctuation Phenomena*, chapter On an enriched Collection of Stochastic Processes, page 61. North-Holland, 1979.

[98] Jorge Martins, Winchil L. C. Vaz, and Eurico Melo. Long-range diffusion coefficients in two-dimensional fluid media measured by the pyrene excimer reaction†. *The Journal of Physical Chemistry*, 100(5):1889–1895, 1996.

[99] Jirasak Wong-Ekkabut, Zhitao Xu, Wannapong Triampo, I Ming Tang, D. Peter Tieleman, and Luca Monticelli. Effect of lipid peroxidation on the properties of lipid bilayers: A molecular dynamics study. *Biophysical Journal*, 93(12):4225–4236, 2007.

[100] Omar Mertins, Isabel O.L. Bacellar, Fabrice Thalmann, Carlos M. Marques, Maurício S. Baptista, and Rosangela Itri. Physical damage on giant vesicles membrane as a result of methylene blue photoirradiation. *Biophysical Journal*, 106(1):162 – 171, 2014.

[101] John F. Nagle and Stephanie Tristram-Nagle. Structure of lipid bilayers. *Biochimica and Biophysica Acta*, 1469:159–195, 2000.

[102] P. H. B. Aoki, A. P. Schroder, C. J. L. Constantino, and C. M. Marques. Bioadhesive giant vesicles for monitoring hydroperoxidation in lipid membranes. *Soft Matter*, 11:5995–5998, 2015.

[103] J.A. Barker and D. Henderson. What is a ”liquid” ? understanding the states of matter. *Review of Modern Physics*, 48(4):587, 1976.

[104] J.P Hansen and I Mac Donald. *Theory of simple liquids*. Oxford Science Publications, 1986.

[105] T.V Ramakrishnan and M Yussouf. First principles order parameter theory of freezing. *Physical Review B*, 19(5), 1979.

[106] P Allen and P Tildesley. *Numerical simulation*. Oxford, 1986.

Abstract We propose a novel approach to extract the lateral diffusion coefficient in lipid bilayers using excimer formation. In contrast to previous statistical models that modeled the system as points undergoing jumps from site to site on a lattice, we use coarse-grained molecular dynamics to study lipid bilayers simulated using the Martini force field. We derive time dependent reaction rates from survival probabilities obtained *a posteriori* from numerically generated trajectories of symmetric DOPC (*1,2-Dioleoyl-sn-glycero-3-phosphocholine*) and POPC (*1-palmitoyl-2-oleoyl-sn-glycero-3-phosphocholine*) bilayers at 283K and 293K respectively. Collision dynamics are determined by *virtually* relabeling the simulated molecules. The fluorescent probes are assumed to behave like ordinary membrane lipids and therefore the dynamics remain unaffected. We derive a generalized expression for the survival probability combining independent pairs and size scaling assumptions, but no assumption is made regarding the kinetic rate of the excimer formation process. By fitting the numerically determined normalized fluorescence emission intensities to experimental titration curves, we obtain two sets of results for the lateral diffusion coefficients depending whether interleaflet excimer association is allowed or not. We use a capture radius of 0.5 nm, the distance at which the probes react to form excimers. By relating Martini dynamics to real fluorescence experiments, we estimate the numerical Martini acceleration factor.

We also study mixtures of oxidized-non oxidized DOPC and POPC bilayers using a hydroperoxidized model of these lipids for different concentrations of the oxidized component (3.1%, 25% and 50%). Using pair correlation functions, we extract structural information on the systems and determine whether the two components are prone to mixing or not. Finally, we calculate the thermodynamic mixing parameters within the framework of the virial expansion.

Resume Nous proposons une nouvelle approche pour déterminer le coefficient de diffusion dans des membranes lipidiques se basant sur la formation d'excimères. Alors que les autres modèles statistiques considèrent le système comme un ensemble de points sur un réseau, nous utilisons un modèle à gros grain afin d'étudier des bicouches lipidiques simulées à l'aide du champs de force Martini. Nous déterminons le taux de réaction dépendant du temps à partir des probabilités de survie obtenues *a posteriori* à l'aide des trajectoires numeriques des bicouches symétriques de DOPC (*1,2-Dioleoyl-sn-glycero-3-phosphocholine*) et POPC (*1-palmitoyl-2-oleoyl-sn-glycero-3-phosphocholine*) simulées à 283 K et 293 K respectivement. Les dynamiques de collision sont obtenues en distinguant *virtuellement* les molécules simulées. Les sondes fluorescentes sont supposées semblables aux lipides, et par conséquent, ne modifient pas la dynamique. Nous obtenons une expression générale pour la probabilité de survie en combinant approximation des paires indépendantes et propriétés d'échelle, mais aucune hypothèse n'est faite pour le taux de formation d'excimère. En superposant les intensités d'émission de fluorescence normalisées, déterminées numériquement, aux courbes de titrations expérimentales, nous obtenons deux ensembles de résultats pour le coefficient de diffusion latéral, selon que l'association entre feuillets est autorisée ou pas. Nous utilisons un rayon de capture de 0.5 nm, la distance à partir de laquelle les deux sondes réagissent pour former un excimère. En comparant la dynamique Martini aux expériences de fluorescence, il est possible d'estimer le facteur d'accélération.

Nous avons également étudié les mélanges binaires de lipides oxydés-non oxydés dans le cas de bicouches de DOPC et POPC à differentes concentrations (3.1%, 25% and 50%) de lipides peroxidés. A l' aide de la fonction de correlation de paire, nous déteminons si les lipides ont tendance à se mélanger ou non. Enfin, nous calculons les paramètres de mélanges dans le cadre du developpement du viriel.